Structure - based design of inhibitors of the zinc-dependent enzymes histone deacetylase (HDAC) and UDP-3-O-(R-3-hydroxymyristoylyl)-N-acetylglucosamine deacetylase (LpxC)

DISSERTATION

zur Erlangen des akademischen Grades

Doctor rerum naturalium (Dr. rer. nat.)

der Naturwissenschaftlichen Fakultät I Biowissenschafften

der Martin-Luther-Universität Halle-Wittenberg

von

M. Sc. Emre Fatih Bülbül

geboren am 07.08.1991

geboren in Kütahya

ABSTRACT

Computer-aided drug design (CADD) techniques are used nowadays to design novel compounds in a faster and cheaper way than in previous periods. In the current work, CADD methods were used to identify and develop novel compounds that are both potent and selective against two groups of zinc-dependent enzymes: histone deacetylase (HDAC) and UDP-3-*O*-(*R*-3-hydroxymyristoylyl)-*N*-acetylglucosamine deacetylase (LpxC). HDACs are engaged in multiple physiological processes. Thus, HDACs represent potential drug targets for various diseases, from cancer to parasitic diseases. In the first part of this work, the parasitic *Trypanosoma cruzi* deacetylase 2 (tcDAC2) is targeted for the treatment of Chagas disease. Novel hydroxamic acid derivatives were suggested using CADD techniques and tested against the parasitic tcDAC2 protein. In a second project, the zinc-binding group of the hydroxamic acid derivatives was replaced by 2-aminobenzamides to obtain selective human class I HDAC inhibitors. Their linker and cap groups were optimized by using different design approaches. The compounds were tested against human class I HDACs. To develop quantitative structure-activity relationships (QSAR) the docked compounds were rescored by using binding free energy (BFE) calculations. Then, novel 2-aminobenzamides were designed using the *in silico* predictions. In a third project, alkylhydrazides targeting the foot pocket of human class I HDACs were designed to achieve selectivity among human class I HDACs. The structure-activity relationship (SAR) of the protein-ligand complexes was determined by molecular docking and molecular dynamics simulations (MD). In a fourth project, the zinc dependent LpxC, which is a promising antibacterial target, is addressed by hydroxamic acid derivatives. Molecular docking, binding free energy calculations, and MD simulations were used to rationalize the binding mode of the compounds and to support the chemical optimization. The results obtained in the current work illustrates how structure-based drug design (SBDD) methods can be used to design potent and selective zinc-dependent enzyme inhibitors and to accelerate drug discovery projects.

i

KURZFASSUNG

CADD-Techniken (Computer-gestütztes Wirkstoffdesign) werden heutzutage verwendet, um neuartige Inhibitoren schneller und kostengünstiger zu entwickeln als in früheren Phasen. Die CADD-Methoden wurden angewendet, um wirksame und selektive neue Inhibitoren gegen zwei Familien zinkabhängiger Enzyme vorzuschlagen. Histon-Deacetylasen (HDAC) sind an mehreren physiologischen Prozessen beteiligt. Daher sind sie ein potenzielles Ziel für verschiedene Krankheiten, von Krebs bis hin zu parasitären Erkrankungen. Erstens steht die parasitäre Trypanosoma-cruzi-Deacetylase 2 (tcDAC2) im Fokus zur Behandlung der Chagas-Krankheit. Die neuartigen Hydroxamsäurederivate wurden unter Verwendung von CADD-Techniken vorgeschlagen und gegen das parasitäre tcDAC2 getestet. Zweitens wurde die zinkbindende Gruppe der Hydroxamsäurederivate durch ein 2-Aminobenzamid ersetzt. Ihre Linker- und Cap-Gruppen wurden unter Verwendung verschiedener Design Ansätze optimiert. Die Inhibitoren wurden gegen humane HDACs der Klasse I getestet. Um quantitative Struktur-Wirkungs Beziehungen zu erstellen wurden die gedockten Inhibitoren unter Verwendung von Berechnungen der freien Bindungsenergie neu bewertet. Dann wurden neue 2-Aminobenzamide unter Verwendung der *in silico*-Vorhersagen entworfen. Drittens wurden Alkylhydrazide entworfen, die auf die Fußtasche von humanen Klasse-I-HDACs abzielen, um die Selektivität für humane Klasse-I-HDACs zu erreichen. Die Struktur-Aktivitäts-Beziehung (SAR) der Protein-Ligand-Komplexe wurde durch molekulares Docking und moleculardynamische Simulationen (MD) bestimmt. Neben HDACs wird UDP-3-O-(R-3-Hydroxymyristoylyl)-N-Acetylglucosamin-Deacetylase (LpxC) von Hydroxamsäure-Derivaten angegriffen. Das molekulare Docking, Berechnungen der freien Bindungsenergie (BFE) und Molekulardynamiksimulationen (MD) wurden verwendet, um die Projekte zu voranzutreiben. Diese Ergebnisse der vorliegenden Arbeit veranschaulichen, wie Methoden des strukturbasierten Wirkstoffdesigns (SBDD) verwendet werden können, um wirksame und selektive zinkabhängige Enzyminhibitoren zu entwickeln und die Projekte zu beschleunigen.

Schlagwörter: computer gestütztes wirkstoff design, zinc-abhängig enzyme, HDAC, LpxC, tcDAC2, molekular docking, molekular dynamische simulation, binding free energy calculations.

PUBLICATIONS ARISING FROM THE WORK IN THE THESIS

The results of the thesis have been published in the following manuscripts:

1) Synthesis, Biological evaluation, and molecular docking studies of aldotetronic acid-based-LpxC inhibitors. Wimmer, S, Hoff K, Martin B, Grewer M, Denni L, Massanet RL, Raimondi MV, **Bülbül EF,** Melesina J, Hotop S, Haupenthal J, Rohde H, Heisig P, Hirsch A, Brönstup M, Sippl W, Holl R., Bioorganic Chemistry, 2022, 106331. doi: 10.1016/j.bioorg.2022.106331

2) Development of alkylated hydrazides as highly potent and selective class I HDAC inhibitors with T cell modulatory properties, Sun P, Wang J, Khan KS, Yang W, Ng WL, Ilmenov N, Zessin M, **Bülbül EF**, Robaa D, Erdmann F, Schmidt M, Romier C, Schutkowski M, Cheng A, Sippl W., J. Med. Chem, 2022, 16313-16337, doi: 10.1021/acs.jmedchem.2c01132

3) Small Changes Make the Difference for SIRT2: Two Different Binding Modes for 3-Arylmercapto-Acylated Lysine Derivatives. Kalbas D, Meleshin M, Liebscher S, Zessin M, Melesina J, Schiene-Fischer C, **Bülbül EF**, Bordusa F, Sippl W, Schutkowski M., Biochemistry. 2022 Aug 16. doi: 10.1021/acs.biochem.2c00211. Online ahead of print.

4) Docking, Binding Free Energy Calculations and In Vitro Characterization of Pyrazine Linked 2-Aminobenzamides as Novel Class I Histone Deacetylase (HDAC) Inhibitors. **Bülbül EF**, Melesina J, Ibrahim HS, Abdelsalam M, Vecchio A, Robaa D, Zessin M, Schutkowski M, Sippl W., Molecules. 2022 Apr 14;27(8):2526. doi: 10.3390/molecules27082526.

5) Synthesis, Molecular Docking and Biological Characterization of Pyrazine Linked 2-Aminobenzamides as New Class I Selective Histone Deacetylase (HDAC) Inhibitors with Anti-Leukemic Activity. Ibrahim HS, Abdelsalam M, Zeyn Y, Zessin M, Mustafa AM, Fischer MA, Zeyen P, Sun P, **Bülbül EF**, Vecchio A, Erdmann F, Schmidt M, Robaa D, Barinka C, Romier C, Schutkowski M, Krämer OH, Sippl W., Int J Mol Sci. 2021 Dec 29;23(1):369. doi: 10.3390/ijms23010369.

6) Synthesis, biological evaluation, and molecular docking studies of deoxygenated C-glycosides as LpxC inhibitors. Dreger A, Hoff K, Agoglitta O, **Bülbül EF**, Melesina J, Sippl W, Holl R., Bioorg Chem. 2021 Dec; 117:105403. doi: 10.1016/j.bioorg.2021.105403.

7) Strategies to Design Selective Histone Deacetylase Inhibitors. Melesina J, Simoben CV, Praetorius L, **Bülbül EF**, Robaa D, Sippl W., ChemMedChem. 2021 May 6;16(9):1336-1359. doi: 10.1002/cmdc.202000934.

8) Synthesis and biological evaluation of triazolyl-substituted benzyloxyacetohydroxamic acids as LpxC inhibitors. Hoff K, Mielniczuk S, Agoglitta O, Iorio MT, Caldara M, **Bülbül EF**,

Melesina J, Sippl W, Holl R., Bioorg Med Chem. 2020 Jul 1;28(13):115529. doi: 10.1016/j.bmc.2020.115529.

9) Chiral Pool Synthesis, Biological Evaluation and Molecular Docking Studies of C-Furanosidic LpxC Inhibitors. Dreger A, Kharwb O, Agoglitta O, **Bülbül EF**, Melesina J, Sippl W, Holl R., ChemMedChem. 2019 Apr 17;14(8):871-886. doi: 10.1002/cmdc.201900068.

ACKNOWLEDGEMENT

DEDICATION

I dedicate this dissertation to my parents, Mükerrem and Esra Bülbül, to my sister, Betül Bilge Bülbül, to my son Kerem Bülbül and my lovely wife, Sümeyya Parlakyildiz Bülbül.

CONTENTS

LIST OF FIGURES

xiii

LIST OF TABLES

LIST OF ABBREVIATIONS

μM	Micro molar
2D	Two dimensional
3D	Three dimensional
AM1-BCC	Austin Model1 with bond charge correction
BFE	Binding free energy
CADD	Computer-aided drug design
CD	catalytic domains
CoREST	Corepressor of REST
DMSO	Dimethylsülfoxide
FEP	Free energy perturbation
GAFF	General amber force field
HAT	Histone deacetyltransferase
HDAC	Histone deactylase
IC$_{50}$	Half-maximal inhibitory concentration
LpxC	UDP-3-O-(R-3-hydrocymyristoyl)-N-acetyl-glucosamide deacetylase
MD	Molecular dynamics
MIDAC	Mitotic deacetylase complex
MMGBSA	Molecular mechanics - generalized born-surface area
MMPBSA	Molecular mechanics - poisson boltzman-surface area
NAD	Nicotinamide adenine denucleotide
NCoR	Nuclear receptor corepressor
nM	Nano molar
NuRD	Nucleosome remodeling and deacetylase complex
PDB	Protein data bank
PTM	Post-translational modification
QSAR	Quantitative structure-activity relationship

RMSD	Root – mean – square – deviation
RMSE	Root – mean – square – error
SAR	Structure activity relationship
SBDD	Structure based drug design
SMRT	Silencing mediator for retinoid and thyroid receptors
SP	Standard precision
tcDAC2	*Trypanosoma cruzi* histone deacetylase 2
TI	Thermodynamic integration
TSA	Trichostatin A
WHO	World health organization
ZBG	Zinc binding group
ZMAL	Z(Ac)Lys - AMC
ZMTFAL	Z(Tfa)Lys – AMC
Zn	Zinc atom

1. INTRODUCTION

1.1. HDACs

The epigenetic term, which was first used during the 1940s [1], means modifications to gene expression without changing DNA sequence [2]. Chromatin structure regulates gene expression by modifying gene structure and function [3]. Nucleosomes are the central structural units of the chromatin and are comprised of a coil of DNA and histone proteins (H2A, H2B, H3 and H4, Figure 1) [4, 5]. A main focus of epigenetic drug discovery is to target the histone modifying proteins and hence remodel the chromatin structure [6].

Histone proteins include many basic lysine residues in their histone tails. These lysine residues interact with the negatively charged DNA. The chromatin structure is mainly being remodelled by breaking the interaction between the DNA and histone proteins [7]. These basic lysine residues on the histone tails are often modified by the post-translational modifications (PTM), including ubiquitination, SUMOylation, glycosylation, hydroxylation, phosphorylation, sulfation, methylation, and acetylation [8]. The epigenetic machinery mainly focuses on targeting these histone tails by adding, recognizing or removing the groups from them with the aid of the epigenetic machinery (writers-readers-erasers); consequently, the gene structure and function can be altered. Writer enzymes such as methylases, acetylases, and phosphorylases add moieties to the histone tails. Readers recognize the histone modifications, while eraser enzymes such as demethylases, deacetylases remove the moieties from the histone tails (Figure 1) [9].
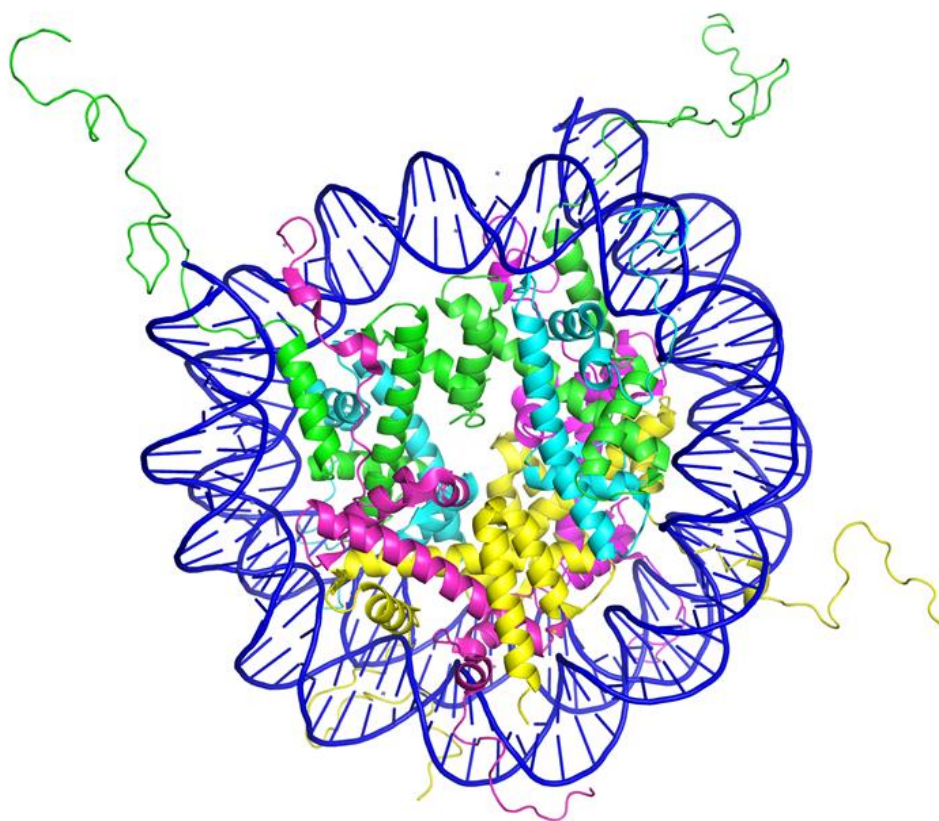
Figure 1. Structure of nucleosome (PDB ID: 1KX5 [10]). Four histone proteins are located in the core of the nucleosome. H2A (magenta), H2B (yellow). H3 (green) and H4 (cyan) are wrapped by DNA (blue). Histone tails protrude from nucleosome.

Acetylation of the histone proteins is a specific PTM that affects the chromatin structure, thereby changing gene expression. The acetylation mechanism was first reported by Allfrey et al. in 1964 [11]. This histone acetylation is controlled by two enzymes: histone acetyltransferases (HAT) and histone deacetylases (HDAC). HATs catalyze the addition of the acetyl group to the amino group of the lysine side chain, resulting in the removal of the positive charge on the lysine side chains. That process decreases the interaction between the DNA and histones, making the chromatin more accessible to transcription factors. In contrast, HDAC enzymes remove the acetyl group from the lysine residues and increase the affinity between histones and DNA. Thus, the binding of transcription factors is blocked, and gene expression is repressed [12-14]. The interplay between HAT and HDAC is a reversible process (Figure 2) [3, 14].
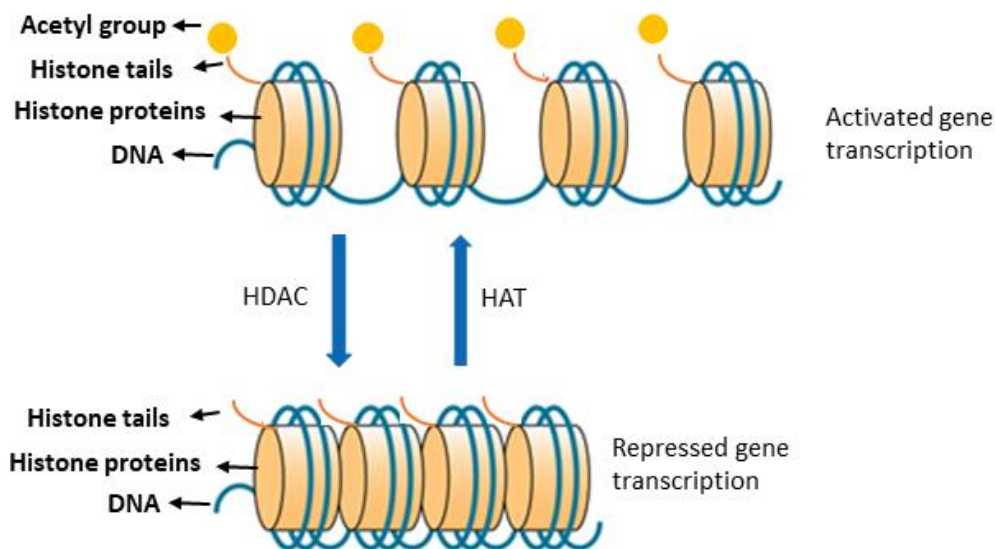
Figure 2. Acetylation-deacetylation on histone proteins (adapted from [3].)

Histone deacetylases (HDAC) are present in a wide range of species, including human and yeast [15]. Therefore, they are attractive therapeutic targets for treatment of variety of illnesses, including cancer, inflammation, cardiac and neurodegenerative diseases, immune disorders, and viral and parasitic diseases [16-22].

At present, 18 human HDACs have been identified and divided into two groups and categorized into four sub-classes based on how closely they resemble yeast (Table 1). Class I, class II, and class IV HDACs are zinc (Zn^{+2}) dependent HDACs. Zinc ion is a co-factor required by these enzymes. Class III enzymes (also known as sirtuins) that need NAD^+ as a coenzyme are nicotinamide adenine dinucleotide (NAD^+) dependent enzymes. Class III enzymes possess different structures and mechanisms of action [23]. In this study, we only focused on zinc-dependent histone deacetylases.

Class I HDACs (HDAC1/2/3/8) are found in the nucleus and share similarity with the Rpd3 yeast protein. Each one contains approximately 400 amino acids [14]. The recruitment and activation of class I HDACs, particularly HDAC1-3, is mediated by corepressor proteins. These corepressor proteins alter gene expression by repressing transcriptional factors [24, 25].

HDAC1 and HDAC2 interact with the nucleosome remodeling and deacetylase complex (NuRD) [26], transcriptional regulatory protein (sin3A) [27], corepressor of REST (CoREST) [28] and the mitotic deacetylase complex (MIDAC) [29], while HDAC3 only forms a complex with the silencing mediator for retinoid and thyroid receptors (SMRT) [30] and nuclear receptor corepressor (NCoR) [31]. HDAC8 does not require the formation of a complex with a corepressor to be active [25, 32, 33]. Class II HDACs are found between the cytoplasm and nucleus and are similar to the Hda1 yeast protein. They contain 600-1200 amino acids. Class IIa enzymes (HDAC4/5/7/9) share an N-terminal domain with a regulatory function [34]. They become members of the SMRT/NCoR repression complex. Compared to class I HDACs, they do not show strong deacetylase activity when bound to the corepressor [35]. Class IIb enzymes (HDAC6/10) have an extra tail domain at the C-terminus. HDAC6 is characterized by two catalytic domains (CD1 and CD2) [14] and is thought to show efficient lysine deacetylase activity [36]. HDAC10 is a potent polyamine deacetylase that only has one deacetylase domain [37]. Class IV HDAC (HDAC11) differs significantly from other HDACs. It is located in the nucleus. Class IV HDAC contains around 300 amino acids [38, 39]. Among the zinc dependent HDACs, class I HDACs (HDAC1-3 and 8) and class IIb HDAC6 are more efficient deacetylases, which can be targeted for drug design [23].

Table 1. Classification of Zinc dependent HDACs

Class	Subtypes
Class I	HDAC1, HDAC2, HDAC3 and HDAC8
Class IIa	HDAC4, HDAC5, HDAC7 and HDAC9
Class IIb	HDAC6 and HDAC10
Class IV	HDAC11

All HDAC family members have undergone knockout investigations in mice [40]. It has been discovered that class I HDACs are widely expressed in all tissues. In mice, deleting HDAC1 and HDAC3 genes causes embryonic lethality [41, 42]. Surprisingly, the deletion of HDAC2 genes did not result in embryonic lethality, but the mice died due to cardiac defects [43]. The deletion of HDAC8 resulted in a cranial defect in mice [44]. On the other hand, class IIa HDACs were expressed in a specific tissue, in contrast to class I HDACs. The knockout studies of HDAC4 resulted in abnormal hyperosteogeny. HDAC5 and HDAC9 knockout studies caused cardiac defects, while HDAC7 knockouts exhibited embryonic lethality [45-47].

In contrast to class IIa, class IIb was found to be non-essential for mouse development. HDAC6-deficient mice and HDAC10-deficient mice did not show any visible phenotypes, and they developed normally, although the enzyme is ubiquitously expressed [48].

It is supposed that class I and class II share a similar catalytic mechanism due to the presence of a conserved catalytic core in class I and class II HDACs. Till now, various catalytic mechanisms have been suggested by Finning et al. [49], Vanommeslaeghe et al. [50], and Corminboeuf et al. [51]. Finnin et al. proposed the first catalytic mechanism for histone deacetylase like protein (HDLP) from *Aquifex aeolicus*, in which H131 (H142 in HDAC8) becomes the general base catalyst and H132 (H143 in HDAC8) serves as a general acid catalyst [49]. The zinc ion in the crystal structure is located at the bottom of the catalytic pocket and coordinated by D168 (D178 in HDAC8), H170 (H180 in HDAC8), and D258 (D267 in HDAC8) and a water molecule in HDLP. Additionally, H131 (H142 in HDAC8), H132 (H143 in HDAC8) and Y297 (Y306 in HDAC8) are found at the bottom of the catalytic pocket. H131 (H142 in HDAC8) and H132 (H143 in HDAC8) exhibit hydrogen-bond interactions with D166 (D176 in HDAC8) and D173 (D183 in HDAC8), respectively. The H131 - D166 (H142 – D176 in HDAC8) is found deeper inside the pocket than H132 – D178 (H143 – D178 in HDAC8) which is partially solvent exposed. This His-Asp arrangement in the charge-relay system increases the basicity of the imidazole on histidine residues and adjusts the histidine conformation. Y297 (Y306 in HDAC8) is positioned next to the zinc ion, and opposite part of the charge-relay system, and does not show interactions with the zinc ion. The carbonyl oxygen of the substrate could make interaction with the zinc ion. The carbonyl carbon is positioned close to the solvent molecule. The zinc ion makes the carbonyl carbon a better electrophile and adjusts the water orientation. The H131-D176 charge-relay system could increase the nucleophilicity of the water molecule. The tetrahedral intermediate is formed as a result of the nucleophilic attack of the water molecule on the carbonyl carbon of the substrate. The formed tetrahedral intermediate could be stabilized by bidentate chelation to the zinc ion through both oxygen atoms. Additionally, Y297 contributes to the stabilization of the tetrahedral intermediate by a hydrogen bond. In the last step, the intermediate breaks its amide bond and yields 2 products; acetate and lysine.

More recently, this proposal was revised for the HDAC8 enzyme by Gantt in 2016 [52]. According to the revised proposal (Figure 3), H143 serves as a single general base-general acid catalyst and facilitates a nucleophilic attack on the carbonyl group of the substrate by activating a water molecule. In the first step (Figure 3A), H143 accepts a proton from the water molecule and serves as a general basic catalyst. The water molecule binds to the carbonyl group of the substrate. Then (Figure 3B), H143 donates its protons to the amide-NH of the substrate. Here, H143 serves as a general acid catalyst. The acetate group is detached from the substrate (Figure 3C). H142 becomes an electrostatic catalyst for the negative charge of the acetate intermediate and simultaneously arranges the position of H143 through steric interactions. In addition, Y306 stabilizes the tetrahedral intermediate by showing hydrogen bond interactions (Figure 3) [52].
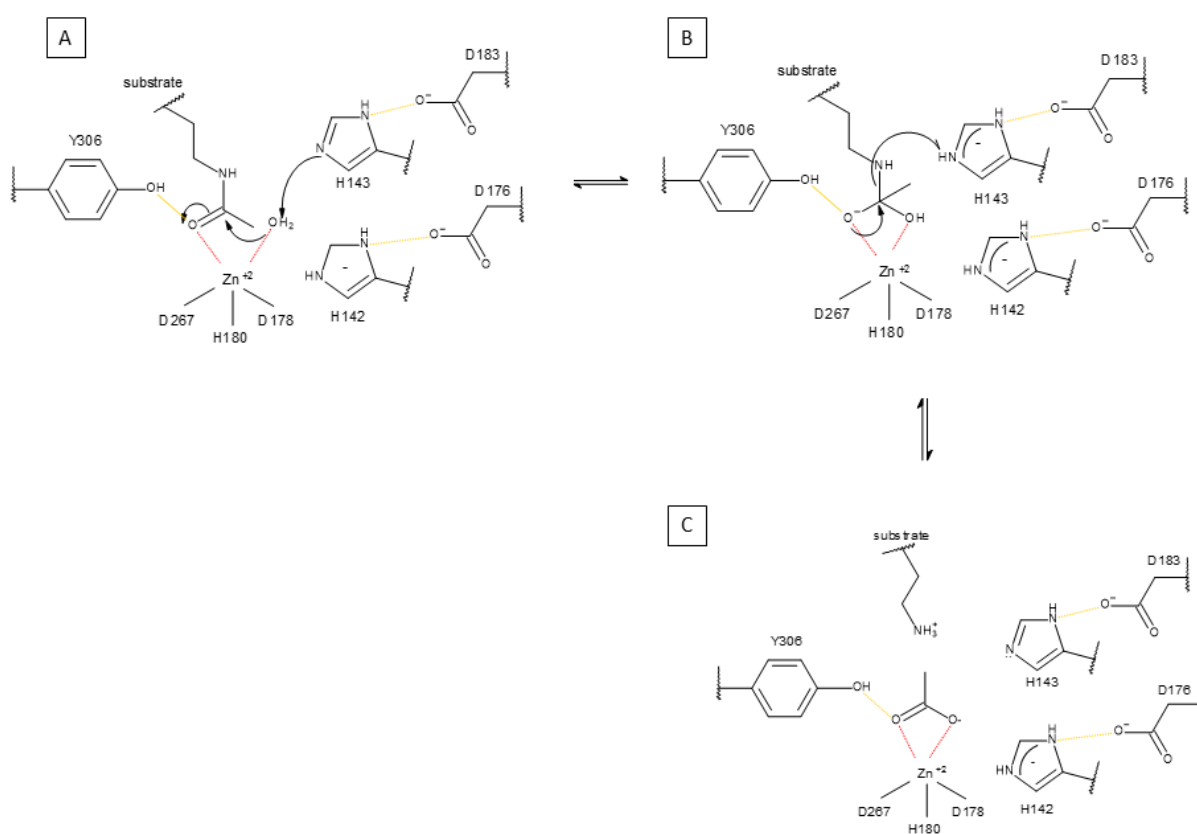
Figure 3. The proposed catalytic mechanism of HDACs by Gantt et. al. (adapted from [52])

Although HDACs show some differences, they have structurally conserved catalytic domains, as seen in almost three hundred solved crystal structures of HDACs and HDAC like proteins from various organisms deposited in protein data bank (PDB, rcsb.org) [23, 53, 54].

The catalytic domain consists of a central eight stranded parallel β-sheet surrounded by α-helices, as exemplified by the single domain of HDAC2 (PDB ID: 4LXZ [55]) in Figure 4. The β-sheets and α-helices are connected by loops [23], which differ in length and conformation. The zinc ion is located at the bottom of the catalytic pocket. The catalytic pocket consists of an acetate binding cavity, an 11 Å substrate binding tunnel, and the rim of the pocket. Different HDACs extend their catalytic pockets by sub-pockets, such as the 14 Å internal cavity in class I HDACs (called foot pocket), side pocket in HDAC8 and lower pocket in class IIa HDACs [23, 56].
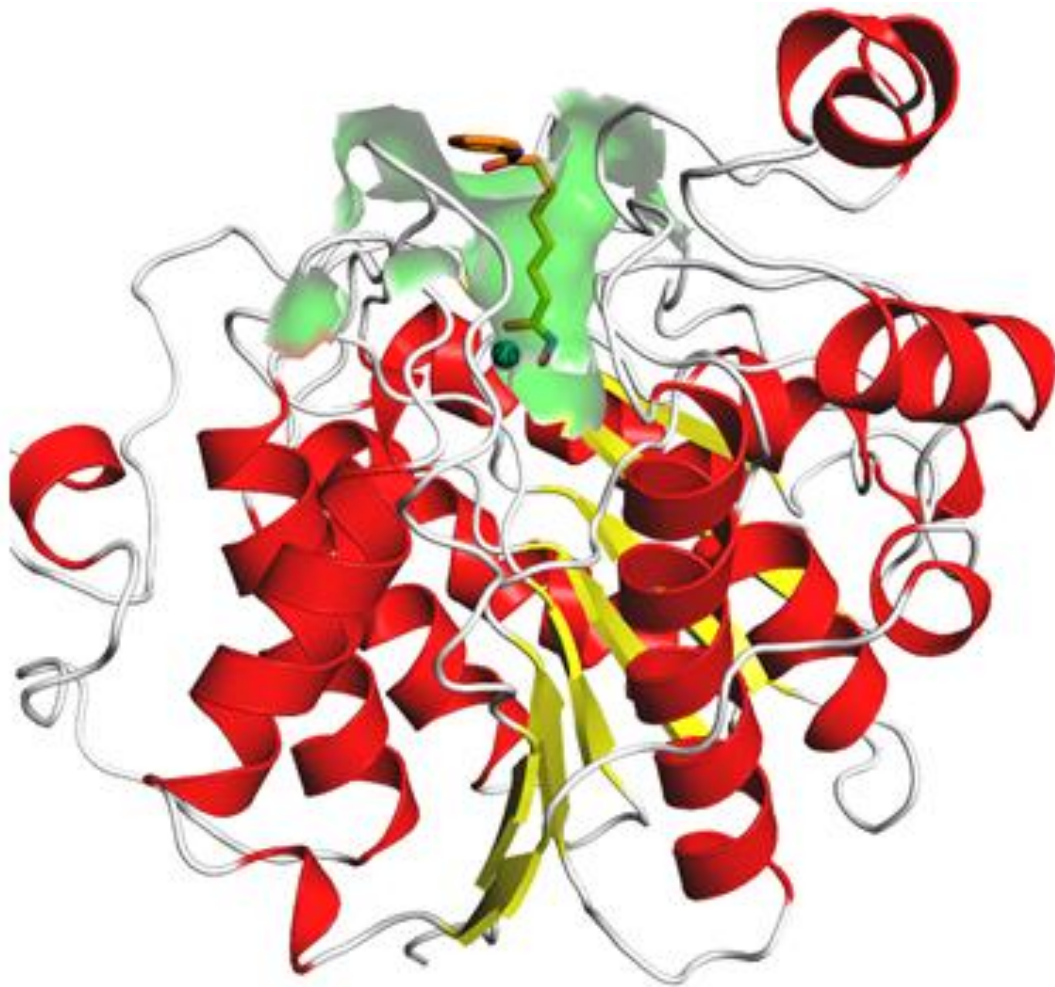
Figure 4. Crystal structure of human HDAC2 in a complex with vorinostat (PDB ID: 4LXZ). The β-sheets are represented by yellow colour, α-helices as red colour, and loops as white colour. Zinc ion is coloured as teal, and the ligand as orange carbon sticks. The active pocket surface was coloured as green.

1.1.1. Parasitic *Trypanosoma cruzi* deacetylase 2 (tcDAC2)

Over a century ago, it was found that *Trypanosoma cruzi* parasites cause American trypanosomiasis, which is known as Chagas disease [57]. The world health organization (WHO identified it as one of the neglected tropical diseases in 2005 [58], and it is a significant health problem in Latin America [59]. Chagas disease threatens lives of 6-8 million people worldwide and kills approximately 50000 people per year [60]. Only benznidazole and nifurtimox are used to fight against Chagas disease. However, due to the side effects of these used compounds, the treatment of Chagas disease is limited [61]. Therefore, finding novel agents with improved safety and efficacy is an urgent issue.

Targeting the parasitic HDACs can be an efficient strategy for the treatment of parasitic infections such as Chagas disease [62]. Four HDACs were characterized in *T. cruzi* which were classified into two classes depending on their homology to human HDACs [63] (Table 2).

Table 2. Classification of Trypanosoma cruzi HDACs

Class	Subtypes
Class I	tcDAC1, tcDAC2
Class IIb	tcDAC3, tcDAC4

Although little information is known about *T.cruzi* HDACs, gene-targeted deletion experiments by homologue recombination revealed that *T.cruzi* class I HDACs (tcDAC1, tcDAC2) are essential for the parasite. Deletion of tcDAC1 and tcDAC2 caused cell death. Specifically, tcDAC2 shows acetyl-lysine deacetylase activity [64]. Therefore, tcDAC2 became a potential target for inhibitor design.

The available crystal structures of tcDAC2 (PDB ID: 7Q1B and 7Q1C) revealed that the catalytic domain is similar to the human isoforms (HDAC1, 2, 3, and 8) [64] . The catalytic domain consists of eight stranded parallel β-sheets, which are surrounded by α-helices as shown in human isoforms (Figure 4). The active pocket region consists of an acetate binding cavity, substrate binding tunnel and surface, as seen in human isoforms (HDAC1, 2, 3, and 8). The zinc ion is located at the bottom of the catalytic site. In addition, the tcDAC2 enzyme has a

unique pocket in its active site, which can be targeted for selective inhibitor design (details will be discussed in the Results section).

1.2. LpxCs

Gram-negative bacteria are one of the major health threats. These pathogens cause morbidity and mortality all over the world. Antibiotics are drugs that are used to kill bacteria that cause infections. However, the antibiotic misuse increases bacterial resistance. The emergence of multi-drug resistant pathogens complicates treatment of the infections by current antibiotics. Thus, the discovery of novel antibacterial agents is an urgent need [65, 66].

The outer membrane of Gram-negative bacteria consists of lipopolysaccharides, which are essential for bacterial growth [67]. The lipopolysaccharides contain three components; a hydrophilic polysaccharide, *O* antigen and a hydrophobic membrane anchor, which is known as Lipid A [68]. Lipid A causes a powerful endotoxin activity in the bacteria. Moreover, it is necessary for bacterial growth. Bacteria with a reduced lipid A grow slowly, whereas the inhibition of lipid A biosynthesis causes lethality in Gram-negative bacteria [69].

The lipid A synthesis starts with the acylation of UDP-GlcNAc (Figure 5). This thermodynamically unfavourable step is catalyzed by the LpxA enzyme. The UDP-3-*O*-(R-3-hydroxymyristoyl)-*N*-acetylglucosamine deacetylase (LpxC) enzyme removes the acetyl group from the structure in the second step, which is considered the first committed step of Lipid A synthesis. This second step becomes a potential target to inhibit due to the regulatory role of LpxC in Lipid A biosynthesis [70]. Any change on LpxC activity (either increasing or decreasing) shows lethality to *Escherichia coli (E. coli).* Additionally, the zinc dependent LpxC enzyme is found in all gram-negative bacteria. Nevertheless, they do not show sequence or structural homology to their mammalian deacetylases or amidases. This uniqueness of the LpxC enzyme might be used for the design of particular inhibitors [69].

9
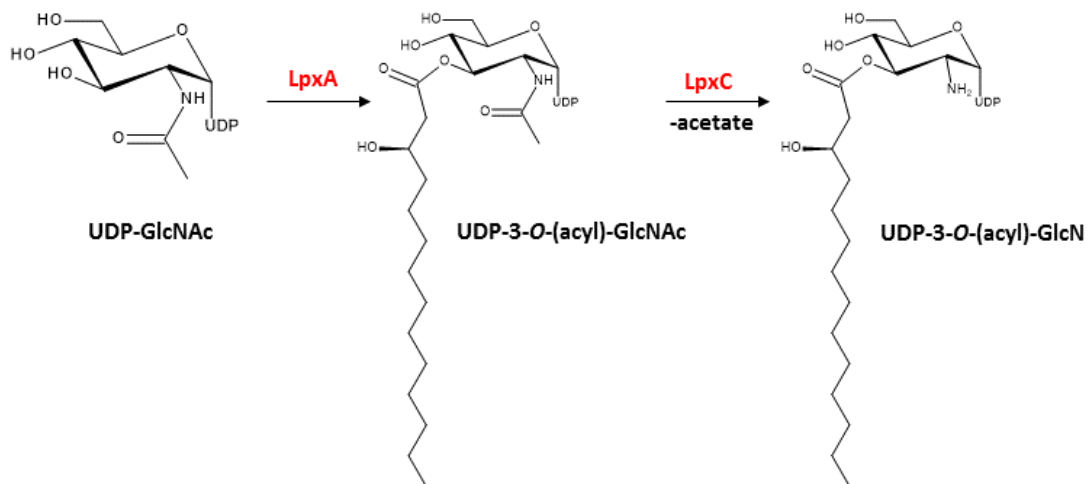
Figure 5. First two steps of Lipid A synthesis pathway (Adapted from [69])

Till now, almost one hundred X-ray structures of LpxCs from Gram-negative bacteria have been resolved with various inhibitors and deposited in the PDB (Protein Data Bank, rcsb.org) [71-74]. The X-ray structure of *Escherichia coli* LpxC (*Ec*LpxC) with inhibitor LPC-009 (PDB ID: 3P3G) serves as an example to discuss the structural information about this family of proteins and the binding mode of the inhibitors (Figure 6A) [71].

The structure of *Ec*LpxC consists of two domains. These domains form a β-α-α-β sandwich fold. Each domain contains five stranded β-sheets and two α-helices as well as unique insert regions (insert I of domain I and insert II of domain II). Insert I contains a small three stranded β-sheet that defines the boundary of the active site. Insert II forms a hydrophobic tunnel, which substrates and inhibitors can fit. Insert II has β-α-β structure. The catalytic zinc ion is found at the interface of the two domains in the active site. The catalytic zinc ion is surrounded by three important regions that can play a significant role in the inhibitor design (Figure 6B); a) hydrophobic substrate binding tunnel, b) hydrophobic patch, and c) basic patch. The hydroxamic acid of LPC-009 binds to the zinc ion in a bidentate manner. A hydrophobic substrate binding tunnel leads out of the active site. The diphenyl-diacetylene group of the LPC-009 is located in the hydrophobic substrate binding tunnel (Figure 6B). The hydrophobic patch is found in domain II and consists of many phenylalanine residues (F161, F192, and F194) (Figure 6B). The threonine group of LPC-009 is directed towards the hydrophobic patch (Figure

6B). A basic patch, which is adjacent to the hydrophobic patch, is formed by lysine residues (K143, K239, and K262) (Figure 6B). This area is also called the UDP binding pocket, where the UDP moiety of the substrate binds [69, 71].
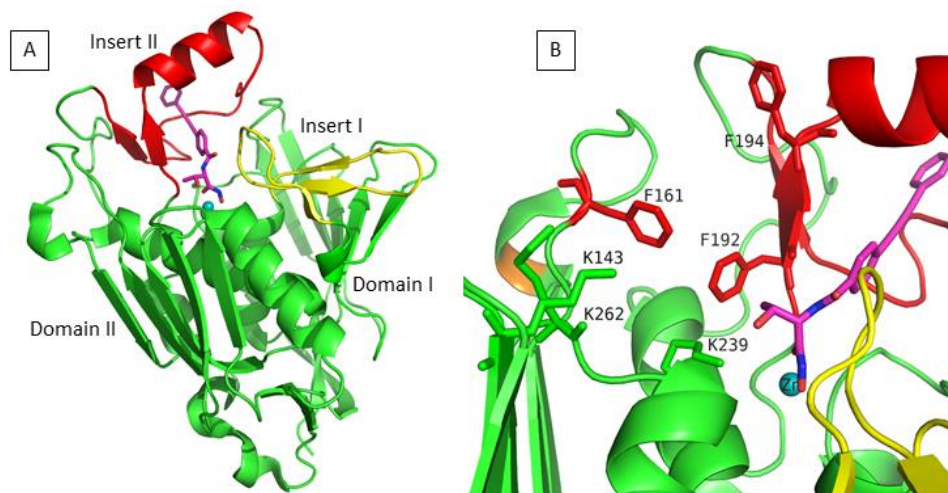
Figure 6. Crystal structure of Escherichia coli LpxC in complex with LPC-009 (PDB ID: 3PG3). A) Overall structure of the EcLpxC in shown as ribbon diagram. Domain I and domain II are coloured as green, Insert I as yellow, and Insert II as red. Zinc atom is coloured as teal, and LPC-009 inhibitor as magenta carbon sticks. B) Close view of LpxC active site. Hydrophobic patch residues are coloured as red, basic patch residues as green. Zinc atom is coloured as teal, and LPC-009 inhibitor as magenta carbon sticks.

According to the proposed LpxC mechanism (Figure 7), E78 and H265 play a role as a general acid/base catalyst pair. E78 serves as a general base catalyst and accepts a proton from a water molecule. The deprotonated water molecule attacks the carbonyl carbon of the substrate. T191 and the zinc ion stabilize the intermediate. Finally, H265, as a general acid catalyst, protonates the nitrogen atom of the intermediately formed tetrahedral *gem*-diolate. Then, the C-N bond is cleaved. The products are formed [75, 76].
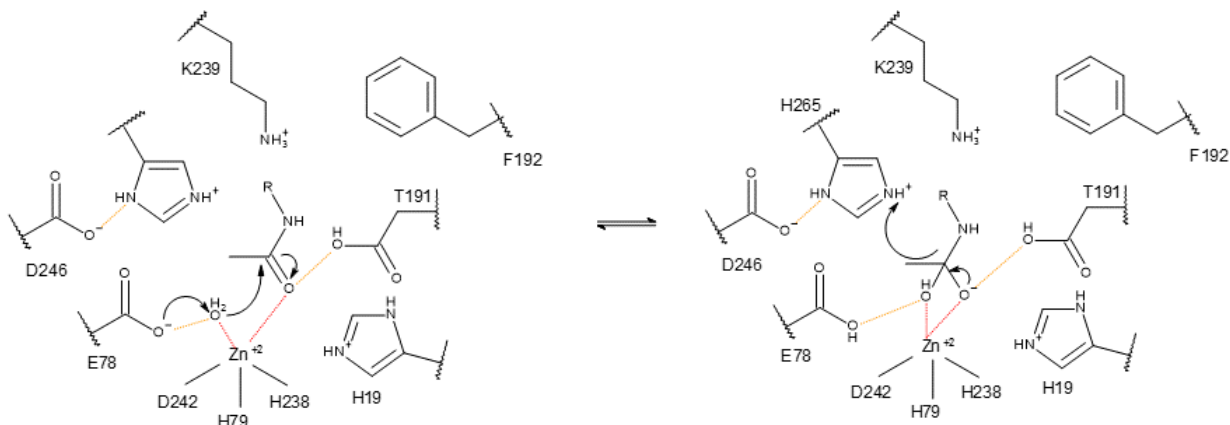
Figure 7. Catalytic mechanism of LpxC (adapted from [75, 76].)

1.3. Design of HDAC and LpxC inhibitors

1.3.1. Design of HDAC inhibitors

HDAC inhibitor researches have resulted in five approved anticancer drugs; vorinostat (SAHA), panobinostat, belinostat, romidepsin (FK228) and chidamide (Figure 8) [77-81]. Besides, many of them are in the clinical trial stages [82-84]. Vorinostat (SAHA) contains a hydroxamate group as a zinc binding group. It was approved for cutaneous T-cell lymphoma in October 2006 [85]. Thrombocytopenia and anemia are the most common reported side effects in patients who use Vorinostat (SAHA) [86]. Belinostat, which also has hydroxamate, was approved in July 2014 for peripheral T-cell lymphoma [87]. Belinostat had a limited effect on patients. Hematologic toxicities such as thrombocytopenia and anemia were reported as side effects of belinostat [88]. Another HDAC inhibitor with hydroxamate is panobinostat, which was approved in 2015. It is used against multiple myeloma [89]. Chidamide having benzamide as a zinc binding group was approved in 2014 for peripheral T-cell lymphoma [90]. Chidamide is a first orally active HDAC inhibitor with HDAC subtype selectivity for HDAC1, HDAC2, HDAC3 [83]. Romidepsin is a cyclic peptide. It was approved in 2009 for T-cell lymphoma [91]. Most of the developed HDAC inhibitors target multiple HDACs and might show unwanted side effects, such as hematologic side effects. Therefore, isoform-selective HDAC inhibitor design has gained attention.
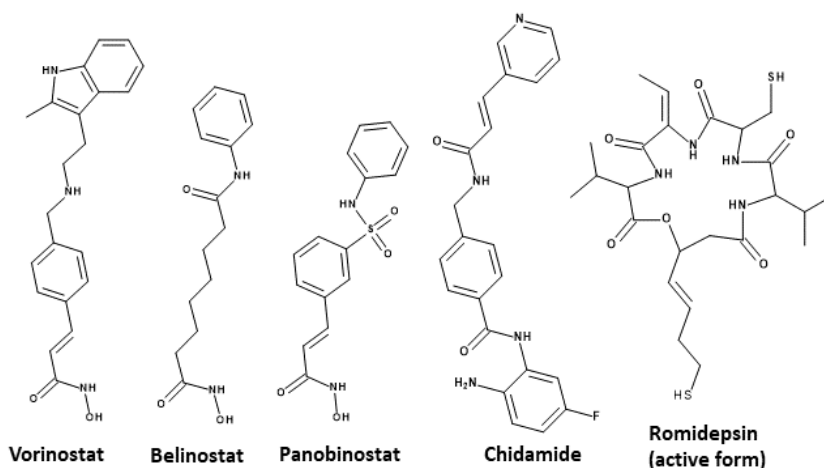
Figure 8. Approved HDAC inhibitors

Most HDAC inhibitors bind to the catalytic pocket, which can be divided into main pocket and sub-pockets. Main pocket consists of the acetate binding cavity, the substrate binding tunnel, and the rim of the pocket. The main pocket is observed in all crystal structures of HDACs. On the other hand, some isoforms of HDACs extend their catalytic pocket by sub-pockets such as side pocket, lower pocket and foot pocket (Figure 9). Accordingly, some inhibitors address these sub-pockets as well as the main catalytic pocket [23]. The sub-pockets could be in open-form or in closed-form depending on the bound ligand [92, 93].

The majority of the HDAC inhibitors occupy the main pocket, as shown for vorinostat in complex with HDAC2 (PDB ID: 4LXZ) (Figure 9A). The vorinostat binding mode reflects the classical binding mode for the HDAC inhibitors. This binding mode comprises three pharmacophoric features: a zinc binding group (ZBG), a linker group, and a cap group. The ZBG coordinates the zinc ion at the bottom of the pocket and prevents the binding of the substrates. The linker group is accommodated in the hydrophobic substrate binding tunnel. The cap group is placed at the rim of the pocket and is solvent-exposed [94, 95]. Besides, there are also inhibitors that target the sub-pockets of the catalytic pocket [23].

Increasing the potency and selectivity of the novel designed compounds is the priority for HDAC inhibitor design. The inhibitors targeting multiple HDAC isoforms may cause unwanted

side effects. The inhibition of a specific isoform instead of multiple isoforms may reduce the unwanted side effects of HDAC inhibitors [96].

Several strategies were developed to design selective HDAC inhibitors. The optimization of the ZBG is one of them. The majority of the HDAC inhibitors contain ZBG, which significantly contributes to the activity, selectivity and toxicity. ZBG fit into the acetate binding cavity and coordinates to the zinc ion at the bottom of the active site. So far, X-ray structures with various zinc binding groups have been released, including hydroxamic acid, 2-aminobenzamide, 2-substituted-benzamide, thiol, carboxylic acid, ketone, aryl ketone, amino acid derivatives, N-substituted hydroxamic acids [55, 97-106]. Hydroxamic acids are the most studied ZBG. The three of the approved drugs (Vorinostat (Figure 9A), Belinostat, Panobinostat) contain hydroxamic acid group as ZBG. These compounds show inhibitory activity on broad range of HDAC isoforms. The low K_i values for these compounds were observed against HDAC1-9: in the range of 20-173 nM for Vorinostat, 0.6-22 nM for panobinostat, 10-26 nM for belinostat [107]. Although hydroxamic acids are strong zinc binder and show high activity, they have poor pharmacokinetic properties and exhibit many off-target effects such as diarrhea, nausea [108, 109]. The replacement of the hydroxamic acid by other ZBG is the most promising strategy to design isoform selective HDAC inhibitors. The usage of 2-aminobenzamide as ZBG resulted in class I selective HDAC inhibitory activity due to addressing the foot pocket of the class I HDACs (Figure 9B). [100, 106, 110-114]. Chidamide, which is approved by the Chinese Food and Drug Administration for the treatment of T-cell lymphoma, contains 2-aminobenzamide group as ZBG and shows IC_{50} of 70-160 nM against HDAC1-3. Additionally, it shows less activity on HDAC8 (IC_{50} = 730 nM) and weak inhibitory activity (up to 30 μM) on HDAC4-7 and HDAC9 [83]. In addition to the 2-aminobenzamides targeting the foot pocket, the alkylhydrazide derivatives are also thought to be able to address the foot pocket of class I HDACs. Therefore, they show class I selectivity. So far, no X-ray structure was elucidated in complex with an alkylhydrazide derivative. The compound UF010 (2D and 3D representations were not shown) having the alkylhydrazide group as ZBG exhibits selectivity for HDAC1-3 over HDAC8 (3 to 25 fold), over class IIb HDACs HDAC6 and HDAC10 (18 to 250 fold) and class IIa HDACs HDAC4-5, 7 and 9 (>200 fold) [115].

In addition to the optimization of the zinc binding group, the optimization of the linker group and cap group can be used to design selective HDAC inhibitors. The linker and cap groups determine shape of the inhibitors; consequently, influences the activity and selectivity. Targeting the side pockets of HDAC isoforms resulted in isoform-selective HDAC inhibitors, as seen in HDAC8 [116-118] . HDAC8 side pocket is formed by L1 and L6 loop residues. In other HDACs, L1 and L6 loops have different conformation, hence this side pocket does not exist. The co-crystallized inhibitor (Figure 9C) in complex with *Schistosoma mansoni* HDAC8 (PDB ID: 6HTH [118]) having meta-substituted benzhydroxamic acid selectively inhibits *Schistosoma mansoni* HDAC8 with the IC_{50} of 75 nM, and human HDAC8 with the IC_{50} of 25 nM [116]. The inhibitor showed IC_{50} of 6.3 µM for HDAC1, and IC_{50} of 0.39 µM for HDAC6 [116]. The biphenyl group of the inhibitor forms hydrophobic contacts with the selectivity pocket of *Schistosoma mansoni* HDAC8 and of human HDAC8.

On the other hand, the lower pocket exists only in class IIa HDACs (Figure 9D). This lower pocket is formed due to the flipped-out conformation of a histidine residue (H974 in HDAC4 PDB ID 4CBY), which is replaced by the catalytic tyrosine residue in other HDACs (for example, Y303 in HDAC1, Y306 in HDAC8). For instance, the lower pocket was observed in one of the crystal structures of HDAC4 in complex with cyclopropylhydroxamic acid derivative (PDB ID: 4CBY) [119]. The co-crystallized inhibitor showed activity in a low nanomolar range on HDAC4-5, HDAC7, and HDAC9 with an IC_{50} of 30-190 nM and 300 to 11000-fold selectivity over HDAC1-3 and 90-fold selectivity over HDAC8 [119].
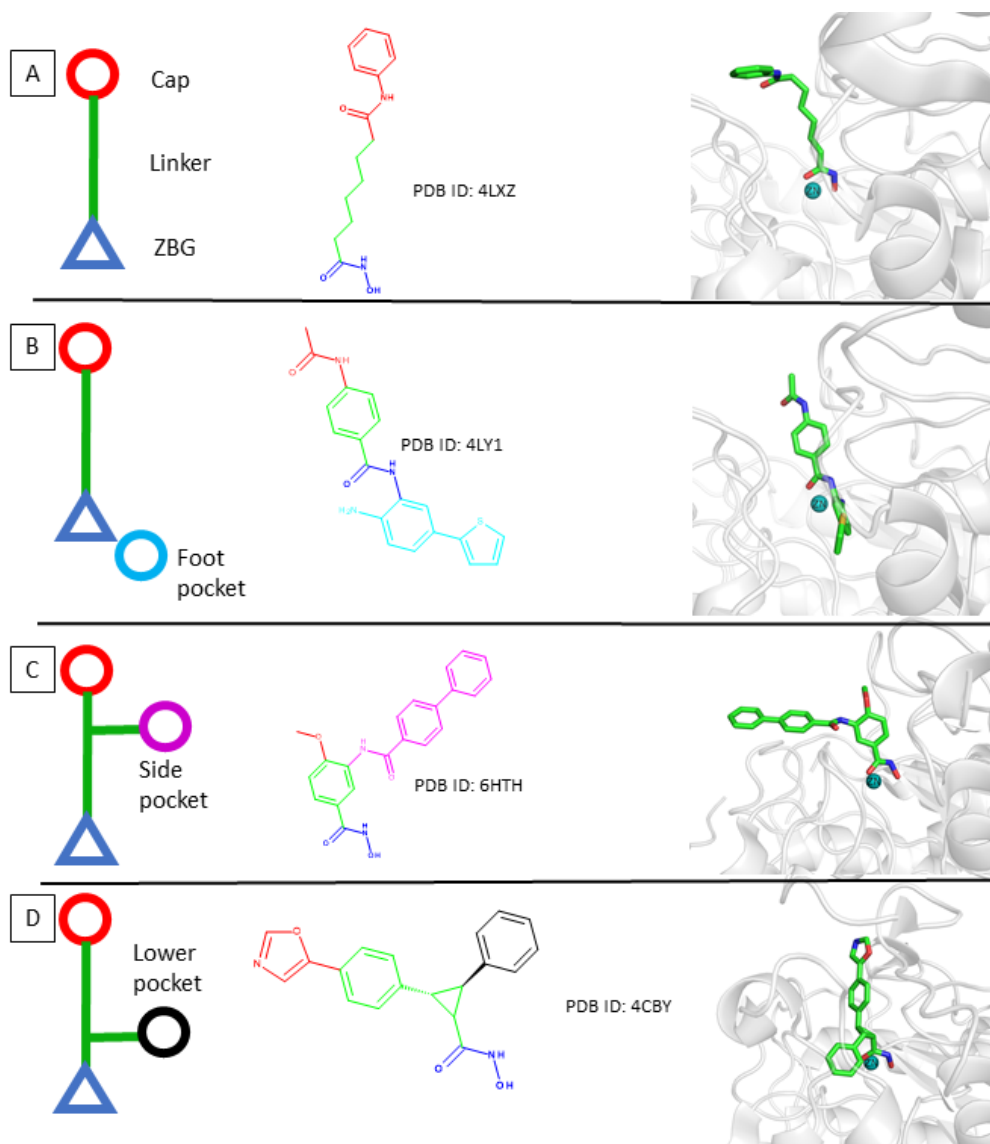
Figure 9. The pharmacophore models of the HDAC inhibitors. A) The compound having general pharmacophore model, B) the compound addressing the foot pocket, C) the compound addressing the side pocket, D) the compound addressing the lower pocket.

To sum up, multiple structure-based design strategies were developed to obtain HDAC inhibitors selective for different HDAC isoforms or classes. For example, targeting the foot pocket allows the obtaining of HDAC1-3 selective inhibitors, while targeting the side pocket results in HDAC8-selective inhibitors, and targeting the lower pocket gives access to class IIa selective inhibitors. These strategies can be used to develop novel HDAC inhibitors with better properties.

1.3.2. Design of LpxC inhibitors

LpxC is conserved in Gram-negative bacteria and does not show any sequence similarity to its mammalian isoforms such as deacetylases and amidases. Therefore, selectivity is not an issue for LpxC inhibitor design. Mainly, researchers focus on improving the potency of the inhibitors. So far, several potent LpxC inhibitors such as CHIR-090, TU514, and LPC-009 have been reported in the literature [71, 72, 74]. Similar to HDAC inhibitors, many LpxC inhibitors have a common pharmacophore consisting of a zinc binding group, a linker group, and a cap group (Figure 10A).
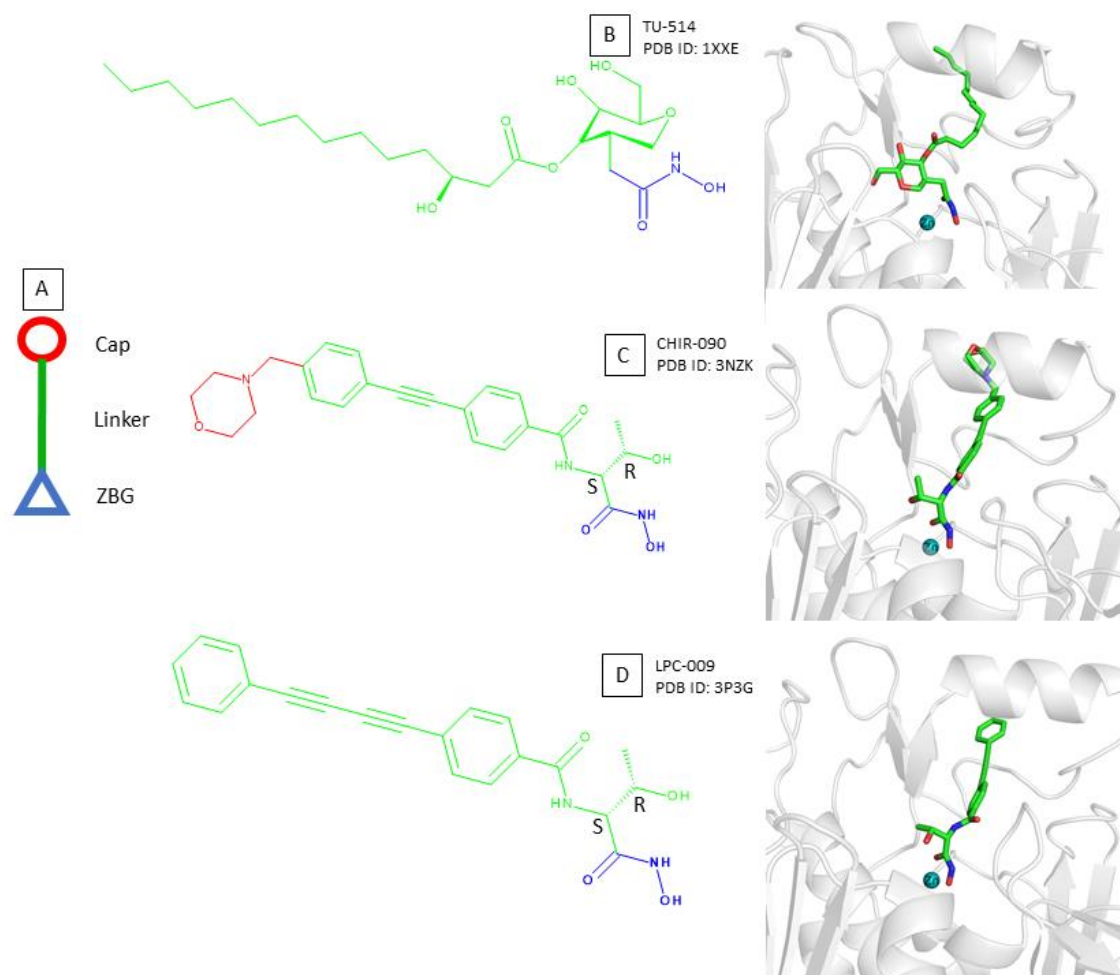
Figure 10. The pharmacophore models of the LpxC inhibitors.

The TU514 (Figure 10B), which was designed as a substrate analog by replacing the acetate with a hydroxamate, mimics the natural substrate of the LpxC [120] . TU514 showed high LpxC inhibitory activity with 650 nM at pH 5.5 and K_i of 1 nM at pH 7.4 against *Aquifex aeolicus* LpxC and 650 nM at pH 7.4 against *Escherichia coli* LpxC.

Compounds having *N*-aroyl-*L*-threonine-hydroxamate like CHIR-090, LPC-009 show potent LpxC inhibitory activity. CHIR-090 (Figure 10C), which was discovered by Anderson and coworkers in 2004 [69], is a slow and tight binding inhibitor with a K_i of 1 nM against *Aquifex aeolicus* LpxC and K_i of 1 nM at pH 7.4 against *Escherichia coli* LpxC. Additionally, it kills *Pseudomonas aeruginosa* effectively in bacterial disk diffusion assays [121]. However, CHIR-090 was found less effective against LpxC orthologs from the *Rhizobiacease* family (K_i of 0.34 μM against *Rhizobium leguminosarum*) [69]. Hence, the novel compounds based on a similar chemical scaffold to CHIR-090 compounds have gained significant interest. Among these studies, LPC-009 (Figure 10D), which is the diphenyl-diacetylene derivative of CHIR-090, enhanced the LpxC inhibitory activity over LpxC orthologs in minimum inhibitory concentration (MIC) assays (Table 3, [72]).

Table 3. MIC values of CHIR090 and LPC009 on different pathogens [72]

Pathogen	MIC (μg/ml)	
	CHIR-090	LPC-009
Escherichia coli	0.20	0.05
Pseudomonas aeruginosa	1.6	0.74
Salmonella typhimurium	0.16	0.024
Klebsiella pneumonia	0.64	0.10
Vibrio cholera	0.16	0.010
Bordetella bronchiseptica	16	2.0
Burkholderia cenocepacia	>32	32
Burkholderia dolosa	8.0	0.125

The overall binding mode of the inhibitors is similar. The X-ray structures of the LpxC-LPC-009 (PDB ID: 3P3G) revealed that a diphenyl-diacetylene group mimicking the fatty acyl

chain of the substrate penetrates through the hydrophobic substrate binding tunnel. The *N*-aroyl-L-threonine group mimicking the hexose group of the substrate binds to the hydrophobic patch of the enzyme which contains phenylalanine residues. The hydroxamic acid part chelates the zinc ion in a bidentate manner through its oxygen. More details of the binding mode will be discussed in the Results section.

The hydroxamic acid group is the strong zinc binder. Thus, it determines high LpxC activity. The glucose group of the substrate can be replaced by different groups, as seen in CHIR-090 and LPC derivatives having the *N*-aroyl-*L*-threonine group. The stereochemistry of the threonine group alters the LpxC activity. The (S)-configuration of position 2 in the threonine part is found to be critical for LpxC activity [72]. Additionally, the optimization of the threonine group allows the ligand to reach the hydrophobic patch and/or basic patch of the enzyme. The fatty acyl chain of the substrate can be mimicked by different linear chemical groups which can fit into the hydrophobic tunnel. Diphenylacetylene and diphenyldiacetylene scaffolds of CHIR-090 and LPC derivatives, respectively, showed enhanced antibiotic activity [72]. The addition of the chemical group to the distal part of the diphenylacetylene or diphenyldiacetylene influences the solubility of the compounds.

Thus, varying the linker and cap group was used to optimize the LpxC inhbitors and obtain more potent compounds.

2. AIM OF THE WORK

The aim of the current work was to design inhibitors for zinc-dependent enzymes, specifically HDACs and LpxC. The novel compounds should be more effective in vitro and in vivo, achieve isoform-selectivity, and have less toxicity and off-target effects. In order to achieve this aim, structure-based drug design techniques were applied in several scenarios.

The first project was to analyze the binding mode of inhibitors for the parasitic *Trypanosoma cruzi* histone deacetylase 2 (tcDAC2) enzyme and its human analogs in order to design selective tcDAC2 inhibitors. Docking studies were envisaged to be applied to understand the structure-activity relationship of the synthesized compounds, and proposals were made and *in silico* predicted.

In the second part of the work, the main focus was on human class I histone deacetylases HDAC1-3. Compounds having a 2-aminobenzamide warhead were studied and *in silico* optimized to achieve class I HDAC inhibitory activity. The goal was to design novel promising compounds using structure-based methods. The inhibitor binding modes were predicted by docking methods. Molecular dynamics simulations were performed to understand the impact of protein-ligand interactions. A quantitative structure activity relationship (QSAR) model based on the binding free energy calculations was established to design new molecules that gain selectivity among class I HDACs.

The third part of the work, similar to the second one, aimed to solve the selectivity problem among the class I HDACs using another zinc-binding group. Alkylhydrazide based HDAC inhibitors served as a starting point to acquire isoform-selective class I HDAC inhibitors. Docking of the known inhibitors could provide a general idea of the binding mode of alkylhydrazide which was later confirmed by enzyme kinetic studies. The protein-ligand interactions were analyzed by performing molecular docking studies and molecular dynamics simulations.

In the last part of the work, the main focus was to inhibit another zinc-dependent enzyme, LpxC. In order to achieve more potent LpxC inhibitiors, it was planned to design novel

hydroxamic acid derivatives mimicking the LpxC enzyme-substrate. The structure-activity relationship and the binding modes of the synthesized compounds were investigated by applying docking and molecular dynamics simulations.

3. METHODS AND MATERIALS

3.1. Computer-Aided Drug Design

Drug design projects are experimentally carried out with the aim of finding novel compounds. It is time-consuming and costly. Computer-aided drug design techniques reduce the time and cost. Computational methods can be applied to generate ideas and predictive models that can guide drug design projects to find the most promising ligands. For this aim, structure-based drug design methods, including molecular docking, molecular dynamics simulations, and binding free energy calculations, were applied in this project [122].

3.2. Molecular Docking

Molecular docking is a widely used structure-based drug design technique if the 3D (three-dimensional) protein structure is available [123]. It is a low cost technique that aims to predict the binding modes of ligands in the protein target. Docking programs are used for two main aims. First, the binding pose of the ligand can be predicted for a protein target. The prediction results are helpful in order to understand the structure-activity relationship of the compounds with the target protein. Secondly, the results are scored and ranked based on their binding affinity assessment. Nevertheless, scoring binding affinity by molecular docking tools is still challenging [124]. Docking programs do not usually consider solvent effects and protein flexibility. Hence, accurate binding pose prediction needs a more advanced evaluation [125]. To overcome the protein flexibility problem, different methods can be used [126].

- Induced fit docking; this method regards protein and ligand as flexible. But it is time consuming for large databases.
- Rotamer libraries; the side chain rotamer of the aminoacids can be generated.
- Ensemble docking methods; The compounds can be docked to multiple crystal structures using this method.
- Molecular dynamics simulations: this method can generate the different conformations of a protein.

In addition to the problems mentioned above, the possible isomers of the ligand, different tautomeric forms, and structures of the ligand can be corrected and adjusted using the ligand preparation tools.

In this work, the protonation and tautomeric forms of the ligand structures were prepared at pH 7.4 using the OPLS3e forcefield [127] in the Ligprep module of the Schrödinger suite [128]. Then, the output structures were subjected to the Confgen module by generating a maximum of 64 conformers and minimizing the output conformers [128].

The crystal structures of the proteins were downloaded from the protein data bank (PDB, rcsb.org) [53] and prepared using the protein preparation wizard in Schrödinger [128]. The missing side chains and hydrogens were automatically added, and bond orders were assigned. The solvent molecules, except conserved water molecules, were removed. All ions except the catalytic zinc ion were deleted. The protonation states of the ligands and residues were optimized at pH 7.4. Subsequently, the protein-ligand complexes were minimized using the OPLS3e forcefield in the Schrödinger program [127, 128].

The original ligand was used to define the active site of the protein. A radius of 10 Å was used to define the receptor grid box. Standard precision (SP) mode was used in Schrödinger [128]. Post-docking minimization was done for ten docking poses. The other settings were set as default. The obtained docking poses were visualized in the MOE program [129].

3.3. Molecular Dynamics Simulation

Molecular dynamics (MD) simulation investigates how every atom in a protein behaves over time based on interatomic interactions [130]. These simulations give an insight into some important biological processes, including conformational change, ligand binding, and protein binding. The MD simulations have been carried out for different purposes:

- To assess the stability of the predicted binding pose of the ligand in the protein
- To evaluate the stability of the protein-ligand interactions by distance analysis
- To calculate the binding free energies of bound and unbound protein-ligand complexes to rescore the binding affinities.

The selected docking poses of the compounds were subjected to MD simulation in AMBER16 [131]. Antechamber package was used to prepare the topologies, force field parameters, atom types and bond types by applying the semi-empirical Austin Model1 with bond charge correction (AM1-BCC) [132, 133]. Then, the tLEaP module was employed to prepare the protein-ligand complexes. General amber force field (GAFF), the Duan et al. force field (ff03.r1) and the 12-6-4LJ ionic model were used for ligand, protein and zinc ion, respectively [134-137]. The system was solvated by TIP3P solvent model and a margin of 10 Å. Two minimization steps, including the two sub-steps in each minimization, were carried out. In the first step, 4000 iterations (2000 cycles of steepest descent and then 2000 conjugate gradient) were performed, while the protein residues, ligand and zinc ion were restrained to their initial geometries (force constant of 10 kcal*mol^{-1}* Å^{-2}) to relieve the bad contacts. Only solvent molecules were minimized. In the second step, 4000 iterations (2000 cycles of steepest descent and then 2000 conjugate gradient) were performed to remove the steric clashes in the entire complex. The restraint on the protein, ligand and zinc were removed during the second minimization. Then, the system was heated at 300 K through 100 ps of MD. The protein-ligand complex was restrained to prevent large structural deviations (force constant of 10 kcal*mol^{-1}* Å^{-2}). The SHAKE algorithm was activated to constrain the bonds involving hydrogens [138]. Finally, the system was equilibrated for a period of 200 ps. The Langevin dynamics were applied to keep the temperature of 300 K with a collision frequency of 2 ps [139]. The pressure was kept at 1 bar using isotropic position scaling with a relaxation time of 2 ps. Afterwards, a 50 ns MD simulation was run with a time step of 2 fs using the same conditions as in the equilibration step. A non-bonded cut-off distance was set to 10 Å. The electrostatic interactions were calculated by applying the particle mesh Ewald (PME) method. MD snapshots were written every 2 fs. After the MD simulation, the CPPTRAJ module of AMBER was used to analyze the MD snapshots.

3.4. Binding Free Energy Calculation

Molecular docking tools can correctly predict the binding pose of the compounds. However, the correct ranking of docking poses needs an advanced method. Compared to molecular docking methods, the binding free energy calculation methods consider the solvation effect and conformational flexibility of protein and ligand [140].

Binding free energy can be calculated using pathway methods or endpoint methods. Pathway methods cover free energy perturbations (FEP) [141] and thermodynamic integration (TI) [142, 143]. The FEP and TI methods calculate the absolute binding free energy based on molecular dynamics (MD) simulation and thus consider the enthalpy changes, entropy changes, conformational flexibility, and desolvation effects [144, 145]. Endpoint methods include Molecular Mechanics-Generalized Born/Poisson-Boltzmann Surface Area continuum solvation (MM-GB/PBSA) [146, 147] and Linear Interaction Energy (LIE) [148, 149]. The endpoint methods approximately calculate the binding free energy by evaluating the initial and final states of the system [144]. Several studies have reported that the MM-GBSA and MM-PBSA methods can successfully be used to estimate the binding affinity of the protein-ligand complexes. Satisfactory correlations have been obtained between experimental data and predicted data for congeneric series [150-154].

Binding free energy (BFE) calculations were done for the docked inhibitors in the AMBER16 program [131]. The MMPBSA.py script was used for BFE calculations. Different solvation models (GB ^{HCT} (igb = 1), GB ^{OBC} (igb = 2), GB ^{OBC2} (igb = 5), and GBn (igb = 8) as well as PB_mbondi (mbondi) and PB_parse (parse)) were tested [155-159]. The MMGB(PB)SA methods combine molecular mechanics and solvent models. In addition, the binding free energy results were evaluated by considering six different systems:

- single frame after the first minimization step (Emin1),
- single frame after the second minimization step (Emin2),
- 1-50 frames during MD with an interval of 5 (MD-1),
- 51-100 frames during MD with an interval of 5 (MD-2),
- 101-500 frames during MD with an interval of 5 (MD-3),
- the single frame after the third minimization after MD (Emin3).

The binding free energies of protein-ligand complexes can be obtained from the difference between complex energy and the sum of the protein and ligand components (eq. (1)) [153, 154, 160].

$\Delta G_{bind} = G_{complex} - (G_{protein} + G_{ligand})$ (1)

The binding free energies in eq (1) can be obtained as the sum of the gas phase energy (E_{MM}), free solvation energies (ΔG_{sol}) and entropy ($-T\Delta S$) (eq. (2)) [154, 160, 161].

$$G_{molecule} = E_{MM} + \Delta G_{sol} - T\Delta S \quad (2)$$

The molecular mechanic energy (E_{MM}) is calculated as the sum of E_{int} (internal), E_{ele} (electrostatic), E_{vdv} (van der Waals). The internal energies (E_{int}) calculate the bond, angle, and dihedral energies, while the electrostatic energies (E_{ele}) consider the interactions between atoms occurring as a result of positive and negative atomic charges. Van der Waals (E_{vdv}) interactions consider the short and long ranged interactions among atoms. Solvation energies are the sum of polar solvent contributions ($G_{PB/GB}$) and non-polar solvent contributions (G_{SA}) (eq. (3)). [153, 154, 160, 161].

$$\Delta G_{bind} = (E_{int} + E_{ele} + E_{vdw}) + (\Delta G_{PB/GB} + \Delta G_{SA}) - T\Delta S \quad (3)$$

The conformational entropy change ($-T\Delta S$) is often considered to determine the total binding free energies. The absolute temperature is expressed as T, and the entropy of the molecule as S. However, including the entropy changes in the BFE calculation increases the computational cost and does not always improve the accuracy of the calculation [153, 154, 160, 162]. Hence, the conformational entropy change was not included in the calculation. Only enthalpy values (ΔH) were considered to find the correlation between binding enthalpies and biological data (eq. (4)).

$$\Delta H = (E_{MM}) + (\Delta G_{sol}) \quad (4)$$

3.5. Biological evaluation

3.5.1. Hydroxamic acid derivatives as parasitic HDAC inhibitors

The activities of the compounds designed as tcDAC2 inhibitors were determined as described by Marek et al. [64].

The tcDAC2 inhibitory activities of the compounds were tested using the fluorogenic substrate ZMTFAL(Z-(F3Ac)Lys-AMC) in ½ areaPlate-96 F microplates (PerkinElmer) as described previously [163]. 12.5 µL of assay buffer were prepared with 15 mM Tris, pH 7.5, 50 mM KH_2PO_4, 3 mM $MgSO_4 \cdot 7 H_2O$ and 10 mM KCl. Then, 10 µL enzyme solution, 2.5 µL of increasing concentrations of inhibitors in DMSO and 5 µL of the fluorogenic substrate ZMTFAL(Z-(F3Ac)Lys-AMC) were added to the assay buffer. In total, 30 µL solution was incubated for 90 min at room temperature (37 °C). Meanwhile, 2.5 µL Trichostatin A (TSA) (33 µM) and 5 µL trypsin (6 mg/mL) in trypsin buffer (50 mM Tris HCl, pH 8.0, 100 mM NaCl) were prepared and added to the stop solution. In total, 30 µL stop solution was added to the 30 µL solution including enzyme solution after first incubation. Then, the 60 µL solution was incubated again for 30 min at room temperature. After the incubation, the fluorescence intensity was measured on a BMG LABTECH POLARstar OPTIMA plate reader with excitation at λ = 390 nM and emission at 460 nM. The IC_{50} values of the compounds were determined with Origin Pro (version 9.0.0, Northampon, Massachusetts) [64].

The HDAC1 activities of the compounds were measured using the human recombinant HDAC1 assay as described before [164]. The incubation buffer was prepared with 50 mM Tris-HCl, pH 8.0, 137 mM NaCl, 2.7 mM KCl, 1 mM MgCl2 and 1 mh/ml bovine serum albumin. In incubation buffer, 52 µL enzyme solution was prepared and then combined with 3 µL of increasing concentrations of inhibitors in DMSO and 5 µL of fluorogenic substrate ZMAL (Z-(Ac)Lys-AMC, 126 µM). In total, 60 µL assay was pipetted into OpTiPlateTM-96 F black microplates (PerkinElmer) and incubated for 90 min at room temperature. After incubation, 60 µL of stop solution containing 5 µL Trichostatin A (TSA) (33 µM) and 10 µL trypsin (6 mg/mL) in trypsin buffer (50 mM Tris HCl, pH 8.0, 100 mM NaCl) was added. After the second incubation (30 min, 37 °C), the fluorescence was recorded on a BMG LABTECH POLARstar OPTIMA plate reader with excitation at λ = 390 nM and emission at 460 nM.

The HDAC8 activities of the compounds were measured using the Fluor-de-Lys (FDL) drug discovery kit. The 15 µL enzyme solution, inhibitor in increasing concentration (10 µL) and 25 µL of FDL substrate solution were pipetted into ½ AreaPlate-96 F microplates (PerkinElmer). The mixture was incubated for 90 min at room temperature. The 50 µL developer solution was added to it. After the second incubation (45 min, 30 °C), the fluorescence was detected on a

BMG LABTECH POLARstar OPTIMA plate reader with excitation at λ = 390 nM and emission at 460 nM.

3.5.2. In vitro testing of 2-aminobenzamide and alkylhydrazide derivatives as class I HDAC inhibitors

The activities of 2-aminobenzamide derivatives were determined as described in the published article [114].The in vitro HDAC activities of the compounds containing 2-aminobenzamides were measured using the recombinant HDAC1, HDAC2 and HDAC3/NCOR1 (purchased from ENZO Life Sciences AG (Lausen, CH)) with a fluorogenic peptide derived from p53 (Ac-RHKK(Acetyl)-AMC). Assay buffer were prepared with 50 mM Hepes, 150 mM NaCl, 5 mM MgCl$_2$, 1mM TCEP and 0.2 mg/ml BSA, at pH 7.4. The inhibitors at different concentrations were incubated for 5 minutes with final concentrations of 10 nM HDAC1, 3 nM HDAC2 or 3 nM HDAC3. The fluorogenic substrate was added to the mixture. The 20 µM final concentration was incubated for 90 min for HDAC1, 30 min for HDAC2 and 30 min for HDAC3. Stop solution containing 1 mg/mL trypsin and 20 µM SAHA in 1 mM HCl was added to stop the reaction. After the second incubation (60 min, 37 $^{\circ}$C), the fluorescence was measured with an Envision 2104 Multilabel Plate reader (PerkinElmer, Wlatham, MA, USA) with excitation at λ = 380 nM and emission at 430 nM. Then, the IC$_{50}$ values were measured.

The HDAC8 activities of the compounds were recorded by using a fluorescence assay as reported previously [117]. The fluorogenic substrate ZMAL (Z(ac)Lys-AMC) and enzyme and increasing concentrations of inhibitors were incubated for 90 min at room temperature. Fluorescence was recorded with excitation at λ = 390 nM and emission at 460 nM in a BMG Polarstar plate reader.

3.5.3. In vitro testing of LpxC inhibitors

LpxC activities of the compounds were determined by using fluorescence-based microplate assay as described previously [165-167].

28

The 93 µL UDP-3-O-(R-3-hydroxymyristoyl)-N-acetylglucosamine (29 µM) in assay buffer (40 mM sodium morpholinoethanesulfonic acid, 80 µM dithiothreitol, 0.02 % Brij 35 at pH 6.0) was pipetted into 96 well fluorescence microplate (Greiner Bio One, Frickenhausen). To assay the inhibitors at final concentrations from 0.2 nM up to 200 µM, 2 µL of respective dilution of the compounds in DMSO was added. Then, the 5 µL of a solution of purified LpxC (50 µg · ml^{-1}) was added to the assay buffer. The mixture was incubated for 30 min at 37 °C. The stop solution with 40 µL of 0.625 M sodium hydroxide. The mixture is incubated again for 10 min and neutralized by adding 40 µL of 0.625 M acetic acid. The deacetylated product UDP-3-O-(R-3-hydroxymyristoyl)-N-acetylglucosamine was converted into a fluorescent isoindole by adding 120 µL of 3 mM o-phthaldialdehyde-2-mercaptoethanol in 0.1 M borax. Fluorescence was detected with excitation at $\lambda = 340$ nM and emission at 460 nM in a Tristar plate reader (Berthold, Bad Wildbad). The IC$_{50}$ values were calculated via Probit-log concentration graphs in origin software.

4. RESULTS AND DISCUSSION

4.1. Design of inhibitors for the parasitic enzyme tcDAC2

4.1.1. Structural analysis of tcDAC2

Class I HDACs (HDAC1, 2, 3, and HDAC8) show phylogenetic resemblance to tcDAC2 more than other isoforms. Therefore, we have started by comparing the crystal structures of human HDACs (exemplified by HDAC1 and HDAC8 isoforms) and tcDAC2.

The available tcDAC2 crystal structures (PDB ID: 7Q1B in a complex with quisinostat and 7Q1C in a complex with TB56 [64]), HDAC1 crystal structure (PDB ID: 5ICN in a complex with a peptide [168]) and HDAC8 (PDB ID: 2V5X, in a complex with an inhibitor [169]) were retrieved from the protein data bank (PDB, rcsb.org, [53]). The analysis of tcDAC2, HDAC1 and HDAC8 revealed some similarities and differences (Figure 11). The catalytic pocket in both tcDAC2 and human isoforms consists of an acetate binding cavity, substrate binding tunnel and rim of the pocket. The zinc ion is found at the bottom of the catalytic pocket and coordinated by D237, D328 and H239 in tcDAC2 (D176/D178, D264/D267 and H178/H180 in HDAC1/8, respectively). The conserved residues H197, H198 and Y371 are located in the zinc binding region in tcDAC2 (H140/142, H141/143, and Y303/306 in HDAC1/8, respectively). The F207 and F267 (F150/152 and F205/208 in HDAC1/8, respectively) form a substrate binding tunnel (known as a hydrophobic tunnel) in tcDAC2. The acidic residue E156 is placed on the surface of tcDAC2, where the acidic residues D99/101 are found in HDAC1/8, respectively.

In addition to these similarities, crucial differences were observed between tcDAC2 and human isoforms (Figure 11). Notably, the unique R196, which is not found in other human HDAC isoforms (replaced by L139/W141 in HDAC1/8, respectively), is found at the acetate binding pocket (called foot pocket) and increases the charged character in the foot pocket region of tcDAC2. This pocket can be used to design selective-tcDAC2 inhibitors. In HDAC1-3, the hydrophobic residues make the foot pocket narrower, while, in HDAC8, its size and volume can change depending on the conformations of W141. Another crucial difference is observed in the hydrophobic tunnel. The tcDAC2 contains a unique selectivity pocket consisting of L335 and I266. Similarly, HDAC8 has a unique selectivity pocket consisting of M274 and the catalytic tyrosine Y306. However, location, shape and size of the pocket and the residues which

fill it are different in HDAC8 and tcDAC2. This pocket does not exist in HDAC1-3. The I266 in tcDAC2 is altered by bulky phenylalanine and tyrosine residues in HDAC1/8 (Y204 in HDAC1 and F207 in HDAC8). The hydrophobic L335 in tcDAC2 is changed by M274 in HDAC8. In the deeper part of the unique pocket in tcDAC2, A261 and A337 are observed to replace K200/K202 and C273/S276 in HDAC1/8, respectively. This unique pocket can be targeted to achieve selectivity for tcDAC2. Additionally, R439 increases the charged character of the unique pocket in tcDAC2.
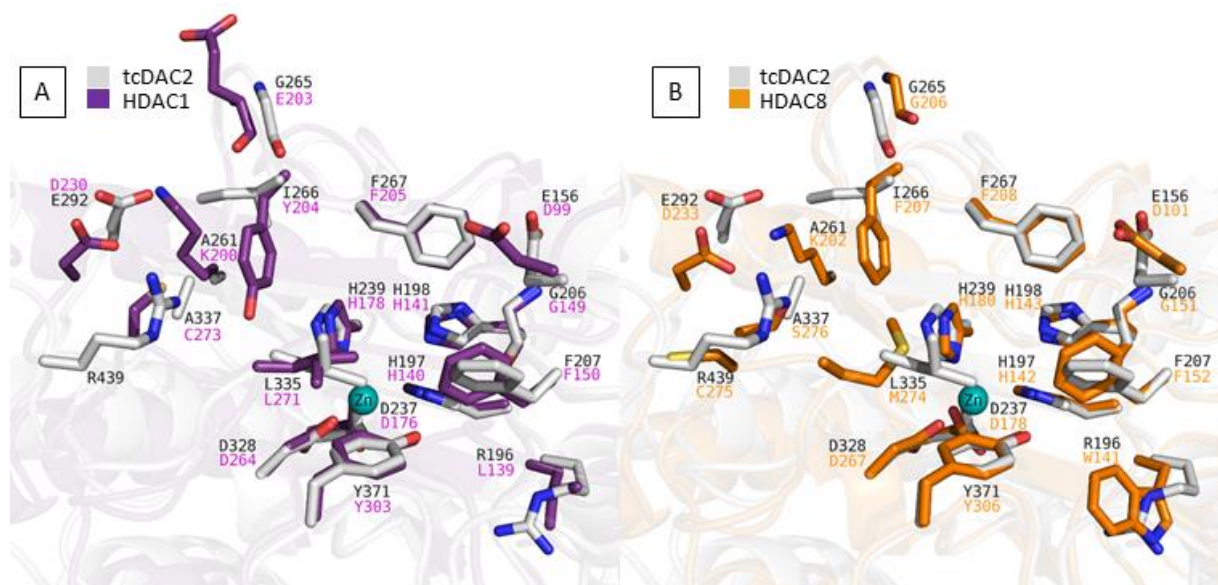
Figure 11. Comparison of tcDAC2 – HDAC1 and HDAC8. A) Comparison of tcDAC2 (PDB ID: 7Q1B) (white coloured carbon and ribbons) and HDAC1 (PDB ID: 5ICN) (purple coloured carbon and ribbons) B) comparison of tcDAC2 (PDB ID: 7Q1B) (white coloured carbon and ribbons) and HDAC8 (PDB ID: 2V5X) (orange coloured carbon and ribbons). Zinc ion was showed as cyan sphere.

In the next step, we have analyzed the binding mode of the co-crystallized ligands, quisinostat and TB56, in tcDAC2 (Figure 12). Both inhibitors possess a hydroxamic acid moiety as a warhead which coordinates the catalytic zinc ion through its carbonyl and hydroxyl oxygens. Moreover, this moiety makes hydrogen bond interactions with the conserved residues H197, H198 and Y371. The rigid pyrimidine-piperidine linker group of quisinostat is sandwiched between F207 and F267 by making π-π interactions. The C-N-C (secondary amine) linking group between pyrimidine and indole is able to make water-mediated H-bond interactions with E156. The indole cap group is solvent-exposed on the surface and stacked on F267. It is noticed that the quisinostat does not interact with the unique pocket of tcDAC2. In contrast to quisinostat, TB56 occupies the entrance of the unique pocket, consisting of L335

31

and I266. Besides, the dibenzofuran moiety of TB56 makes π-π interactions with F207 and F267 (Figure 12C).
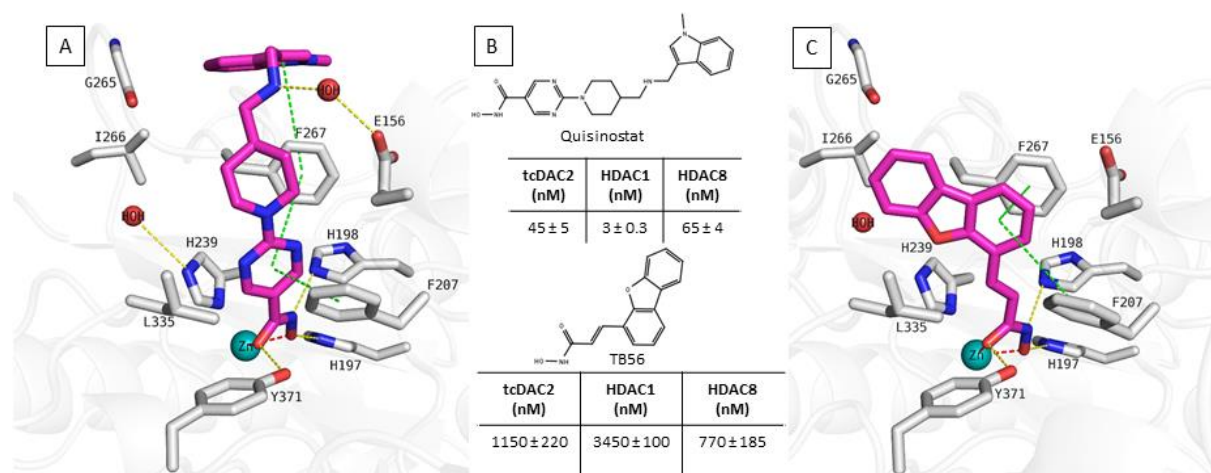
Figure 12. Binding mode of quisinostat and TB56 in tcDAC2 as determined in. A) Quisinostat in tcDAC2 (PDB ID: 7Q1B). B) 2D representation and biological activity results of quisinostat and TB56. C) TB56 in tcDAC2 (PDB ID: 7Q1C). Ligands were shown as magenta carbon coloured in stick representation. Protein backbones were shown with white carbon colour. Ribbons were shown with white colour. The zinc ion is shown as cyan coloured sphere. The conserved water molecule is shown as red sphere.

4.1.2. Redocking and cross-docking studies in tcDAC2 crystal structures and redocking in HDAC1 and HDAC8

A redocking study in the tcDAC2, HDAC1 and HDAC8 crystal structures was conducted to find the docking protocol which is able to reproduce the binding mode of co-crystallized ligands (Figure 13). In the case of tcDAC2 (Figure 13A), quisinostat and TB56 were redocked into the corresponding X-ray structures (PDB ID: 7Q1B, 7Q1C, respectively). The docking protocol was adjusted for the hydroxamate form of the ligand without using constraints and by enhancing the planarity of conjugated pi groups. Additionally, all solvent molecules (except one conserved water molecule which interacts with H239 in tcDAC2, H178 in HDAC1 and H180 in HDAC8) were removed. The details of the docking protocol were explained in section 3.2. The redocking results were visually analyzed and evaluated based on the RMSD (root mean square error) between docked pose and its co-crystallized pose. The RMSD was calculated as 0.16 Å for TB56 and 0.35 Å for quisinostat. Both crystal structures gave good redocking results. But, tcDAC2 crystal structure in a complex with quisinostat (PDB ID:

7Q1B) was selected due to both good redocking results and the structural similarity between the designed compounds and quisinostat. The same docking protocol was applied for HDAC1 (PDB ID: 5ICN) and HDAC8 (PDB ID: 2V5X) crystal structures. In the case of HDAC1 (Figure 13B), the crystal structure (PDB ID: 5ICN) is complexed with a peptide having a hydroxamic acid warhead. Due to the flexible peptide structure, the RMSD of the docking pose was 1.68 Å with respect to the co-crystalized peptide. The visual analysis of the docking pose revealed that the hydroxamic acid moiety and alkyl linker group of the peptide are in good agreement with the co-crystallized ligand. In the case of the HDAC8 (Figure 13C), the co-crystallized ligand in a complex with an inhibitor having hydroxamic acid as zinc binder was chosen due to the structural similarity of the cap group and zinc binding group to the quisinostat. The indol group of the ligand interact with the F208 in HDAC8 (PDB ID: 2V5X) as observed for quisinostat in tcDAC2. The redocked pose shows good agreement with the co-crystallized ligand. The RMSD was measured as 1.21 Å. The solvent-exposed cap group shows different conformations on the HDAC8 surface, while the zinc binding group and linker group of the redocked pose match with the co-crystallized ligand of HDAC8 (PDB ID: 2V5X).
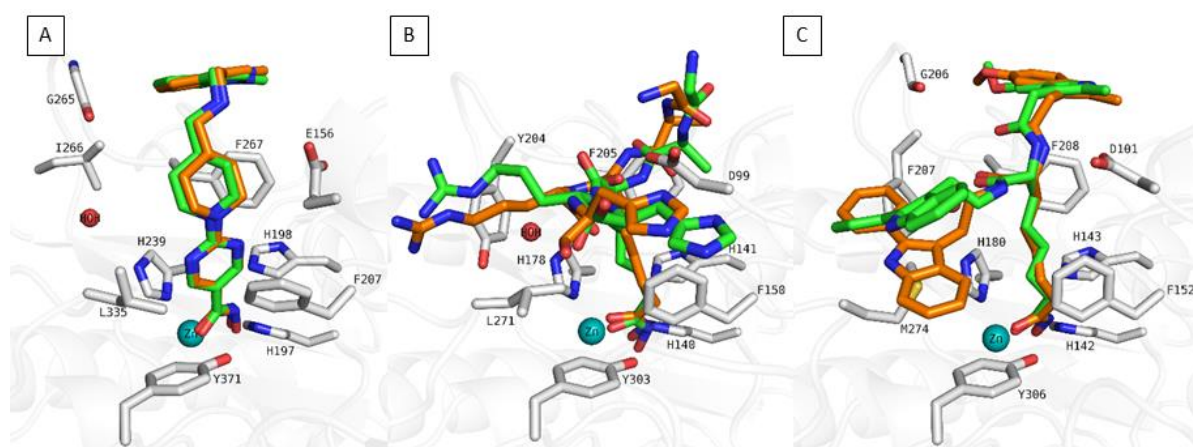
Figure 13. Redocking poses of co-crystallized ligands in tcDAC2 – HDAC1 – HDAC8. A) in tcDAC2 crystal structure (PDB ID: 7Q1B), B) in HDAC1 crystal structure (PDB ID: 5ICN) and C) in HDAC8 crystal structure (PDB ID: 2V5X). Protein backbone was shown as white ribbons. Important amino acid residues of the binding pocket were shown in stick representation with white carbon atoms. Ligands were shown as sticks with carbon atoms coloured in green for redocked pose and orange for co-crystallized ligand. Zinc ion was shown as cyan sphere, water molecules as red sphere.

4.1.3. Design of the compounds

In this part of the study, we designed novel compounds of five different series (Figure 14). The structures were created by combining the structural features of quisinostat and TB56 to acquire tcDAC2 selective inhibitors (Figure 14). The hydroxamic acid warhead was kept to make chelation with zinc ion as well as hydrogen bond interactions with neighboring residues. The piperazine or 1,4-diazepane was attached to the pyrimidine/benzothiophen ring in order to make the compounds more soluble. Different aromatic cap groups were attached to the piperazine or 1,4-diazepane moiety in order to maintain π-π interactions with F267 on the surface of tcDAC2 and to test their effect on the selectivity over HDAC1 and HDAC8. Additionally, we designed one series of compounds by replacing one nitrogen of pyrimidine with different substitutions to target the unique selectivity pocket of tcDAC2. In the last series, we removed the piperazine or 1,4-diazepane part. Instead, the rigid cyclopropane ring was used to change the direction of the cap groups.
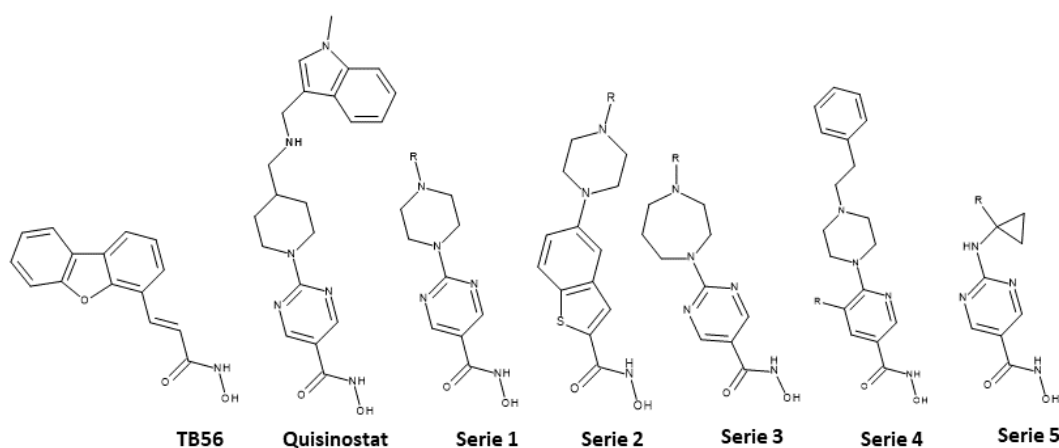
Figure 14. 2D representation of reference inhibitors and synthesized HDAC compounds

4.1.4. Docking of compounds

In total, 39 compounds were designed by modifying the aromatic linker as well as the capping group using the MedChem optimization tool in the MOE program. The compounds were then synthesized, and tested against tcDAC2, HDAC1, and HDAC8 (Table 4-8). Some of the them had nanomolar activity on tcDAC2 enzyme, while others were not as active as expected. To understand the structure-activity relationship (SAR) of the synthesized

compounds, molecular docking studies were carried out using crystal structures of tcDAC2 (PDB ID: 7Q1B), HDAC1 (PDB ID: 5ICN), and HDAC8 (PDB ID 2V5X).

Table 4. Inhibitory activity of first series of the synthesized compounds against tcDAC2 – HDAC1 – HDAC8.

Serie	Name	Substitutent	Inhibitory activity (IC$_{50}$, nM or % inhibition at a given concentration)		
			tcDAC2	HDAC1	HDAC8
1	1	H	3820 ±770	26 ± 6	550 ± 98
1	2		135 ± 19	5.5 ± 0.8	153 ± 27
1	3		105 ± 12	6.5 ± 0.4	107 ± 15
1	4		217 ± 63	9.18 ± 1.3	56 ± 6
1	5		148 ± 19	33 ± 2	65 ± 11
1	6		257 ± 17	156 ± 9	100 ± 23
1	7		497 ± 66	124 ± 15	185 ± 34
1	8		804 ± 101	31 ± 3	59 ± 7
1	9		329 ± 51	141 ± 29	170 ± 15
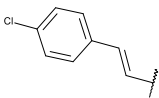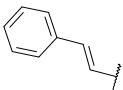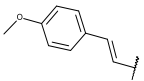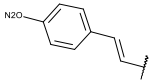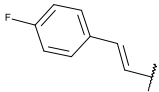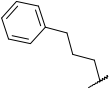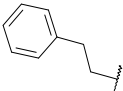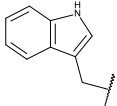
1	10		36 ± 2	13 ± 1	21 ± 3
1	11		57 ± 3	13 ± 0.8	208 ± 17
1	12	-CH₃	1530 ± 210	194 ± 73	234 ± 33
1	13		10 µM: 99 %	9.4 ± 0.5	56 ± 4
1	14		10 µM: 96 %	44 ± 4	133 ± 13
Ref	Quisinostat		45 ± 4	3 ± 0.3	65 ± 7
Ref	TB56		1150 ± 100	3450 ± 100	770 ± 50
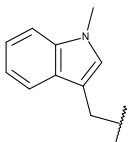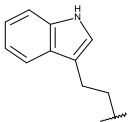
*nd: not determined

The first series of designed compounds (compounds 1-14 in Table 4) possessing different capping groups demonstrated similar binding poses in tcDAC2, HDAC1 and HDAC8. Compound 10 with an indole cap group showed higher inhibitory activity in tcDAC2 than other compounds (IC$_{50}$ 36 nM, 13 nM and 21 nM in tcDAC2, HDAC1 and HDAC8, respectively). The hydroxamic acid moiety of compound 10 binds to the zinc ion in a bidentate manner through its carbonyl and hydroxyl oxygen (Figure 15). Additionally, this moiety makes hydrogen bond interactions with conserved residues (H197/140/142, H198/141/143 and Y371/303/306 in tcDAC2, HDAC1 and HDAC8, respectively). The pyrimidine group is sandwiched between F207/150/152 and F267/205/208 in the hydrophobic tunnel of tcDAC2, HDAC1 and HDAC8, respectively. The basic piperazine group is located at the entrance of the binding pocket where it can interact with conserved acidic residues E156/D99/D101 in tcDAC2/HDAC1/HDAC8, respectively (not seen in tcDAC2 due to unfavorable E156 conformation in the solved crystal structure, but observed in MD simulation). The indole cap group is found on the surface of the pocket by making π - π interactions with F267/205/208 in tcDAC2/HDAC1/HDAC8, respectively. Additionally, the indole group of compound 10 is able to make hydrogen bond interactions with G265 and G206 in tcDAC2 and HDAC8, respectively. In HDAC1, it is in close proximity to E203 residues, which is also likely to provide a hydrogen bond.
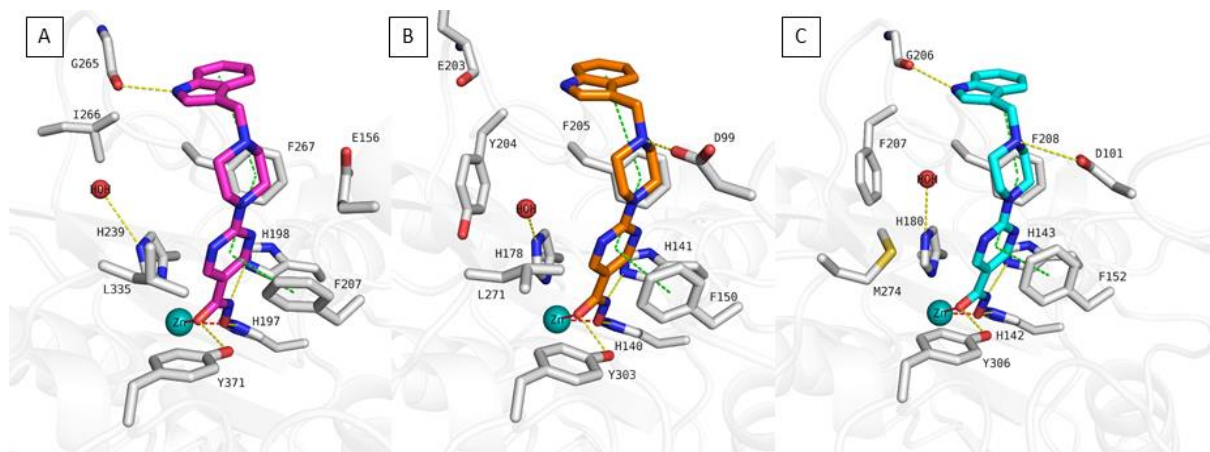
Figure 15. Docking poses of compound 10 (A, magenta coloured sticks) in tcDAC2 (PDB ID: 7Q1B), (B, orange coloured sticks) in HDAC1 (PDB ID: 5ICN), (C, cyan coloured sticks) in HDAC8 (PDB ID: 2V5X). Hydrogen bonds (yellow dashed lines), metal coordination (red dashed lines), and aromatic interactions (green dashed lines) between inhibitors and proteins are shown. Relevant residues are shown in stick representation with white carbon atoms in tcDAC2, HDAC1 and 8. The zinc ion is shown as cyan coloured sphere. The conserved water molecule is shown as red sphere.

Table 5. Inhibitory activity of second series of the synthesized compounds against tcDAC2 – HDAC1 – HDAC8.
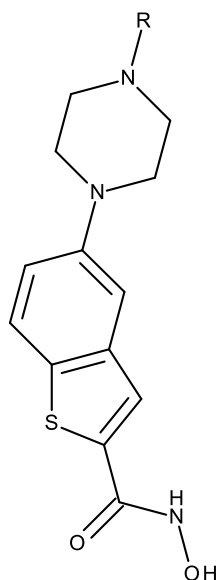
			Inhibitory activity (IC$_{50}$, nM or % inhibition at a given concentration)		
Serie	Name	Substitutent	tcDAC2	HDAC1	HDAC8
2	15	H	3870 ± 710	690 ± 37	493 ± 82

37
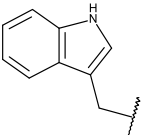
2	16		10 µM: 87.6 %	1100 ± 50	490 ± 68
2	17		10 µM: 78.3 %	6600 ± 300	1692 ± 186
2	18		10 µM: 81.9 %	610 ± 30	629 ± 79
2	19		10 µM: 71.7 %	2400 ± 100	769 ± 184
2	20		n.d	1700 ± 100	348 ± 99
2	21		n.d	840 ± 50	395 ± 41
2	22		n.d	620 ± 30	679 ± 69
Ref	Quisinostat		45 ± 4	3 ± 0.3	65 ± 7
Ref	TB56		1150 ± 100	3450 ± 100	770 ± 50
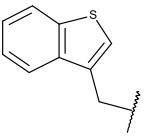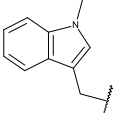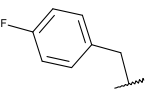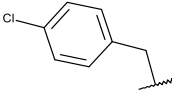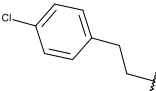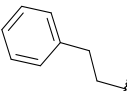
*nd: not determined

In the second series of compounds (compounds 15-22, Table 5), the pyrimidine linker group is replaced by a benzothiophene ring (Figure 16). This replacement increased the π - π interaction surface with F267/205/208 in tcDAC2/HDAC1 and HDAC8. However, in contrast to our expectation, compound 16, a benzothiophene derivative of compound 10, showed decreased inhibitory activity on all three enzymes. In the postulated binding mode of compound 16 in tcDAC2, it has been noticed that the benzothiophene ring fills the hydrophobic tunnel and causes the piperazine moiety to be placed further from the hydrophobic tunnel. The observed difference in the location of the piperazine ring on the surface of tcDAC2 might be responsible for the reduced tcDAC2 activity. This is because the new location of piperazine ring considerably increases its distance to potential interaction partners – the acidic residues E156/D99/D101 in tcDAC2/HDAC1/HDAC8, respectively. In the docking pose of HDAC1,

the piperazine is found 4.2 Å away from D99 and no more interaction was observed. In HDAC8, similarly, the D101 was 3.8 Å away and interaction was lost.
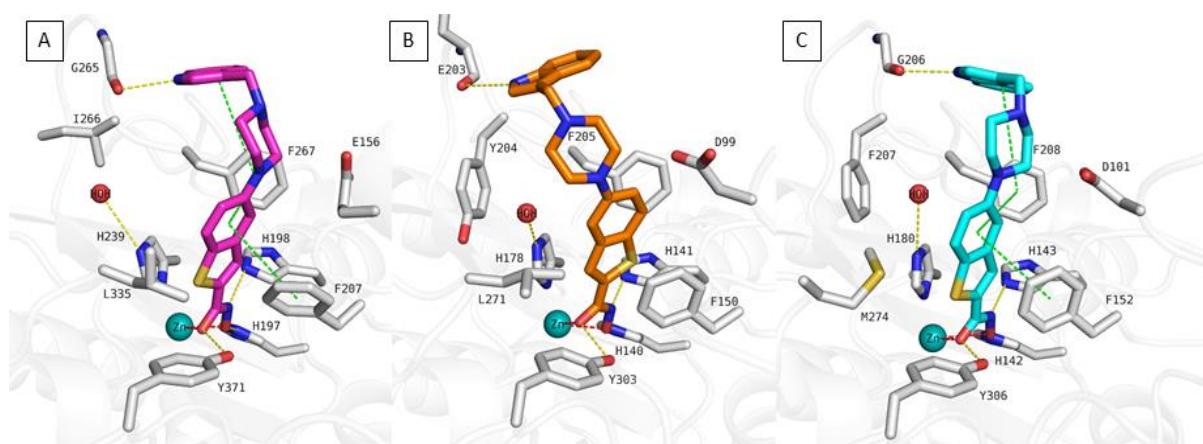
Figure 16. Docking poses of compound 16 (A, magenta coloured sticks) in tcDAC2 (PDB ID: 7Q1B), (B, orange coloured sticks) in HDAC1 (PDB ID: 5ICN), (C, cyan coloured sticks) in HDAC8 (PDB ID: 2V5X). Hydrogen bonds (yellow dashed lines), metal coordination (red dashed lines) and aromatic interactions (green dashed lines) between inhibitors and proteins are shown. Relevant residues are shown in stick representation with white carbon atoms in tcDAC2, HDAC1 and 8. The zinc ion is shown as cyan coloured sphere. The conserved water molecule is shown as red sphere.

Table 6. Inhibitory activity of third series of the synthesized compounds against tcDAC2 – HDAC1 – HDAC8.
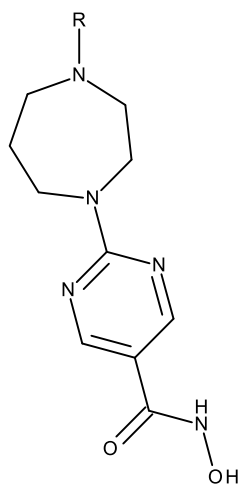
			Inhibitory activity (IC$_{50}$, nM or % inhibition at a given concentration)		
Serie	**Name**	**Substitutent**	**tcDAC2**	**HDAC1**	**HDAC8**
3	23	H	10 μM: 45.9 %	190 ± 10	61 ± 8

39
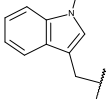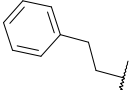
3	24		10 µM: 92.3 %	33 ± 1	105 ± 20
3	25		10 µM: 75.3 %	83 ± 5	99 ± 11
3	26		10 µM: 88.6 %	58 ± 3	10 µM: 97.7 %
3	27		10 µM: 76.0 %	330 ± 10	79 ± 12
3	28		n.d	32 ± 1	83 ± 10
3	29		10 µM: 90.9 %	150 ± 10	10 µM: 96.1 %
3	30		74 ± 4	26 ± 1	10 µM: 97.6 %
3	31		10 µM: 95.9 %	36 ± 1	52 ± 5
Ref	Quisinostat		45 ± 4	3 ± 0.3	65 ± 7
Ref	TB56		1150 ± 100	3450 ± 100	770 ± 50
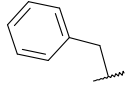
*nd: not determined

In the third series of designed compounds (compounds 23-31, Table 6) bearing a 1,4-diazepane ring (Figure 17), docking results are exemplified by compound 31, which is the 1,4-diazepine derivative of compound 10. The binding pose of compound 31 showed that the usage of the bulkier ring did not result in a significant difference in the binding mode. The tcDAC2 inhibitory activity was also high (almost 100 % at 10 µM), but the IC_{50} values were not determined.
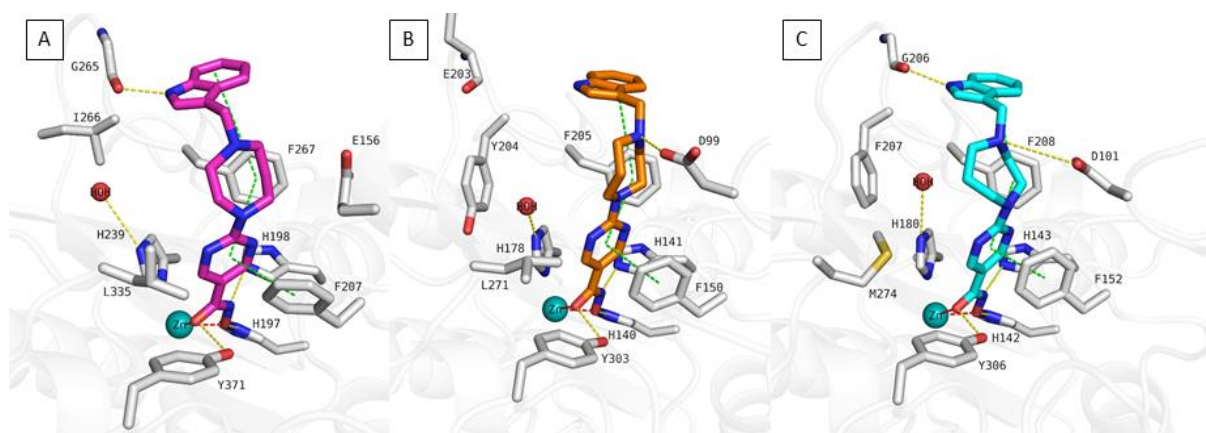
Figure 17. Docking poses of compound 31 (A, magenta coloured sticks) in tcDAC2 (PDB ID: 7Q1B), (B, orange coloured sticks) in HDAC1 (PDB ID: 5ICN), (C, cyan coloured sticks) in HDAC8 (PDB ID: 2V5X). Hydrogen bonds (yellow dashed lines), metal coordination (red dashed lines), and aromatic interactions (green dashed lines) between inhibitors and proteins are shown. Relevant residues are shown in stick representation with white carbon atoms in tcDAC2, HDAC1 and 8. The zinc ion is shown as cyan coloured sphere. The conserved water molecule is shown as red sphere.

Table 7. Inhibitory activity of fourth series of the synthesized compounds against tcDAC2 – HDAC1 – HDAC8.
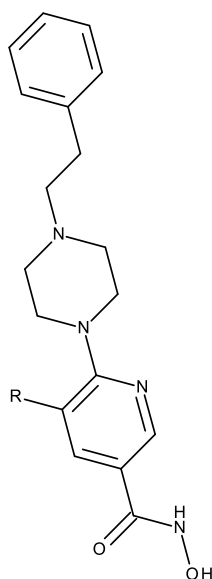
Serie	Name	Substitutent	Inhibitory activity (IC$_{50}$, nM or % inhibition at a given concentration)		
			tcDAC2	HDAC1	HDAC8
4	32		10 μM: 15.7 %	2300 ± 200	199 ± 36
4	33		10 μM: 13.5 %	1800 ± 200	530 ± 92

41

4	34		10 µM: 25.9 %	2700 ± 400	299 ± 30
Ref	Quisinostat		45 ± 4	3 ± 0.3	65 ± 7
Ref	TB56		1150 ± 100	3450 ± 100	770 ± 50

*nd: not determined

The first three series have been inspired by quisinostat, which is a broad spectrum HDAC inhibitor. The fourth series was created using the second solved X-ray crystal structure, which is in complex with TB56. This inhibitor is a cinnamic acid derivative containing dibenzofuran. Analysis of its binding mode revealed the dibenzofuran moiety of TB56 occupies the unique pocket consisting of I267 and L336 in tcDAC2 (Figure 12B). TB56 shows an IC_{50} of 1150 nM for tcDAC2 and 3450 nM for HDAC1. One of the unique pocket residues, Ile267 in tcDAC2, is replaced by the bulky Y204 in HDAC1. The bulky Y204 in HDAC1 moves the L271 a bit away (Figure 11A). Moreover, Y204 and L271 in HDAC1 form hydrogen bond interactions, which are not observed in tcDAC2. Then, we decided to utilize these structural differences to achieve selectivity for tcDAC2 versus HDAC1. The co-crystallized TB56, which occupies the unique pocket of the tcDAC2, shows selectivity over HDAC1 but is not highly active against tcDAC2. Hence, we designed new compounds (32-34, Table 7) by adding a small alkyl chain group to position-2 of the aromatic linker of compound 9 (IC_{50} 329 nM in tcDAC2, 290 nM in HDAC1, and 170 nM in HDAC8) in the fourth series (Table 4). The phenyl cap group in compound 32 makes π-π interactions with F268 in tcDAC2 as shown by the docking poses (Figure 18). The linker group is sandwiched between the phenylalanine residues in tcDAC2, HDAC1, and HDAC8. The new substitution on the linker group makes van der Waals interactions with L336 at the entrance of the selectivity pocket of tcDAC2. This pocket does not exist in HDAC1. In HDAC1, the bidentate zinc chelation was lost, which led to a decrease in HDAC1 inhibitory activity (IC_{50} 2300 nM). The docking results of TB56 and the fourth series showed us that the substituent aiming at the selectivity pocket of tcDAC2 also targets the selectivity pocket of HDAC8. Thus, as expected, the methoxy substituent of compound 32 occupied the selectivity pocket of HDAC8 and it showed high activity (IC_{50} 199nM). However, contrary to our expectation, tcDAC2 activity was lost (inhibition 10 µM: 15.7 %), although the methoxy substituent was postulated to interact with the selectivity pocket. It seems that the solvent effects might have played a big role in this case. The displacement of the conserved water molecule, which is required to enter the pocket, causes a large energy change. Furthermore, a suitable

substituent on the ligand is required to compensate for this change and maintain the biological activity.
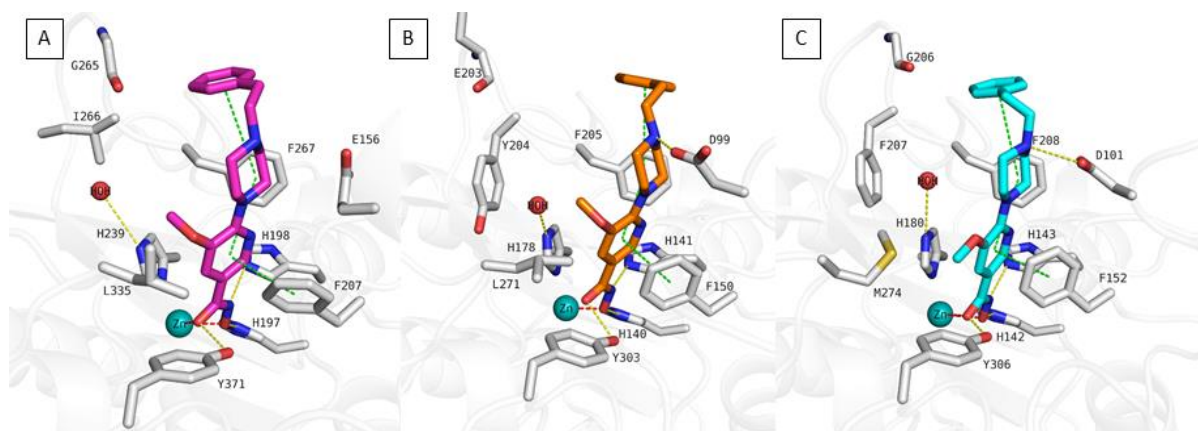
Figure 18. Docking poses of compound 32 (A, magenta coloured sticks) in tcDAC2 (PDB ID: 7Q1B), (B, orange coloured sticks) in HDAC1 (PDB ID: 5ICN), (C, cyan coloured sticks) in HDAC8 (PDB ID: 2V5X). Hydrogen bonds (yellow dashed lines), metal coordination (red dashed lines), and aromatic interactions (green dashed lines) between inhibitors and proteins are shown. Relevant residues are shown in stick representation as white carbon atoms in tcDAC2, HDAC1 and 8. The zinc ion is shown as cyan coloured sphere. The conserved water molecule is shown as red sphere.

Table 8. Inhibitory activity of fifth series of the synthesized compounds against tcDAC2 – HDAC1 – HDAC8.
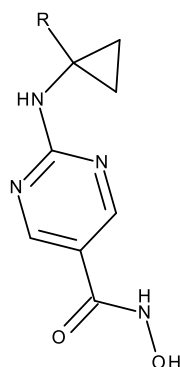
Serie	Name	Substitutent	Inhibitory activity (IC$_{50}$, nM or % inhibition at a given concentration)		
			tcDAC2	HDAC1	HDAC8
5	35		10 μM: 72.5 %	230 ± 10	10 μM: 92.7 %
5	36		10 μM: 73.3 %	190 10±	10 μM: 91.5 %
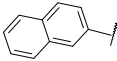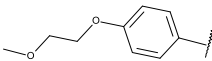
5	37		10 μM: 81.9 %	88 ± 2	10 μM: 95.4 %
5	38		910 ± 30	350 ± 20	1050 ± 235
5	39		150 ± 8	85 ± 2	857 ± 272
Ref	Quisinostat		45 ± 4	3 ± 0.3	65 ± 7
Ref	TB56		1150 ± 100	3450 ± 100	770 ± 50
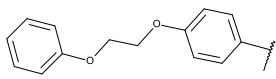
*nd: not determined

In the fifth series (compounds 35-39, Table 8), we designed new compounds to decrease HDAC1 and HDAC8 activity. Two modifications were made to the structures. First, the piperazine moiety of compound 9 was replaced by a rigid hydrophobic moiety to remove the D99/D101 interactions in HDAC1 and HDAC8, respectively. We were hoping that a more flexible E156 amino acid residue would still be able to make contact with a hydrophilic linker of the ligand. Additionally, a rigid cyclopropane moiety, which was used instead of piperazine, allows us to keep the compounds away from the selectivity pocket of HDAC8. Second, in tcDAC2, HDAC1 and HDAC8, a flexible cap group was used to make a π-π interactions with F267/205/208 (Figure 19). Biological testing revealed that the tcDAC2 activity of compound 39 (IC_{50} 150 nM) increased compared to compound 9 (IC_{50} 329 nM), but only the activity of HDAC8 (IC_{50} 857 nM) decreased compared to compound 9 (IC_{50} 170 nM). The HDAC1 activity of compound 39 (IC_{50} 85 nM) increased compared to compound 9 (IC_{50} 290 nM). More careful analysis revealed that E156/D99 in tcDAC2 and HDAC1 both have a more favorable orientation than D101 in HDAC8 in order to make contact with a hydrophilic linker of compound 39. This might explain the unexpectedly high activity on HDAC1.
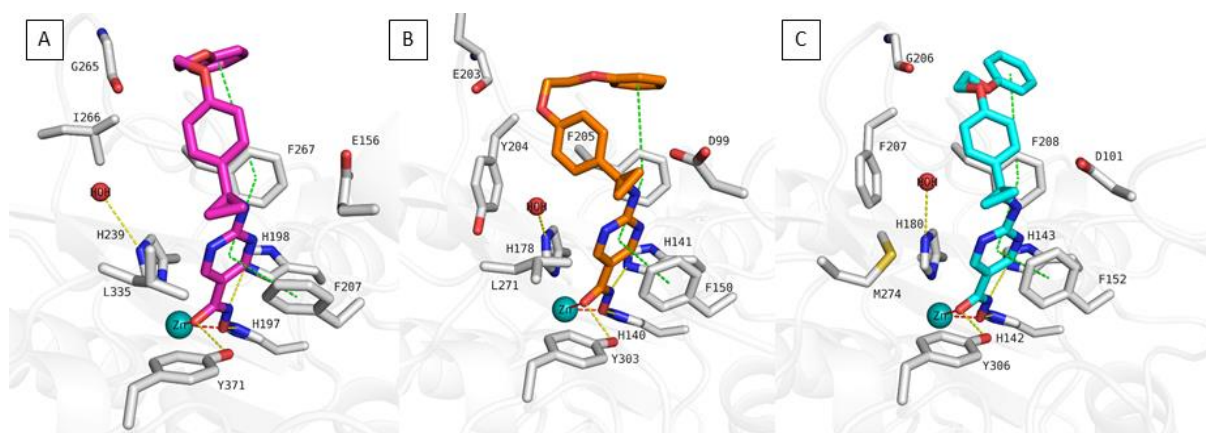
Figure 19. Docking poses of compound 39 (A, magenta coloured sticks) in tcDAC2 (PDB ID: 7Q1B), (B, orange coloured sticks) in HDAC1 (PDB ID: 5ICN), (C, cyan coloured sticks) in HDAC8 (PDB ID: 2V5X). Hydrogen bonds (yellow dashed lines), metal coordination (red dashed lines), and aromatic interactions (green dashed lines) between inhibitors and proteins are shown. Relevant residues are shown in stick representation as white carbon atoms in tcDAC2, HDAC1 and 8. The zinc ion is shown as cyan coloured sphere. The conserved water molecule is shown as red sphere.

To summarize the docking results, five series of compounds (39 compounds) have been designed, synthesized, and their binding modes have been analyzed. The compounds in the first three series do not show selectivity for tcDAC2, but they are highly active in tcDAC2. The fourth series of compounds, which is supposed to be selective over HDAC1, had indeed decreased activity on HDAC1. Unfortunately, the tcDAC2 activity of this series was also reduced. A more suitable substituent, which would effectively occupy the unique pocket of tcDAC2, is needed to maintain the tcDAC2 activity. In the fifth series, selectivity over HDAC1 and HDAC8 was attempted to be achieved. The ligands were made more rigid to reduce the possibility of occupying the selectivity pocket of HDAC8 and more hydrophobic to reduce interactions with acidic residues in HDAC1 and HDAC8 (compound 35-39). This strategy worked partially giving a compound (compound 39), which was highly active on tcDAC2 and HDAC1, but selective over HDAC8.

4.2. Design of inhibitors for human HDACs

4.2.1. 2-Aminobenzamide derivatives as class I HDAC inhibitors

The hydroxamic acid warhead is a potent zinc binder. Off-target effects are common with hydroxamic acid-based HDAC inhibitors [108, 109]. Additionally, many potent candidates were eliminated from further clinical tests due to cell mutagenicity and genotoxicity problems

[170]. Replacing the hydroxamic acid zinc binding group with other alternatives is a novel strategy for developing selective HDAC inhibitors.

In this part of the study, novel 2-aminobenzamide derivatives were designed, and their structure-activity relationships were analyzed by docking and molecular dynamics simulation studies. Then, we rescored the obtained docking poses by calculating their binding free energies to establish predictive models for a series of 2-aminobenzamide inhibitors.

4.2.1.1. Structural analysis of class I HDACs

Class I HDACs share similar pocket residues. Specifically, HDAC1-3 enzymes are structurally different from HDAC8 and share more than 90 % of their pocket similarities with each other. To understand the binding mode of 2-aminobenzamides, the X-ray structure of HDAC2 in a complex with a 2-aminobenzamide derivative (PDB ID: 4LY1 [55]) was compared with HDAC1 (PDB ID: 4BKX [25]) and HDAC3 (PDB ID: 4A69 [24]) (Figure 20). The analysis of HDAC1-3 structures revealed that HDAC1 and HDAC2 have the same pocket residues. Notably, HDAC3 shows some significant differences, which can be used to design selective inhibitors. The catalytic zinc ion is similarly accommodated at the bottom of the pocket. HDAC1-3 have a 14 Å internal cavity called the foot pocket [56], which is adjacent to the catalytic zinc ion. The size of the foot pocket differs between HDAC3 and HDAC1-2. The foot pocket of HDAC3 is narrower than HDAC1 and HDAC2. The bulky Y107 residue in HDAC3 is replaced by serine residues (S113 and S118 in HDAC1 and HDAC2, respectively). In HDAC3, Y107 pushes L133, resulting in a narrower foot pocket compared to HDAC1 and HDAC2. Due to this conformational difference of L133 (L139/144 in HDAC1/2, respectively), the bulky substituents on the 2-aminobenzamide scaffold cannot enter the foot pocket of HDAC3. Furthermore, HDAC1-3 has an 11 Å long acetyl lysine substrate channel (hydrophobic tunnel) that is made up of G149/154/143, F150/155/144, H178/183/172, F205/210/200, L271/276/266 in HDAC1, HDAC2, and HDAC3, respectively. The backbone of L271 and L276 interacts with Y204 and Y209 in HDAC1 and HDAC2, respectively. In HDAC3, F199 replaces Y209 in HDAC2.
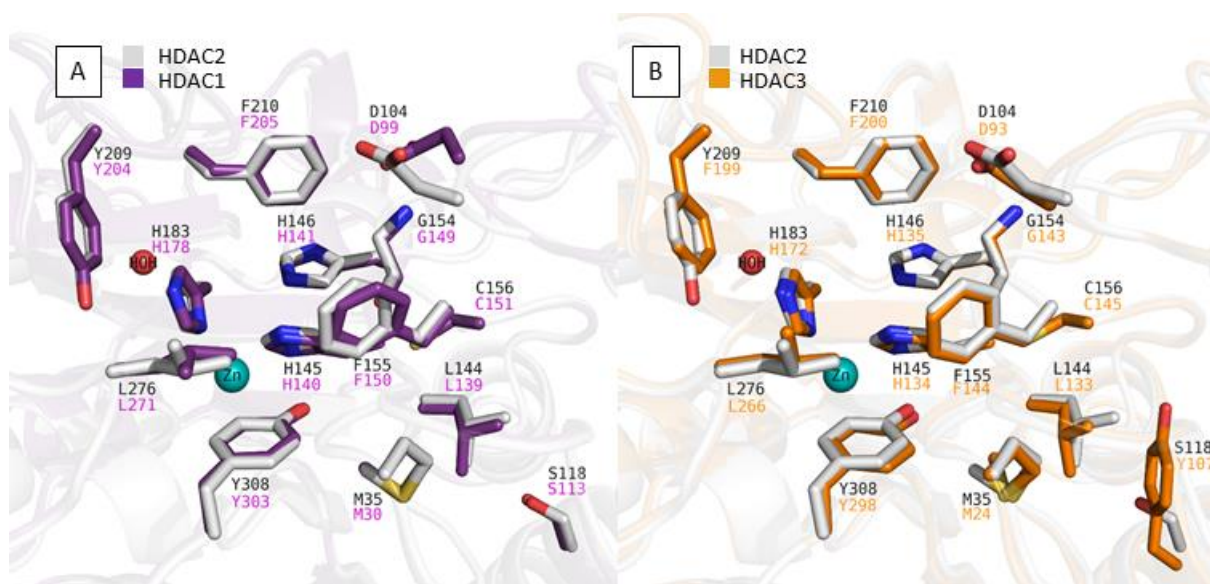
Figure 20. Comparison of HDAC1 – HDAC2 and HDAC3. A) Comparison of HDAC2 (PDB ID: 4LY1) (white coloured carbon and ribbons) and HDAC1 (PDB ID: 4BKX) (purple coloured carbon and ribbons) B) comparison of HDAC2 (PDB ID: 4LY1) (white coloured carbon and ribbons) and HDAC3 (PDB ID: 4A69) (orange coloured carbon and ribbons). Zinc ion were showed as cyan sphere, water as red sphere.

4.2.1.2. Redocking and cross-docking studies for 2-aminobenzamides

The X-ray structures of HDAC2 in a complex with 2-aminobenzamide derivatives (PDB ID: 3MAX [171], 4LY1 [55], 5IX0 [172], 5IWG [172]) were superposed and compared to understand the binding mode of the 2-aminobenzamides. The inhibitors occupy the hydrophobic tunnel and the foot pocket region. They bind in a bidentate manner to the zinc ion through their free amino group and carbonyl oxygen at the bottom of the hydrophobic tunnel. The free amino group shows hydrogen bond interactions with H145/146 and the catalytic Y308. The additional hydrogen bond interactions between the amide-NH of inhibitors and G154 were observed in all HDAC2 X-ray structures in a complex with 2-aminobenzamides. The aromatic linker groups are sandwiched between F155 and F210. In addition, the linker group of the inhibitors in HDAC2 X-ray structures (PDB ID 4LY1, 5IWG, and 5IX0) showed water-mediated H183 interaction.

After binding mode analysis of 2-aminobenzamides in HDAC2, re-docking (the ability to reproduce the binding mode of a co-crystallized ligand) and cross-docking (the ability to correctly predict the binding mode of the other crystallized ligands) studies were performed to

47

select a docking protocol which can correctly predict the binding modes of designed compounds. Although PDB ID 5IX0 and 5IWG showed high RMSD (root mean square deviation) values, their ligands lack a cap group. As a result, the structure PDB ID 4LY1 was chosen to dock the training set because it demonstrated the best re- and cross-docking results, i.e. the lowest RMSD values (Figure 21 and Table 9) and its ligand has a cap group.

Table 9. RMSD results (Å) of the cross-docking

Inhibitors	PDB ID			
	3MAX	4LY1	5IX0	5IWG
3MAX	0.20	0.27	0.15	0.29
4LY1	1.11	0.18	0.21	0.41
5IWG	0.66	0.69	0.55	0.64
5IX0	0.96	0.96	0.82	0.97
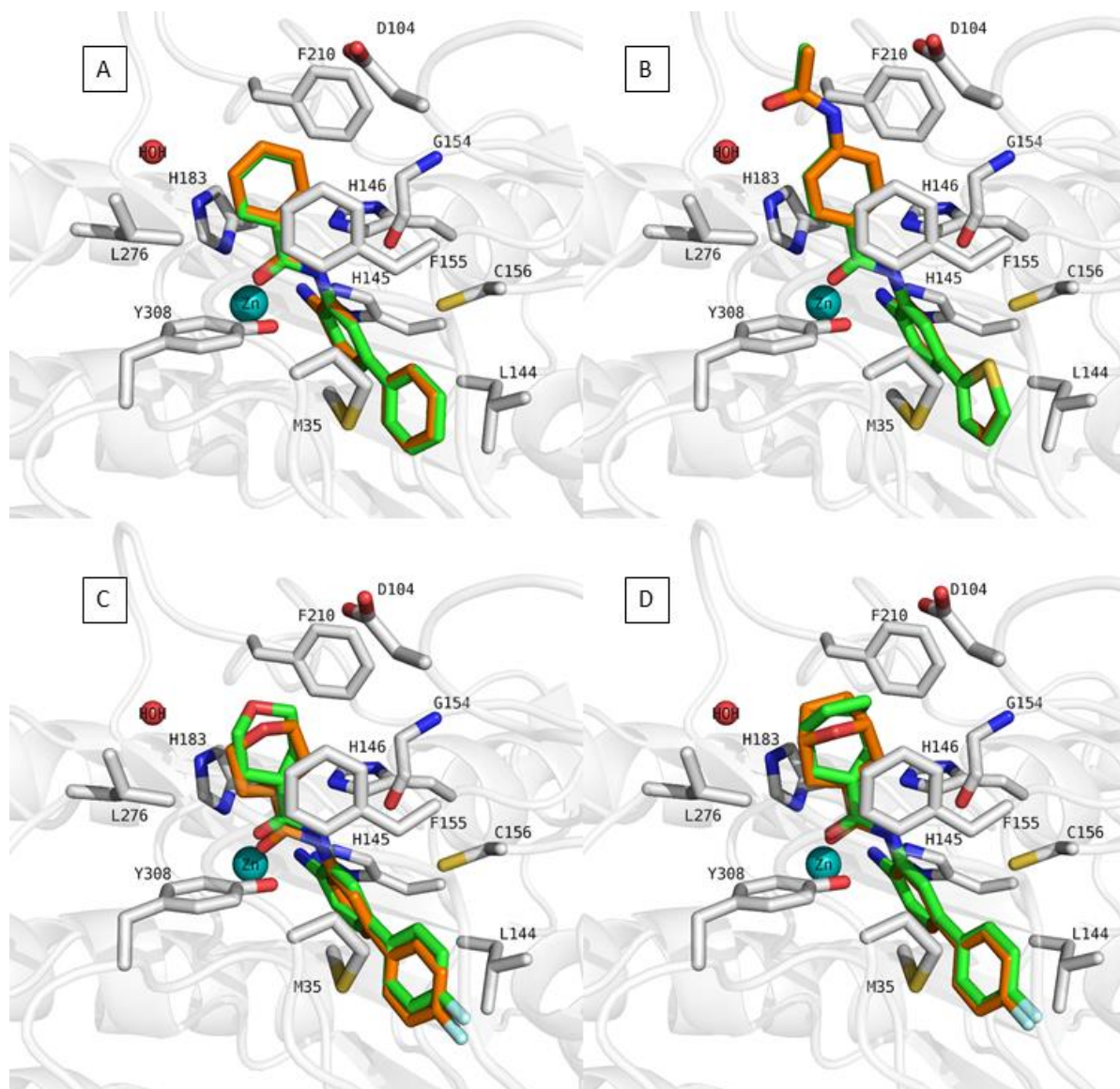
Since there is no crystal structure in a complex with a 2-aminobenzamide inhibitor for HDAC1 and HDAC3, the protein-ligand complexes of HDAC1 and HDAC3 were first prepared. The co-crystallized ligand of HDAC2 (PDB ID 4LY1) is reported as both an HDAC1 and an HDAC2 inhibitors [55]. Thus, the ligand from PDB ID 4LY1 was docked to HDAC1 (PDB ID: 4BKX). The HDAC1-ligand complex was prepared for further steps. This inhibitor showed no activity against HDAC3 [173]. Hence, the selective HDAC3 compound BG45 [173] was docked to HDAC3 (PDB ID: 4A69). The obtained HDAC3-ligand complex was utilized for further steps. Subsequently, a 100 ns molecular dynamics (MD) simulation was performed for the generated protein-ligand complexes of HDAC1, HDAC2 and HDAC3 to analyze the protein-ligand interactions and the stability of protein, ligand and zinc ion.

The MD analysis revealed that the active site residues of HDAC1 were highly stable during the 100 ns MD (Figure 22A). However, the catalytic Y303 was observed as flexible. In the RMSD analysis, the protein and zinc ion showed stability, while the ligand showed small fluctuations due to the flexible amide group (Figure 22B). The bidentate zinc coordination of the ligand was maintained during the 100 ns (Figure 22C). Additionally, the hydrogen bond analysis revealed that the ligand keeps the interactions with H140, H141, and G149 (Figure 22D). The Y303 interaction was not stable due to the flexibility of Y303. Furthermore, the $\pi - \pi$ interactions with F150 and F205 were maintained by the linker group accommodated in the hydrophobic tunnel (Figure 22E).
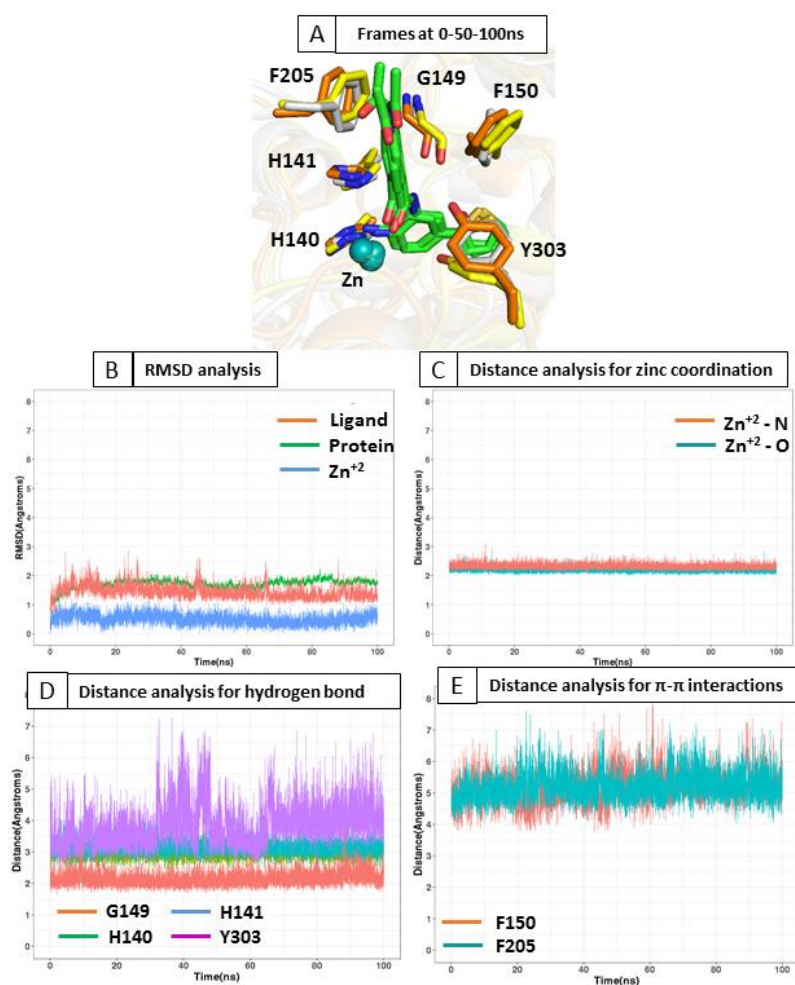
Figure 22. MD analysis results of HDAC1 (PDB ID: 4BKX) A) frames at 0,50, and 100 ns. The carbon atoms of the shown residues are coloured according to the time as following: white – 0ns, yellow – 50ns and orange – 100ns. Zinc ion is shown as cyan spheres. Ligands are shown in stick representation and their carbon atoms are coloured green. For clarity, only relevant residues were shown. B) RMSD analysis C) Distance analysis for zinc coordination D) Distance analysis for hydrogen bonds E) Distance analysis for π-π interactions.

As observed for the HDAC1-ligand complex, the active site residues of the HDAC2-ligand complex were highly stable except for Y308 (Figure 23A). The flexibility of Y308 was also observed in the other HDAC2 x-ray structure in a complex with 2-substituted benzamide (PDB ID: 7KBH [101]). The amide part of the ligand showed some small fluctuations, while the protein and zinc ion kept their positions (Figure 23B). The metal chelation between zinc and ligand was preserved (Figure 23C). Conserved hydrogen bond interactions with H145, H146, and G154 were maintained, while the interaction with Y308 was lost after 15 ns due to

the flexibility of Y308 (Figure 23D). Besides, the linker group is sandwiched between F155 and F210 throughout the MD simulation (Figure 23E).
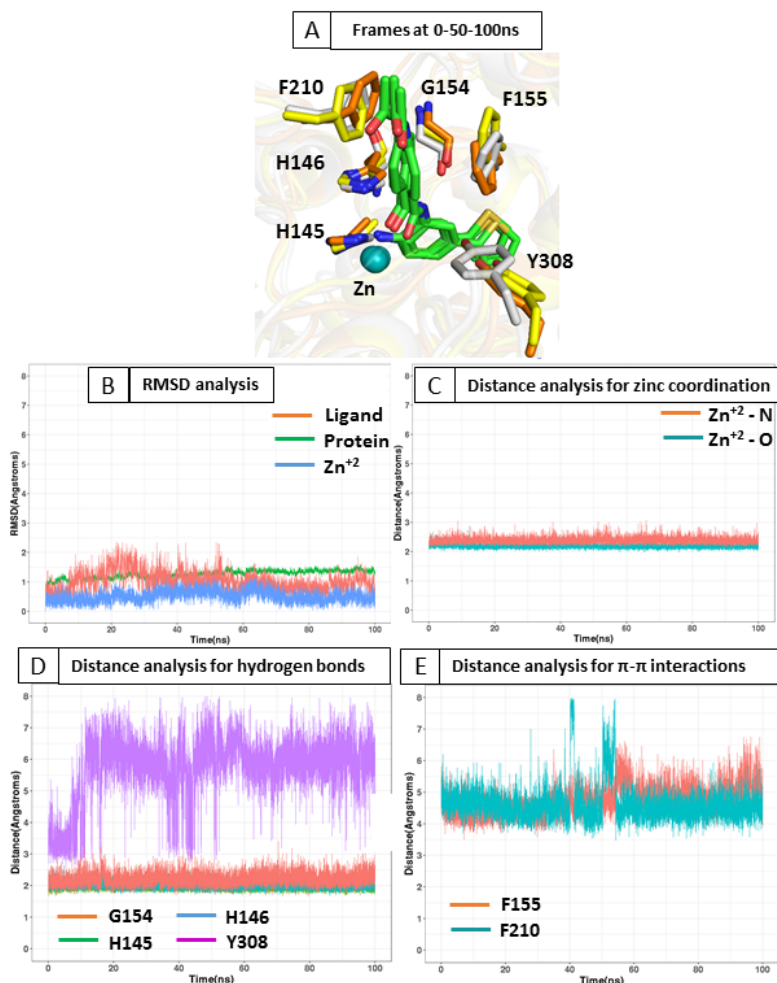
Figure 23. MD analysis results of HDAC2 (PDB ID: 4LY1) A) frames at 0-50 and 100 ns. The carbon atoms of the shown residues are coloured according to the time as following: white – 0ns, yellow – 50ns and orange – 100ns. Zinc ion is shown as cyan spheres. Ligands are shown in stick representation and their carbon atoms are coloured green. For clarity, only relevant residues were shown. B) RMSD analysis C) Distance analysis for zinc coordination D) Distance analysis for hydrogen bonds E) Distance analysis for π-π interactions.

Visual MD analysis of the HDAC3-ligand complex revealed that the active site residues of HDAC3 keep their positions except for F200 (Figure 24A). The RMSD analysis demonstrated that the protein, ligand, and zinc ion were highly stable and showed less than 2 Å deviation (Figure 24B). The distances for the zinc coordination between the ligand and zinc ion were maintained (Figure 24C). The hydrogen bonds with H145, H146, G154, and Y298 were maintained (Figure 24D). Furthermore, while π – π interactions with F144 were conserved, the

interactions between F200 and ligand were lost after 60 ns due to the side chain flexibility of F200 (Figure 24E).
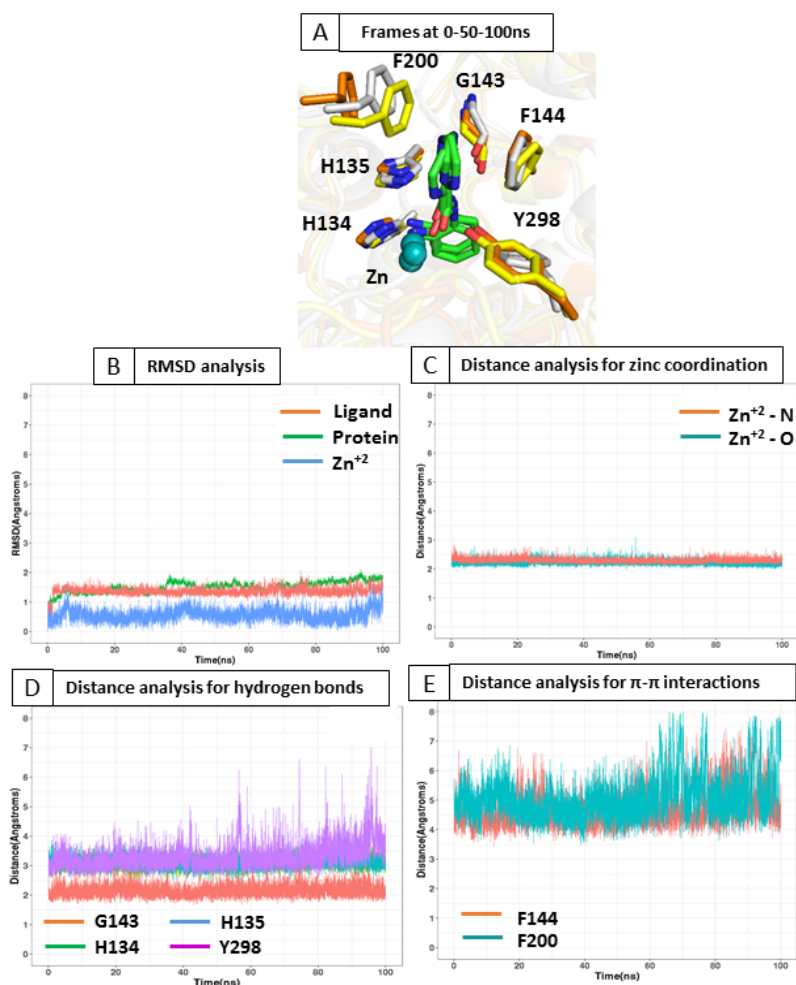
Figure 24. MD analysis results of HDAC3 (PDB ID: 4A69) A) frames at 0-50 and 100 ns. The carbon atoms of the shown residues are coloured according to the time as following: white – 0ns, yellow – 50ns and orange – 100ns. Zinc ion is shown as cyan spheres. Ligands are shown in stick representation and their carbon atoms are coloured green. For clarity, only relevant residues were shown. B) RMSD analysis C) Distance anaylsis for zinc coordination D) Distance analysis for hydrogen bonds E) Distance analysis for π-π interactions.

4.2.1.3. Design of novel 2-aminobenzamide derivatives

Analysis of the crystal structure of HDAC2 demonstrated that the 2-aminobenzamide part could fill the foot pocket next to the catalytic region. The isoform selectivity for HDAC1 and 2 was improved by the addition of an aromatic substituent to position-5 of the 2-aminobenzamide group. The entinostat chemotype was selected as a starting point to design novel compounds

due to its good class I HDAC selectivity. Entinostat was docked to the available crystal structures of HDAC1, 2, and 3 isoforms to acquire ideas for structural optimization (Figure 25).

In the designed compounds, the 2-aminobenzamide zinc binding group of entinostat was conserved to keep bidentate chelation with zinc ion. In the hydrophobic tunnel, the phenyl linker ring is accommodated between phenylalanines (F150/155/144 and F205/210/200 in HDAC1/2/3, respectively). This phenyl ring was substituted with polar pyrazine and pyrimidine rings to improve the solubility. The basic piperazine attached to a pyrimidine or pyrazine ring was postulated to imitate the amide moiety of entinostat, which shows interactions with conserved aspartate (D99/104/93 in HDAC1, 2 and 3, respectively). The cap group of entinostat is accommodated into the hydrophobic cavity consisting of H27/33/22 and P29/34/23 in HDAC1/2/3, respectively. Accordingly, various aromatic groups with different linker lengths were utilized to determine the impact of the cap groups on class I HDAC activity. Additionally, mono- or di-substitutions with different small groups at position 4 and/or position 5 of 2-aminobenzamides were tried to investigate the effect on isoform selectivity. The synthesized compounds structures are shown in Table 10.
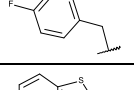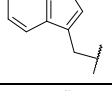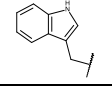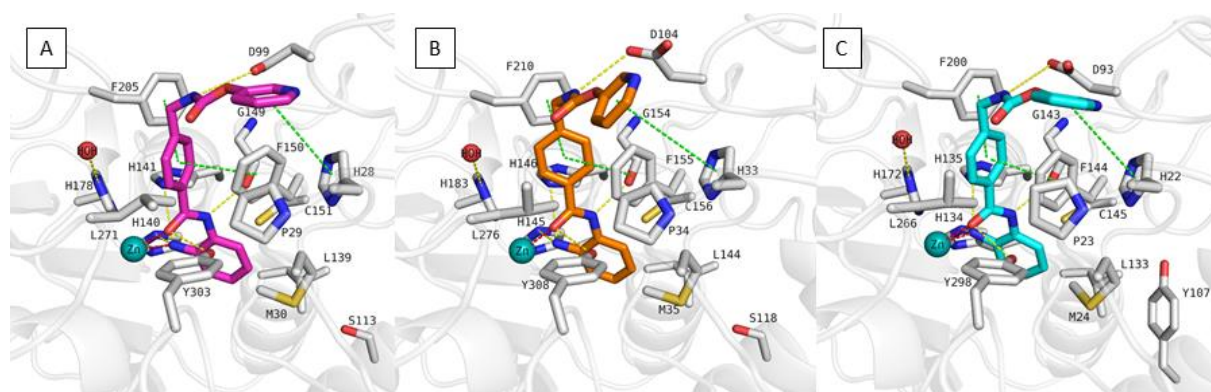

Figure 25. Docking poses of Entinostat (A, magenta coloured sticks) in HDAC1 (PDB ID: 4BKX), (B, orange coloured sticks) in HDAC2 (PDB ID: 4LY1), (C, cyan coloured sticks) in HDAC3 (PDB ID: 4A69). Hydrogen bonds (yellow dashed lines), metal coordination (red dashed lines), ionic interactions (blue dashed lines) and aromatic interactions (green dashed lines) between inhibitors and proteins are shown. Relevant residues are shown in stick representation as white carbon atoms in HDAC1/2/3. The zinc ion is shown as cyan coloured sphere. The conserved water molecule is shown as red sphere.

Table 10. İnhibitory activity of the synthesized compounds of the training set against HDAC1-3 [114].
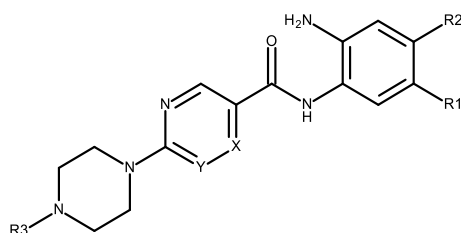
series	Cpd. No.	Substituents					IC$_{50}$ (μM) or % inhibition at given concentration		
		X	Y	R1	R2	R3	HDAC1	HDAC2	HDAC3
1	40	N	CH	H	H		0.51 ± 0.05	0.80 ± 0.07	1.12 ± 0.07
1	41	N	CH	H	H		26% @ 2 μM	30% @ 2 μM	65% @ 2 μM
1	42	CH	N	H	H		34% @ 2 μM	20% @ 2 μM	27% @ 2 μM
1	43	N	CH	H	H		0.52 ± 0.07	1.43 ± 0.08	1.06 ± 0.04
1	44	N	CH	H	H		0.21 ± 0.07	0.71 ± 0.04	0.84 ± 0.03
1	45	N	CH	H	H		0.13 ± 0.01	0.28 ± 0.01	0.31 ± 0.01
1	46	N	CH	H	H		0.31 ± 0.03	0.96 ± 0.05	0.49 ± 0.06
1	47	CH	N	H	H		0.45 ± 0.06	0.93 ± 0.04	1.75 ± 0.06
1	48	N	CH	H	H		0.14 ± 0.02	0.56 ± 0.04	0.59 ± 0.03
2	49	N	CH	2-Thienyl	H		0.26 ± 0.01	2.47 ± 0.22	0% @ 1 μM
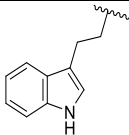
2	50	N	CH	4-F-C$_6$H$_4$	H	[indol-3-yl-propyl]	0.70 ± 0.08	0.77 ± 0.06	0% @ 1 µM
2	51	N	CH	2-F-C$_6$H$_4$	H	[indol-3-yl-propyl]	0.76 ± 0.07	0.76 ± 0.04	15 ± 1
2	52	N	CH	F	F	[indol-3-yl-propyl]	0.81 ± 0.07	0.74 ± 0.03	0.57 ± 0.02
2	53	N	CH	H	Cl	[indol-3-yl-propyl]	3.0 ± 0.2	2.7 ± 0.2	1.9 ± 0.1
2	54	N	CH	F	F	[1-methylindol-3-yl-ethyl]	0.29 ± 0.03	0.56 ± 0.02	0.81 ± 0.05
2	55	N	CH	H	F	[1-methylindol-3-yl-propyl]	0.40 ± 0.06	1.48 ± 0.19	0.40 ± 0.02
2	56	N	CH	F	H	[1-methylindol-3-yl-ethyl]	0.27 ± 0.03	0.50 ± 0.03	0.50 ± 0.02
2	57	N	CH	F	H	[1-methylindol-3-yl-propyl]	0.33 ± 0.02	1.37 ± 0.08	0.59 ± 0.04
3	58	CH	N	H	H	CH$_3$	5% @ 1 µM	7% @ 1 µM	13% @ 1 µM
3	59	N	CH	H	H	CH$_3$	27% @ 1 µM	15% @ 1 µM	30% @ 1 µM
4	60	N	CH	H	F	H	3.30 ± 0.18	2.17 ± 0.18	0.40 ± 0.01
4	61	N	CH	H	Cl	H	0% @ 1 µM	0% @ 1 µM	8.7 ± 0.4
4	62	N	CH	F	F	H	4.3 ± 0.3	4.2 ± 0.15	1.6 ± 0.1
4	63	N	CH	CF$_3$	H	H	0% @ 1 µM	0% @ 1 µM	0% @ 1 µM
4	64	N	CH	H	CH$_3$	H	0% @ 1 µM	0% @ 1 µM	0% @ 1 µM
4	65	N	CH	H	OCH$_3$	H	20.0 ± 1.0	14.0 ± 2.0	14.0 ± 1.0
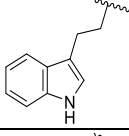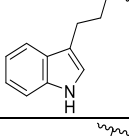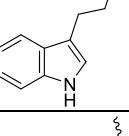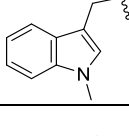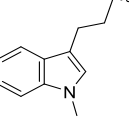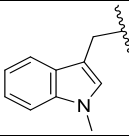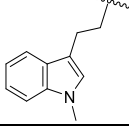
4	66	N	CH	3-Thienyl	H	CH$_3$	0.11 ± 0.01	0.18 ± 0.06	4.4 ± 0.1
4	67	N	CH	2-Thienyl	H	H	0.07 ± 0.01	0.26 ± 0.01	6.1 ± 0.7
4	68	N	CH	4-F-C$_6$H$_4$	H	H	0.16 ± 0.03	0.34 ± 0.01	6.7 ± 0.5
4	69	N	CH	2-F-C$_6$H$_4$	H	CH$_3$	0.18 ± 0.01	0.26 ± 0.07	12.0 ± 1.0
	CI994	--	--	--	--	--	37% @ 1 μM	36% @ 1 μM	32% @ 1 μM
	RGFP-966	--	--	--	--	--	16 ± 2	11 ± 1	1.3 ± 0.1
	MS-275	--	--	--	--	--	0.93 ± 0.1	0.95 ± 0.03	1.8 ± 0.1
	Mocetinostat	--	--	--	--	--	0.33 ± 0.04	0.34 ± 0.01	0.93 ± 0.05

n.d. not determined, -- no substituents

4.2.1.4. Structure – activity relationship and docking of synthesized compounds

The synthesized compounds can be classified into four groups depending on the substitution of the 2-aminobenzamide and the presence of the cap group. The first group of compounds (compounds 40-48) contain cap groups and unsubstituted 2-aminobenzamide scaffolds. The second group of compounds (compounds 49-57) comprises cap groups and substituted 2-aminobenzamide scaffolds. The third group of compounds (compounds 58-59) have unsubstituted 2-aminobenzamide and no cap groups. The last group of compounds (compounds 60-69) includes substituted 2-aminobenzamides and no cap groups. To understand the structure-activity relationship of the synthesized compounds, molecular docking studies were performed using the prepared crystal structures of HDAC1 (PDB ID: 4BKX), HDAC2 (PDB ID: 4LY1), and HDAC3 (PDB ID: 4A69).

In the first group of the designed compounds (40-48, Table 10) containing different capping groups and an unsubstituted 2-aminobenzamide moiety, the compounds exhibited HDAC1-3 inhibitory activity from low to submicromolar range. The different cap groups exhibit different effects on the HDAC inhibitory activity. For instance, the compounds 44, 45, and 48 having indole or benzothiophen ring as a cap group showed similar inhibitory profile for HDAC1, HDAC2 and HDAC3 (Table 10). Compound 45 (0.13 μM for HDAC1, 0.28 μM for HDAC2 and 0.31 μM for HDAC3) was found more potent than the reference compounds MS-275, CI994 and RGF-966. The other cap groups such as phenyl, 2-pyridyl demonstrated reduced inhibitory activity compared to compound 45 (Table 10). Additionally, the replacement of pyrazine linker group with pyrimidine ring caused in a decrease of inhibitory activity as observed for compounds 42, 47, 43, and 45. On the other hand, it was noticed that the replacement of methylene connecting group between indole group and piperazine with an ethylene connecting group resulted in a decrease of HDAC inhibitory activity as observed for compounds 45 and 46. In the first group of compounds, similar binding modes were observed in HDAC1-3, as exemplified by the docking pose of compound 45 in HDAC1/2/3 (Figure 26). The novel compounds chelate the zinc ion in a bidentate manner through their carbonyl oxygen and their free amino group. Moreover, the compounds interact with conserved H140/145/134, H141/146/135, G149/154/143, and Y303/308/298 in HDAC1, HDAC2, and HDAC3, respectively. The pyrazine group of compound 45 fills the hydrophobic tunnel consisting of G149/154/143, F150/155/144, H178/183/172, F205/210/200, and L271/276/266 in HDAC1, HDAC2, and HDAC3, respectively. The basic piperazine shows salt bridge interactions with aspartate D199/104/93 in HDAC1, 2, and 3, respectively. The aromatic cap group undergoes aromatic interactions with H28/33/22 in HDAC1/2 and 3, respectively.
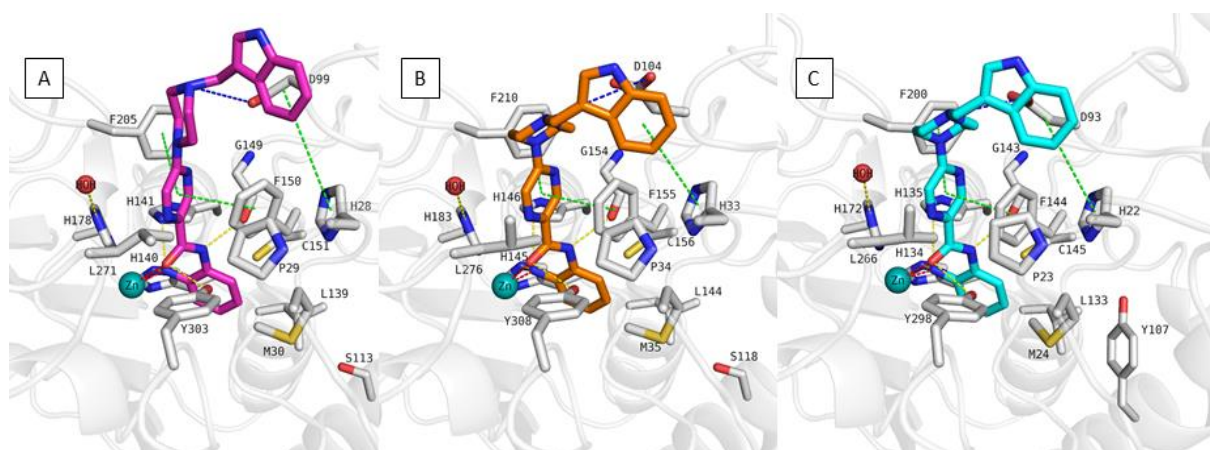
Figure 26. Docking poses of compound 45 (A, magenta coloured sticks) in HDAC1 (PDB ID: 4BKX), compound 45 (B, orange coloured sticks), in HDAC2 (PDB ID: 4LY1), compound 45 (C, cyan coloured sticks), in HDAC3 (PDB ID: 4A69). Hydrogen bonds (yellow dashed lines), metal coordination (red dashed lines), ionic interactions (blue dashed lines) and aromatic interactions (green dashed lines) between inhibitors and proteins are shown. Relevant residues are shown in stick representation as white carbon atoms in HDAC1, HDAC2 and HDAC3. The zinc ion is shown as cyan coloured sphere. The conserved water molecule is shown as red sphere.

In the second group of compounds (49-57, Table 10) having different substituents at the 2-aminobenzamide scaffold in the presence of 3-indolyl or (*N*-methyl)-3-indolyl capping group, different binding modes were observed in the class I HDAC isoforms. Attachment of a 5-thienyl ring to the benzamide moiety results in selectivity for HDAC1/2 over HDAC3 as observed for compound 49 (0.26 µM for HDAC1, 2.47 µM for HDAC2, 0 % at 1 µM for HDAC3). Similarly, compounds 50 and 51 having 4-fluorophenyl and 2-fluorophenyl, respectively, showed selectivity for HDAC1/HDAC2 over HDAC3 compared to their unsubstituted compound 46. Docking results of compound 49 in HDAC1 and 2 (Figure 27A/B) revealed that the thienyl moiety attached to the benzamide fills the foot pocket of HDAC1/2, where it exhibits hydrophobic interactions with M30/35, L139/144, C151/156 in HDAC1/2, respectively. Compounds with bulky groups at 2-aminobenzamide were unable to enter the foot pocket of HDAC3, which is narrower than HDAC1/2 (Figure 27C).
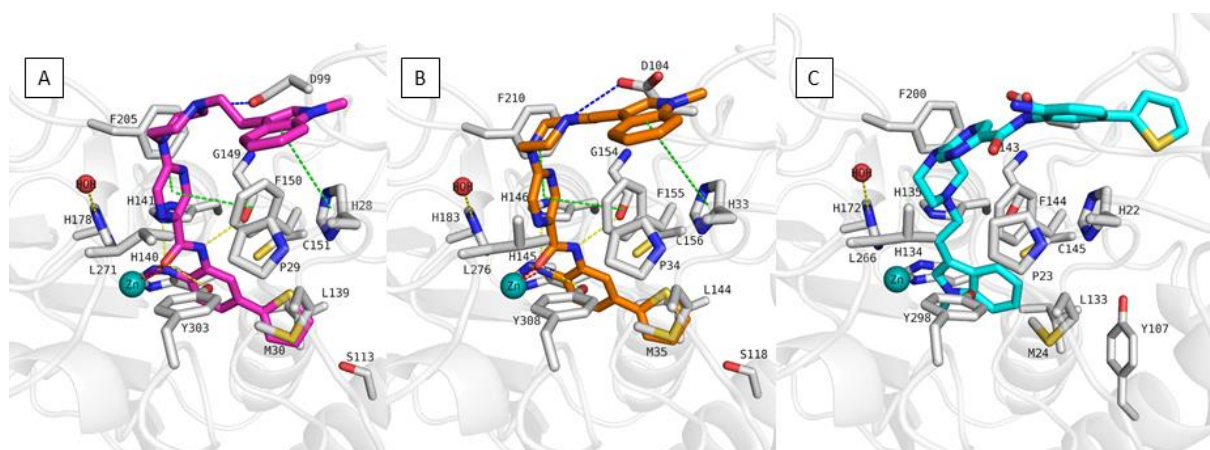
Figure 27. Docking poses of compound 49 (A, magenta coloured sticks) in HDAC1 (PDB ID: 4BKX), compound 49 (B, orange coloured sticks), in HDAC2 (PDB ID: 4LY1), compound 49 (C, cyan coloured sticks), in HDAC3 (PDB ID: 4A69). Hydrogen bonds (yellow dashed lines), metal coordination (red dashed lines), ionic interactions (blue dashed lines) and aromatic interactions (green dashed lines) between inhibitors and proteins are shown. Relevant residues are shown in stick representation as white carbon atoms in HDAC1, HDAC2 and HDAC3. The zinc ion is shown as cyan coloured sphere. The conserved water molecule is shown as red sphere.

The replacement of bulky groups by halogens (mono- or di-) did not improve the HDAC subtype selectivity as observed for compounds 52-57. Compound 53, which was chloro-substituted, had lower HDAC inhibitory activity than its unsubstituted derivative compound 46. Mono- or difluoro- substituted compounds 52, 54 and 55 performed similarly to their unsubstituted derivative compound 48. The docking results show a similar binding mode for the compounds 52-57 in class I HDAC isoforms, as exemplified by compound 54 in Figure 28. HDAC3 inhibitory activity was regained due to the accommodating of compounds into the active site of HDAC3.

Figure 28. Docking poses of compound 54 (A, magenta coloured sticks) in HDAC1 (PDB ID: 4BKX), compound 54 (B, orange coloured sticks), in HDAC2 (PDB ID: 4LY1), compound 54 (C, cyan coloured sticks), in HDAC3 (PDB ID: 4A69). Hydrogen bonds (yellow dashed lines), metal coordination (red dashed lines), ionic interactions (blue dashed lines) and aromatic interactions (green dashed lines) between inhibitors and proteins are shown. Relevant residues are shown in stick representation as white carbon atoms in HDAC1, HDAC2 and HDAC3. The zinc ion is shown as cyan coloured sphere. The conserved water molecule is shown as red sphere.

The third series of compounds (compounds 58-59, Table 10) possessing an unsubstituted 2-aminobenzamide and no cap groups exhibited weak HDAC1-3 inhibitory activity. These results lead us to try different substituents on the 2-aminobenzamide scaffold in the next series to understand the effect of the foot pocket group.

In the last series of compounds (60-69, Table 10) bearing different substitutions on the 2-aminobenzamide scaffold and no capping group, different binding poses were obtained in class I HDAC isoforms. Among the compounds 60-65 having small substituents instead of bulky aromatic groups, compound 60 having a fluoro substituent at position-4 showed selectivity for HDAC3 over HDAC1 and 2 (Figure 29). The fluoro substituent at position 4 is well tolerated in the foot pocket. In contrast, larger or bulkier groups like chloro (compound 61), trifluoromethyl (compound 63), methyl (compound 64) and methoxy (compound 65) dramatically reduced the inhibitory activity on HDAC1/2/3 isoforms. Docking poses of these compounds indicate that the larger or bulkier groups clash with G138/143/132 and G303/305/296 in HDAC1/2/3, respectively (not shown here).

Figure 29. Docking poses of compound 60 (A, magenta coloured sticks) in HDAC1 (PDB ID: 4BKX), compound 60 (B, orange coloured sticks), in HDAC2 (PDB ID: 4LY1), compound 60 (C, cyan coloured sticks), in HDAC3 (PDB ID: 4A69). Hydrogen bonds (yellow dashed lines), metal coordination (red dashed lines), ionic interactions (blue dashed lines) and aromatic interactions (green dashed lines) between inhibitors and proteins are shown. Relevant residues are shown in stick representation as white carbon atoms in HDAC1, HDAC2 and HDAC3. The zinc ion is shown as cyan coloured sphere. The conserved water molecule is shown as red sphere.

The compounds (compounds 66-69) having bulky groups like thienyl or fluorophenyl moieties at position-5 could not access the foot pocket of HDAC3 while exhibiting similar binding poses in HDAC1/2 as observed in the crystal structure of HDAC2 (PDB ID: 4LY1). These results indicate that compounds containing bulky groups on ZBG exhibit selectivity for HDAC1/2 over HDAC3, as exemplified by the docking pose of compound 67 in Figure 30.

Figure 30. Docking poses of compound 67 (A, magenta coloured sticks) in HDAC1 (PDB ID: 4BKX), compound 67 (B, orange coloured sticks), in HDAC2 (PDB ID: 4LY1), compound 67 (C, cyan coloured sticks), in HDAC3 (PDB ID: 4A69). Hydrogen bonds (yellow dashed lines), metal coordination (red dashed lines), ionic interactions (blue dashed lines) and aromatic interactions (green dashed lines) between inhibitors and proteins are shown. Relevant residues are shown in stick

61

To summarize the docking results, four series of compounds (30 compounds) have been designed, synthesized, and their binding modes have been analyzed. The compounds in the first series containing different cap groups and unsubstituted 2-aminobenzamide scaffold showed various HDAC1-3 activity depending on cap groups. The second series of compounds having different substituents at the 2-aminobenzamide scaffold in the presence of 3-indolyl or (*N*-methyl)-3-indolyl capping group resulted in different binding modes in the class I HDAC isoforms. The attachment of bulky substituent such as 2-thienyl or phenyl rings to the 5th position of 2-aminobenzamide scaffold caused HDAC1/2 selectivity over HDAC3. The fluoro substituent at the 4th position showed favorable effect on HDAC1-3 enzymes, but chloro had decreased the HDAC1-3 activity. The third series of compounds possessing unsubstituted 2-aminobenzamide and no cap groups showed weak HDAC1-3 inhibitory activity. The last series of compounds bearing different substitutions on ZBG and no capping group demonstrated different binding modes. The bulky substituents resulted in selectivity for HDAC1/2 over HDAC3. The fluoro substituent at 4th position showed HDAC3 selectivity over HDAC1/2. Replacement of the fluoro with chloro, CF$_3$, CH$_3$ and OCH$_3$ substituents caused in losing the HDAC1-3 inhibitory activity.

4.2.1.5. Molecular dynamics (MD) simulation of synthesized compounds

The 100 ns molecular dynamics simulations were performed for the most promising compounds (45, 49, 60, 67) in HDAC1, 2 and 3 crystal structures to evaluate the stability of protein-ligand interactions and predicted binding modes.

The MD analysis of the capless compound 60 showed that the compound conserves its bidentate zinc chelation in HDAC1, 2 and 3 during the 100 ns MD simulation (Figure 31). Protein, ligand, and zinc ion remained stable in all cases. Furthermore, in the zinc binding region, the fundamental hydrogen bond interactions with H140/145/134, H141/146/135, Y303/308/298, and G149/154/143 were preserved, as well as the π – π interactions with F150/155/144 and F205/210/200 in HDAC 1, 2 and 3 respectively.
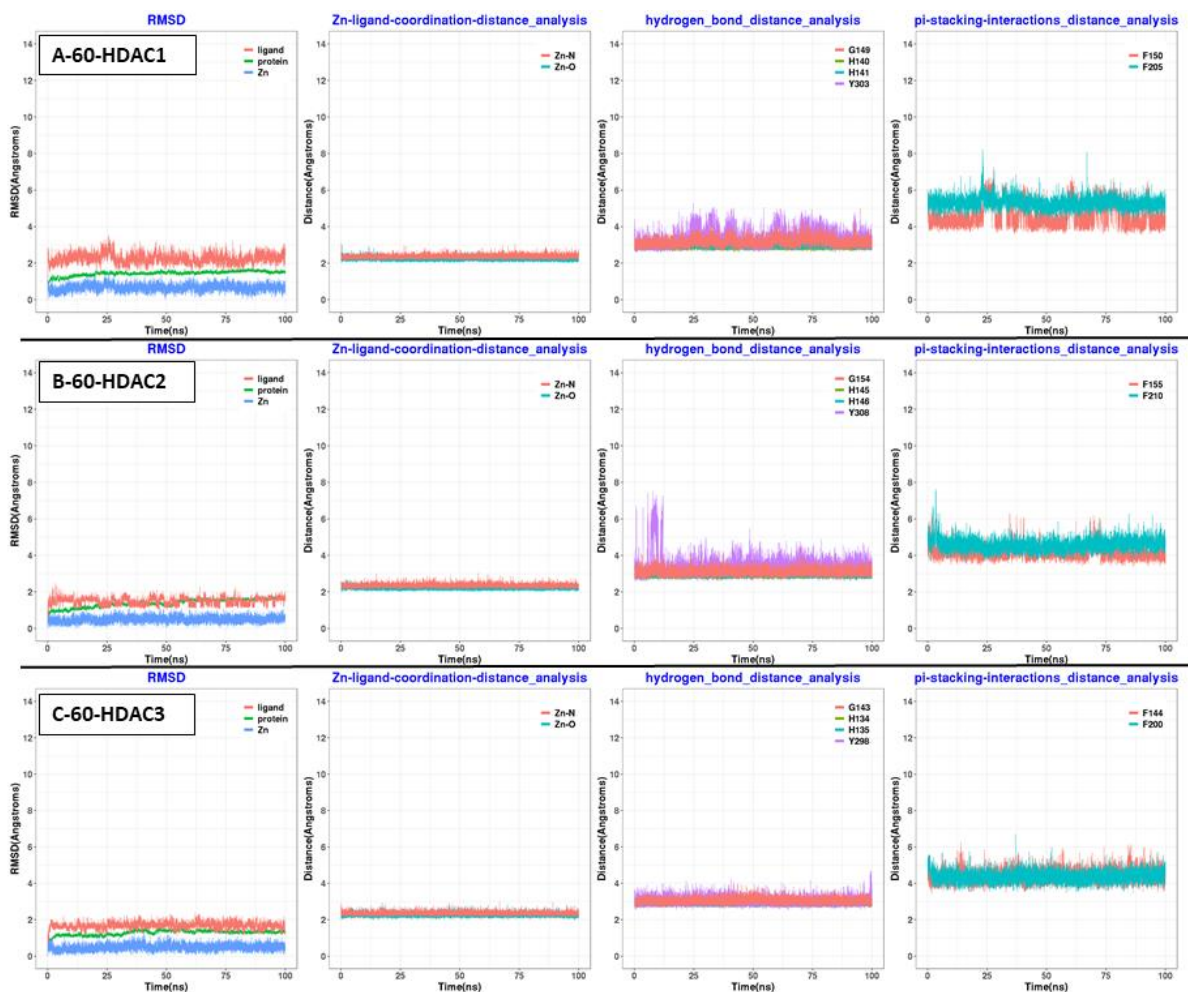
Figure 31. Analysis of 100 ns MD simulation for compound 60 in HDAC1, 2 and 3. A) in HDAC1(PDB ID: 4BKX), B) in HDAC2 (PDB ID: 4LY1) C) in HDAC3 (PDBID: 4A69). RMSD, Zn-ligand coordination distance analysis, hydrogen bond distance analysis and pi-stacking interactions distance analysis were shown.

In the case of the capless compound 67, the 2-aminobenzamide warhead keeps bidentate chelation during the 100 ns MD simulation (Figure 32). The protein, ligand, and zinc ion keep their position. The side chains of Y303 in HDAC1 and Y308 in HDAC2 were to be flexible. The other key hydrogen bond interactions with H140/145, H141/146, and G149/154 were conserved. In HDAC1, the side chain of F200 breaks its stability, while F150 stays stable. In HDAC2, compound 67 keeps its sandwiched position between F155 and F210.
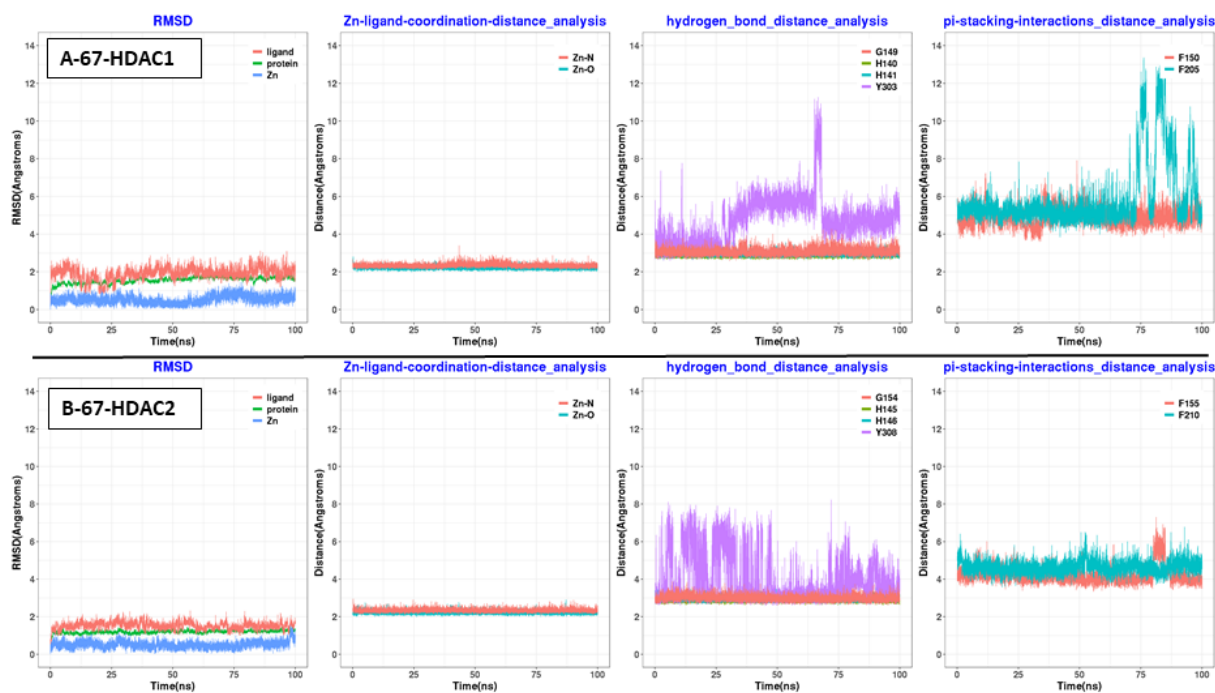
Figure 32. Analysis of 100 ns MD simulation for compound 67 in HDAC1 and 2. A) in HDAC1(PDB ID: 4BKX), B) in HDAC2 (PDB ID: 4LY1). RMSD, Zn-ligand coordination distance analysis, hydrogen bond distance analysis and pi-stacking interactions distance analysis were shown.

In the case of compound 45 (Figure 33), the protein and zinc ion were found stable during 100 ns MD simulation in all cases. The ligand showed some conformational changes and fluctuations in RMSD analysis of HDAC1, 2 and 3. However, the distance analysis in HDAC1, 2 and 3 indicated that the zinc binding and linker groups maintain their positions. The bidentate chelation with the zinc ion was kept in all cases. The hydrogen bonds in the zinc binding region were conserved. In HDAC3, the side chain of catalytic Y298 showed some conformational changes. The distance between Y298 and the carbonyl oxygen of the ligand could not be kept due to the flexibility of Y298 in HDAC3, while Y303 in HDAC1 and Y308 in HDAC2 maintained their position. In all cases, the linker group is accommodated in the hydrophobic tunnel by making π - π interactions with phenylalanines (F150/155/144 and F205/210/200 in HDAC1, 2 and 3, respectively). Notably, the solvent-exposed cap group of compound 45 caused strong fluctuations in the RMSD analysis due to its flexibility. It turned around on the surface and interacted with F205/210/200 in HDAC1, 2 and 3, respectively. The cap group adopts several favorable conformations at the surface of the protein.

64
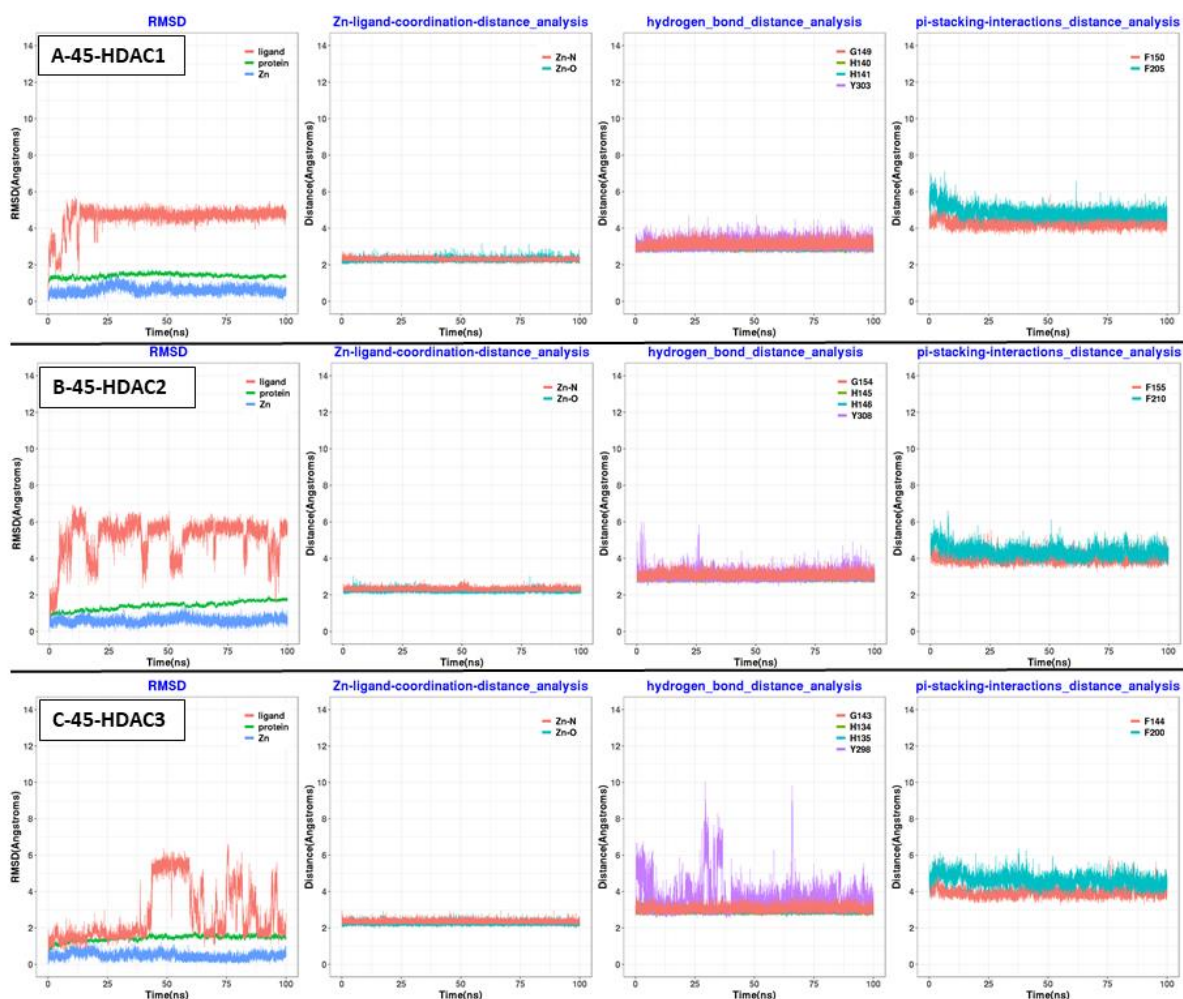
Figure 33. Analysis of 100 ns MD simulation for compound 45 in HDAC1, 2 and 3. A) in HDAC1(PDB ID: 4BKX), B) in HDAC2 (PDB ID: 4LY1) C) in HDAC3 (PDBID: 4A69). RMSD, Zn-ligand coordination distance analysis, hydrogen bond distance analysis and pi-stacking interactions distance analysis were shown.

Similar to compound 45, RMSD analysis of compound 49 indicated that protein and zinc conserve their stability while the ligand shows strong fluctuations (Figure 34). The zinc coordination between compound 49 and zinc ion was found to be stable. In the hydrogen bond analysis of the zinc binding group, it was noticed that the side chain of Y303 changed its position in HDAC1. Other fundamental hydrogen bond interactions were maintained in HDAC1. In HDAC2, the side chain of Y308 showed some fluctuations. Similarly, other interactions were found to be stable. In addition, the linker group also conserved its interactions with phenylalanine residues (F150/155 and F205/210 in HDAC1, and 2 respectively). As observed in the case of compound 45, the solvent-exposed cap group showed various favorable

conformations at the surface of HDAC1 and HDAC2. Similar to compound 45, compound 49 also showed interactions with F205/210 in HDAC1 and 2, respectively.
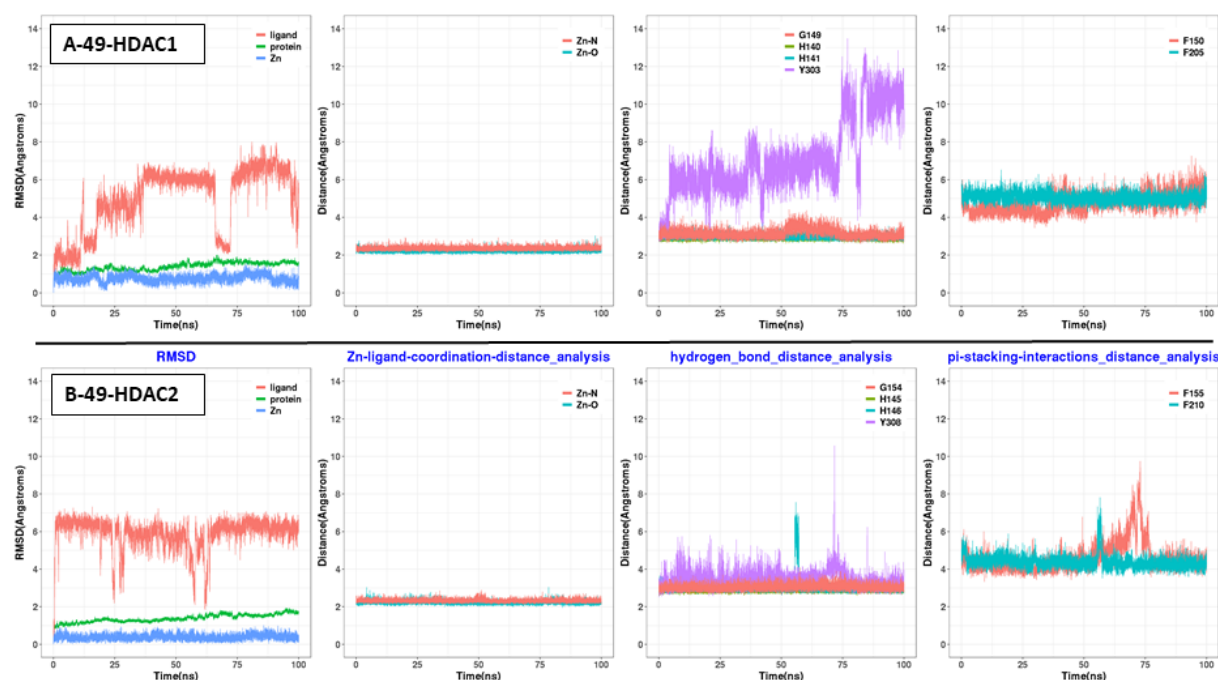
Figure 34. Analysis of 100 ns MD simulation for compound 49 in HDAC1 and 2. A) in HDAC1(PDB ID: 4BKX), B) in HDAC2 (PDB ID: 4LY1). RMSD, Zn-ligand coordination distance analysis, hydrogen bond distance analysis and pi-stacking interactions distance analysis were shown.

Molecular dynamics simulations of these promising compounds (45, 49, 60, 67) demonstrated that the cap groups (if they exist) adopt different favorable conformations on the surface. Furthermore, it is noticed that the linker group, zinc binding group, and foot pocket group (if exists) keep their position. However, Y303, Y308 and Y298 in HDAC1, 2, and 3, respectively, are found to be flexible. According to the MD simulations, tyrosine residues (Y303, Y308 and Y298 in HDAC1, 2, and 3, respectively) adopt different conformations. They might create a new pocket in the zinc binding region. This hypothesis should be tested by using different compounds having 2-aminobenzamide with o-substituents in the future.

4.2.1.6. Binding free energy (BFE) calculation of the synthesized compounds

The binding free energy calculations were done using six different parameter settings and six different frame settings (details in Section 3.4.). Accordingly, 108 models (36 models for

each protein) have been set up and analyzed by calculating the correlation coefficient (R^2) between experimentally obtained biological data and binding free energy values (Figure 35 and Table S1, Appendix). Only compounds whose IC_{50} values were determined were utilized to establish regression models (22 compounds for HDAC1, 23 compounds for HDAC2 and 22 compounds for HDAC3).
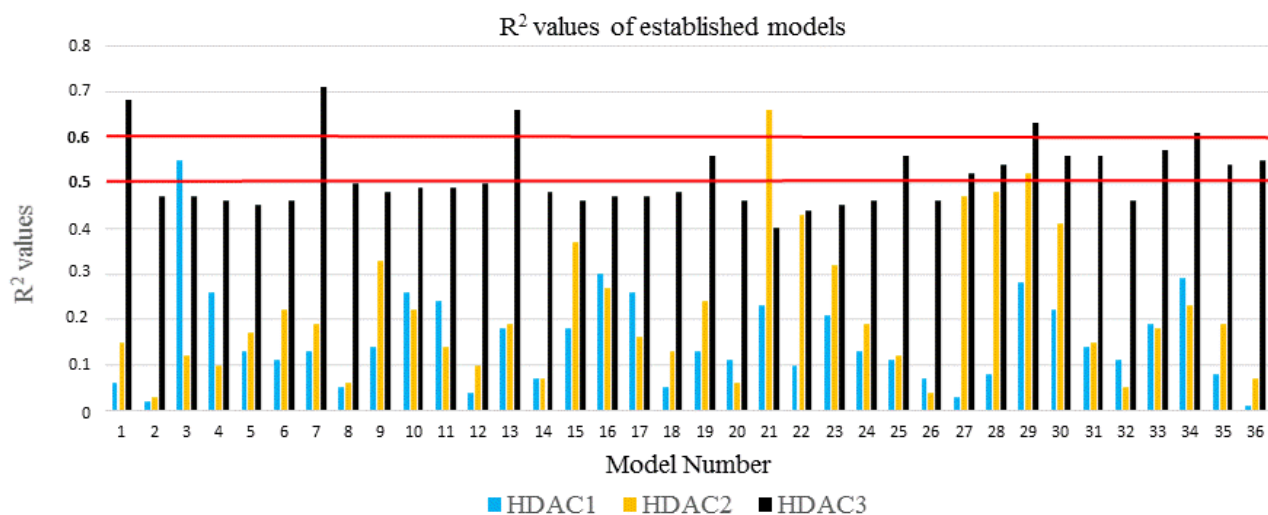
Figure 35. The R2 values of established predictive models for HDAC1 (blue bars), HDAC2 (orange bars) and HDAC3 (black bars). Red lines show the thresholds for model judgement.

The models were evaluated based on the calculated R^2 values. The models that have an R^2 value of less than 0.5 were not considered for model establishment. Only one model for HDAC1 crossed the 0.5 threshold. For HDAC2 and HDAC3, the threshold was determined as 0.6 due to many good correlations. One model for HDAC2 and four models for HDAC3 showed an R^2 value higher than 0.6. Then the cross-validation was performed by applying the leave-one-out method. The models were selected according to their R^2, RMSE (root mean square error), Q^2_{LOO} (leave one-out cross-validation), and QMSE (crossed-root mean square error) (Table 11).

Table 11. The selected best models of HDAC1, HDAC2 and HDAC3

Protein	N	Model Number	Method	Frame	R^2	RMSE	Q^2_{LOO}	QMSE
HDAC1	22	3	GB1	Md1-50	0.59	0.29	0.51	0.32
HDAC2	23	21	GB8	Md1-50	0.66	0.24	0.60	0.26
HDAC3	22	7	GB2	Emin1	0.71	0.29	0.65	0.32

According to the R^2 values (Figure 35 and Table S1, Appendix), model 3, which was established using the total calculated energy from the GB1 solvation model considering only frames 1-50 of the MD step, showed the best correlation coefficient and RMSE values in HDAC1 (R^2 of 0.59 and an RMSE of 0.29). The cross-validation values for model 3 in HDAC1 were determined as Q^2_{LOO} of 0.51 and QMSE of 0.32 (Table 11). The correlation plot of model 3 in HDAC1 is shown in Figure 36A. In addition to a good regression model of HDAC1, model 3 can discriminate between 19 compounds having less than 1 μM and 11 compounds having more than 1 μM (total 30 compounds) (Figure 36B). The threshold for the IC_{50} value was determined as 1 μM in HDAC1. The BFE values of all the compounds showing IC_{50} higher than 1 μM were found to be higher than -68.4 kcal/mol. Only one compound with a non-determined IC_{50} value (compound 42) was determined as an outlier. It has crossed the 1 μM threshold with a BFE value of -68.9 kcal/mol (Table S2, Appendix).

In the case of HDAC2, model 21, which was created from the GB8 solvation model considering different intervals (frames 1-50), outperformed the other models and showed an R^2 value of 0.66 and a RMSE of 0.24 (Figure 35 and Table 11). The cross-validation results were computed by applying the leave-one-out method (Q^2_{LOO} of 0.51 and QMSE of 0.32) (Table 11). The correlation plot of model 21 can be found in Figure 36A. Similar to HDAC1, model 21 in HDAC2 can be used as a classification model for all compounds (15 compounds having less than 1 μM and 15 compounds having more than 1 μM) (Figure 36B). The compounds whose calculated BFE values are less than -110.2 kcal/mol show an IC_{50} of less than 1 μM. Only two slightly less potent compounds 49 and 55 are found as outliers (Table S3, Appendix).

In the case of HDAC3, five models crossed the R^2 value of 0.6 (Figure 35). Among five models, model 7 was selected due to the good validation results (R^2 of 0.71, RMSE of 0.29, Q^2_{LOO} 0.65, and QMSE 0.32) (Table 11). Model 7 was established with the combination of the GB2 model and a single frame taken after the first minimization step (Emin1). The correlation plot of model 7 is shown in Figure 36A. This model can also discriminate all 30 compounds

68

according to their IC_{50} values (16 compounds having less than 2 μM and 14 compounds having more than 2 μM) (Figure 36B). Unfortunately, in the case of HDAC3, the 1 μM threshold for IC_{50} did not discriminate compounds. Hence, the threshold for IC_{50} was determined as 2 μM for HDAC3. Among the compounds having an IC_{50} of less than 2 μM showed less than -55.4 kcal/mol BFE values except compounds 53, 54, and 62. Among the compounds with non-determined IC_{50} values, only three compounds (41, 42, and 58) were observed as outliers (Table S4, Appendix).
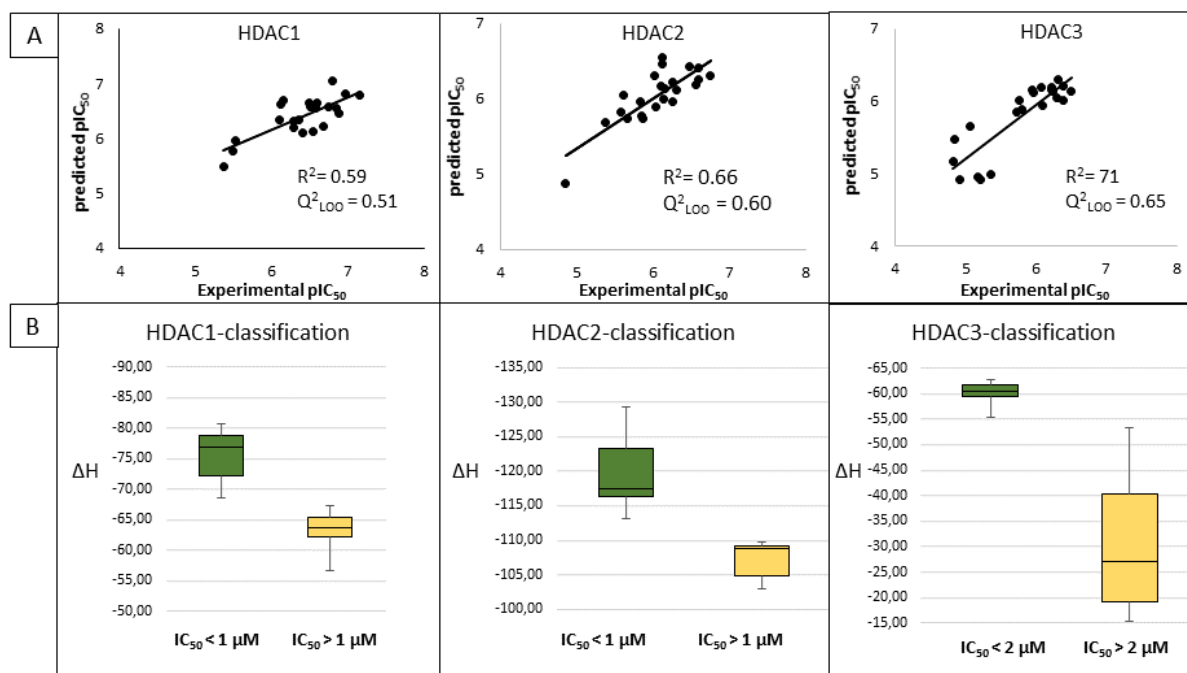
Figure 36. The correlation plots and box plots of the best BFE models. A) Correlation plots showing correlation between the predicted data and experimental data for each HDAC subtype (actives only). B) Box plots showing BFE distribution of 30 compounds (actives and inactives)

4.2.1.7. External validation of the QSAR model

To externally validate the established best three models for HDAC1-3, novel derivatives containing scaffold A or scaffold B were designed (Figure 37). Compounds 70, 71, 72, and 73 (Table 12) containing scaffold A were designed by optimizing compound 67 in the training set to improve the selectivity power for HDAC1 over HDAC2 and HDAC3. The piperazine is substituted by small methyl and acetyl groups to gain water-mediated interactions at the surface of the pocket. In addition, the hydrophobicity of the secondary amine of compound 67 was increased by the tertiary amine formation or conversion to an acetamido group.

On the other hand, the compounds having scaffold B (74, 75, 76, Figure 37B and Table 12) were designed by the combination of structural features of compound 60, entinostat and the co-crystallized ligand in HDAC2 (PDB ID: 4LY1) to evaluate the impact of an inverse amide. The fluoro substituent of compound 60 was kept in the new series to benefit from its favourable effect on HDAC3 selectivity. The hydrophobic cap group of entinostat was attached to the inverse amide.

The predictive accuracy and reliability of the established three models for HDAC1-3 were evaluated on the novel designed test set.
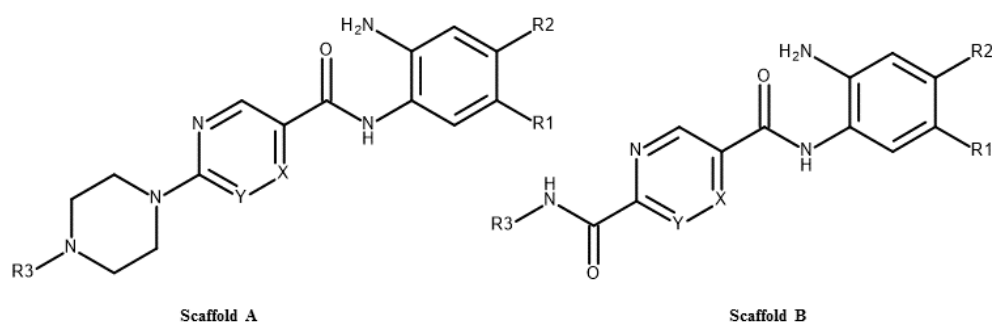
Figure 37. General structure of the test set molecules

Table 12. Structures of the novel inhibitors (test set) [154]

Cpd. No.	Substituents				
	X	Y	R1	R2	R3
70	CH	N	2-Thienyl	H	-CH3
71	N	CH	2-Thienyl	H	-CH3
72	N	CH	2-Thienyl	H	
73	N	CH	H	H	
74	CH	CH	H	F	
75	CH	CH	H	F	
76	CH	CH	H	F	

70

The same docking protocol, which was used for the training set, was applied for the docking of the test set into HDAC1-3. The previously observed binding modes for the reference compounds were obtained for the test set. Compounds 70, 71, and 72 could not access the foot pocket of HDAC3 due to the steric hindrance of L133, which is pushed by Y107 in HDAC3. The compounds of scaffold A are exemplified by the obtained docking pose of compound 72 in Figure 38. This compound binds in a bidentate fashion to the zinc ion and exhibits hydrogen bonds with H140/145/134, H141/146/135, Y303/308/298, and G149/154/143 in HDAC1, 2 and 3, respectively. The pyrazine moiety is located in a sandwiched position between F150/155/144 and F205/210/200 in HDAC1, 2 and 3, respectively. The attachment of the amido group to the piperazine has resulted in improved HDAC1 activity and gained selectivity for HDAC1 over HDAC2 and HDAC3.
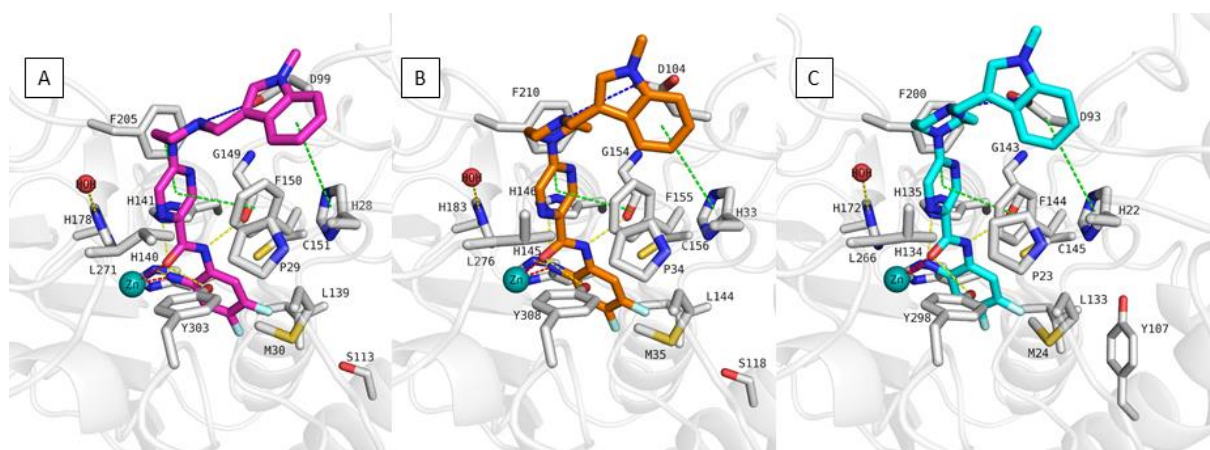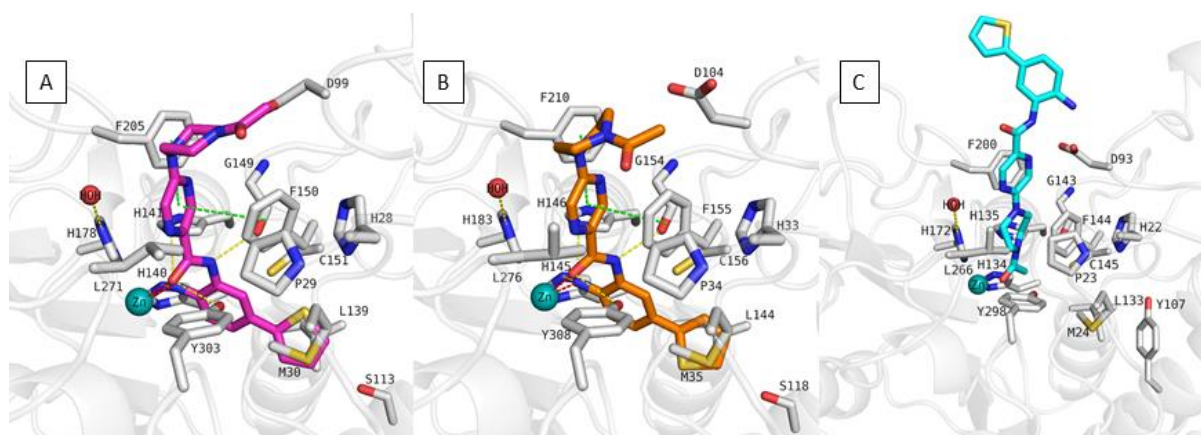

Figure 38. Docking poses of compound 72 (A, magenta coloured sticks) in HDAC1 (PDB ID: 4BKX), compound 72 (B, orange coloured sticks), in HDAC2 (PDB ID: 4LY1), compound 72 (C, cyan coloured sticks), in HDAC3 (PDB ID: 4A69). Hydrogen bonds (yellow dashed lines), metal coordination (red dashed lines), ionic interactions (blue dashed lines) and aromatic interactions (green dashed lines) between inhibitors and proteins are shown. Relevant residues are shown in stick representation as white carbon atoms in HDAC1, HDAC2 and HDAC3. The zinc ion is shown as cyan coloured sphere. The conserved water molecule is shown as red sphere

The compounds designed from scaffold B (74, 75, and 76, Table 12) are exemplified by the binding pose of compound 74 in Figure 39. The amide scaffold lost its interactions with D99/104/93 in HDAC1/2/3, respectively, as compared with the co-crystallized ligand of HDAC2 (PDB ID: 4LY1 and chain B) and entinostat. Notably, the loss of the interaction between the amide of ligands and conserved aspartate dramatically decreased the activity of HDAC1, 2 and 3. The aromatic cap group exhibited π - π interactions with F150/155/144 in HDAC1/2/3, respectively. Interestingly, the existence of both the cap group and the fluoro

group targeting the foot pocket could not tolerate the reduced activity caused by the removal of interactions with D99/104/93 in HDAC1/2/3, respectively.
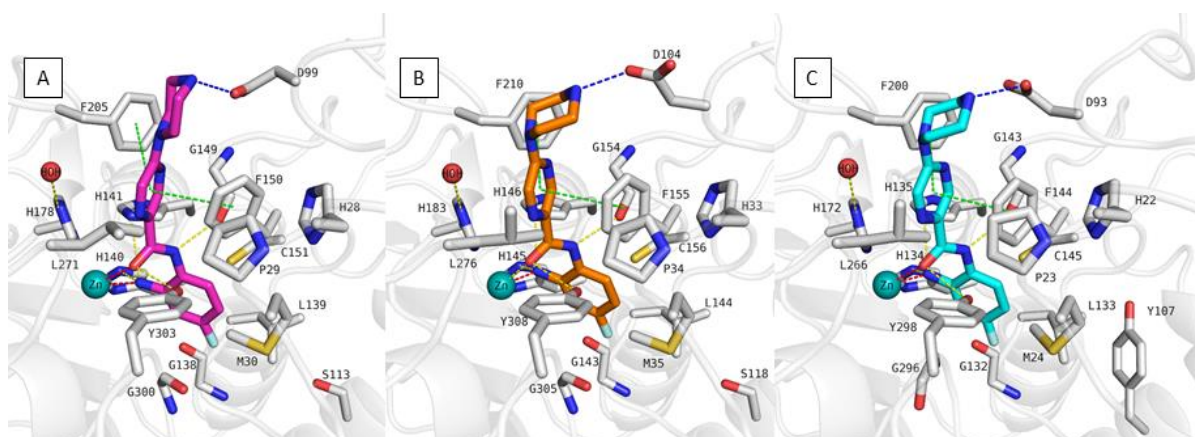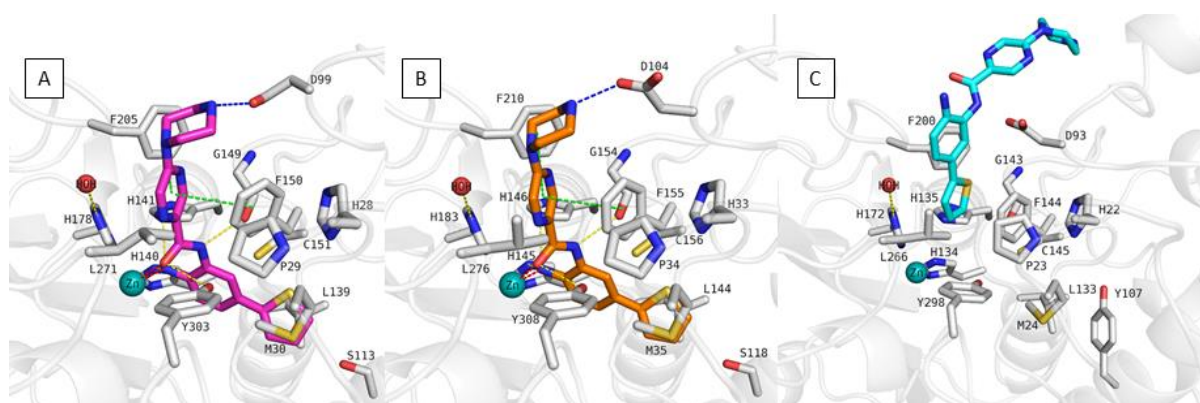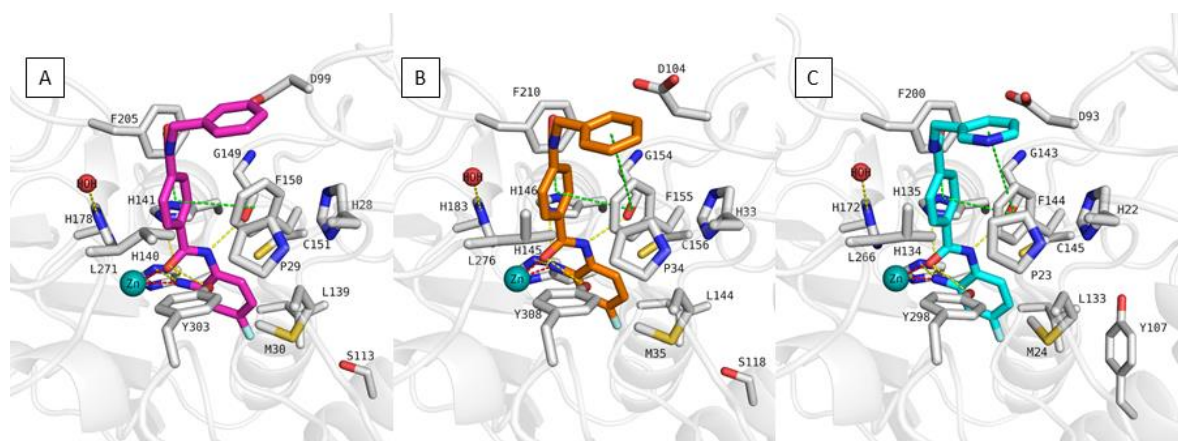

Figure 39. Docking poses of compound 74 (A, magenta coloured sticks) in HDAC1 (PDB ID: 4BKX), compound 74 (B, orange coloured sticks), in HDAC2 (PDB ID: 4LY1), compound 74 (C, cyan coloured sticks), in HDAC3 (PDB ID: 4A69). Hydrogen bonds (yellow dashed lines), metal coordination (red dashed lines), ionic interactions (blue dashed lines) and aromatic interactions (green dashed lines) between inhibitors and proteins are shown. Relevant residues are shown in stick representation as white carbon atoms in HDAC1, HDAC2 and HDAC3. The zinc ion is shown as cyan coloured sphere. The conserved water molecule is shown as red sphere

The selected docking poses were rescored by BFE calculations. The three best models of HDAC1-3 were used to predict the activities of the compounds (Table 13, Table S5-8, Appendix). According to the prediction results, the best three models of HDAC1-3 can classify the compounds as active or weakly active/inactive considering the cut off values determined for the training set. The compounds were predicted with a difference of less than 1.3 log units. Only the predicted activities of compounds 71 and 72 in HDAC1 and compound 73 in HDAC2 showed more than 1 log unit than the experimental pIC_{50} values. However, the classification of these compounds was correctly predicted based on the BFE results.

Table 13. Experimental and predicted activities (pIC_{50} or inhibition percent at a given concentration) of the test set compounds against HDAC1-3s

Cpd. No.	Scaffold	Experimental HDAC1 pIC_{50}	Predicted HDAC1 pIC_{50})	Difference experimental - predicted HDAC1 pIC_{50}	Experimental HDAC2 pIC_{50}	Predicted HDAC2 pIC_{50}	Difference experimental -predicted HDAC2 pIC_{50}	Experimental HDAC3 pIC_{50}	Predicted HDAC3 pIC_{50}

70	A	6.49	6.55	0.06	6.21	6.00	0.21	8% @1 μM 38% @10 μM	5.06
71	A	7.40	6.31	1.09	6.10	6.24	0.14	6% @1 μM 35% @10 μM	5.01
72	A	7.72	6.50	1.22	5.96	5.95	0.01	4% @1 μM 30% @10 μM	4.98
73	A	5.72	5.70	0.02	4.62	5.89	1.27	15% @1 μM 72% @10 μM	5.98
74	B	4% @1 μM 31% @10 μM	5.58		10% @1 μM 37% @10 μM	5.52		21% @1 μM 65% @10 μM	5.81
75	B	0% @1 μM 27% @10 μM	5.77		13% @1 μM 30% @10 μM	5.29		19% @1 μM 59% @10 μM	5.80
76	B	6% @1 μM 36% @10 μM	5.68		14% @1 μM 51% @10 μM	5.52		25% @1 μM 66% @10 μM	5.79

4.2.2. Alkylhydrazide derivatives as novel classs I HDAC inhibitors

Although class I HDAC selectivity is achieved by targeting the foot pocket of class I HDACs, the selectivity between members of class I HDACs, especially HDAC1-3, is still a crucial challenge which should be overcome. The zinc binding group exists in most HDAC inhibitors and might affect selectivity. Till now, hydroxamic acid, 2-aminobenzamide, 2-substitutebenzamide, alkylketone and arylketone warheads have been used to design class I HDAC inhibitors [55, 100-102, 106, 114, 118, 171, 172]. Recently, hydrazide scaffolds attracted attention by showing dramatic improvements in potency and selectivity for HDAC1-3 and 8 [110-113, 115, 174, 175].

In the current part of the work, we performed molecular docking and molecular dynamics simulations to detect the structural explanation for acquiring either high HDAC3 or HDAC8 potency as well as selectivity over other HDACs.

4.2.2.1. Preparation of class I human HDACs (HDAC1-2-3 and 8) and class IIb (HDAC6)

Since no X-ray structure of HDACs was resolved in a complex with a hydrazide warhead, the crystal structures in a complex with a hydroxamic acid warhead were selected for docking studies. The hydroxamic acid scaffold and hydrazide scaffold are structurally similar groups. Therefore, x-ray crystal structures of HDAC1 (PDB ID: 4BKX [25]), HDAC2 (PDB ID: 4LXZ [55]), HDAC3 (PDB ID: 4A69 [24]), HDAC6 (PDB ID: 5EDU [99]) and HDAC8 (PDB ID: 1T69 [103]) were retrieved from the protein data bank (PDB, rcsb.org [53]) and analyzed in MOE [129] .

The comparison of the class I HDACs (HDAC1-3 and 8) and HDAC6 crystal structures revealed some similarities and crucial structural differences (Figure 40). The catalytic binding pocket consisted of three parts in each isoform: the acetate binding cavity (zinc binding region), the substrate binding tunnel (hydrophobic tunnel) and the rim of the pocket. At the bottom of the catalytic pocket, a zinc ion is present. Additionally, the catalytic tyrosines (Y298/782/306 in HDAC3/6/8, respectively) and two histidines (H134/610/142 and H135/611/143 in HDAC3/6/8, respectively) in the zinc binding region show potential hydrogen bond donor and acceptor features. In addition to the similarities, some crucial pharmacophoric differences were observed. First, class I HDACs have an additional 14 Å internal cavity called the foot pocket, as mentioned in section 4.2.1.1. This foot pocket does not exist in HDAC6. P608 (replaced by L133 in HDAC3) closes the foot pocket region of HDAC6, which the alkyl side chain attached to the hydrazide cannot access. This explains why the compounds aimed at the foot pocket of HDAC1-3 are not active on HDAC6. Another crucial structural difference was observed in the foot pocket region of class I HDACs (HDAC1-3 and 8). The difference observed between HDAC1-3 was mentioned in section 4.2.1.1. In addition, the foot pocket shape of HDAC8 is both structurally and volumetrically different from other class I HDACs. The leucine residue in HDAC1-3 (L139/144/133 in HDAC1/2/3, respectively) was replaced by a bulky tryptophan (W141) in HDAC8. Besides, replacing M24 in HDAC3 with I34 enlarges the HDAC8 foot pocket size (Figure 40). In addition to the foot pocket differences between HDAC8 and other class I HDACs, it is observed that HDAC8 has an additional side pocket which is not present

in HDAC1-3. This side pocket consisted of M274 (replaced by L266 in HDAC3), F152, and Y306 residues.
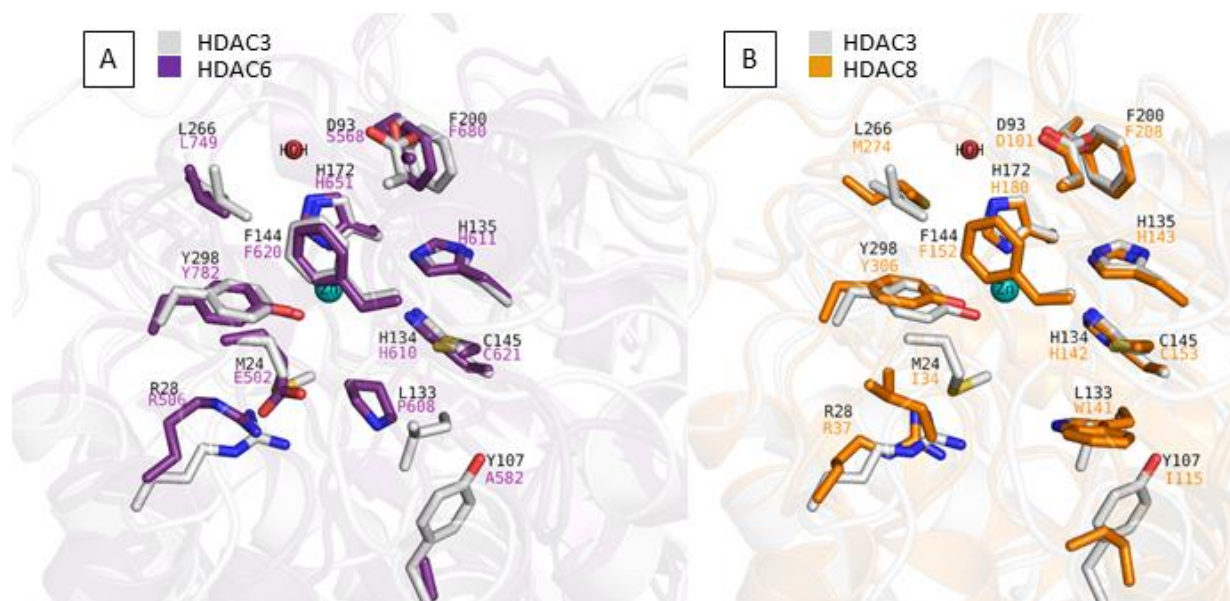
Figure 40. Comparison of HDAC3 - HDAC6 – HDAC8. A) Comparison of HDAC3 (PDB ID: 4A69) (white coloured carbon and ribbons) and HDAC6 (PDB ID: 5EDU) (purple coloured carbon and ribbons) B) comparison of HDAC3 (PDB ID: 4A69) (white coloured carbon and ribbons) and HDAC8 (PDB ID: 1T69) (orange coloured carbon and ribbons). Zinc ion is shown as cyan sphere, water as red sphere.

After careful analysis of protein structures, the crystal structures of HDAC2 (PDB ID: 4LXZ), HDAC6 (PDB ID 5EDU), and HDAC8 (PDB ID: 1T69) were validated by redocking studies to find an appropriate docking protocol (Figure 41). The redocking results of co-crystallized inhibitors in HDAC2, HDAC6 and HDAC8 showed an RMSD of 0.73 Å, 0.45 Å, and 1.22 Å, respectively. In all cases, the hydroxamic acid warheads of the re-docked poses are overlapped with the hydroxamic acid part of the corresponding co-crystallized ligands. SAHA with a hydroxamic acid scaffold in a complex with HDAC2 protein (PDB ID: 4LXZ) was identified as a pan-HDAC inhibitor with activity against HDAC1 and HDAC3 [55]. First, the HDAC2 crystal structure (PDB ID: 4LXZ) was superposed with HDAC1 (PDB ID: 4BKX) and HDAC3 (PDB ID: 4A69) in MOE [129]. Due to the high similarity between HDAC2 and HDAC1/3, SAHA was minimized with HDAC1 and HDAC3 to mimic the induced fit effect of the zinc binding group (Figure 42).
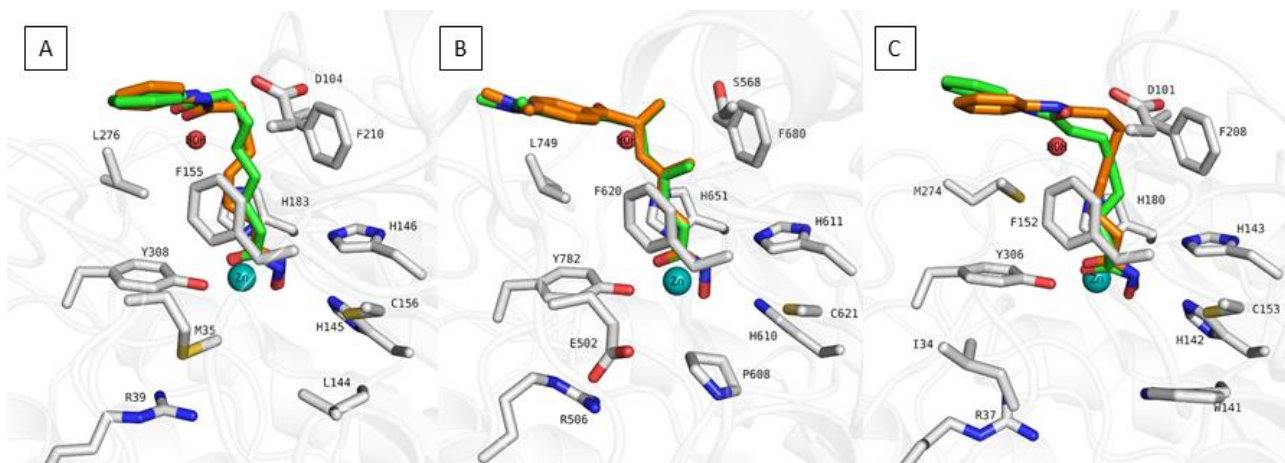
Figure 41. Redocking poses of co-crystallized ligands of HDAC2 – HDAC6 – HDAC8. A) in HDAC2 (PDB ID: 4LXZ), B) in HDAC1 (PDB ID: 4BKX) and C) in HDAC8 (PDB ID:1T69). Ribbons were shown as white colour. Residues were shown with white carbon colour. Redocked poses were shown as green carbon colour and co-crystallized ligands as orange carbon colour.
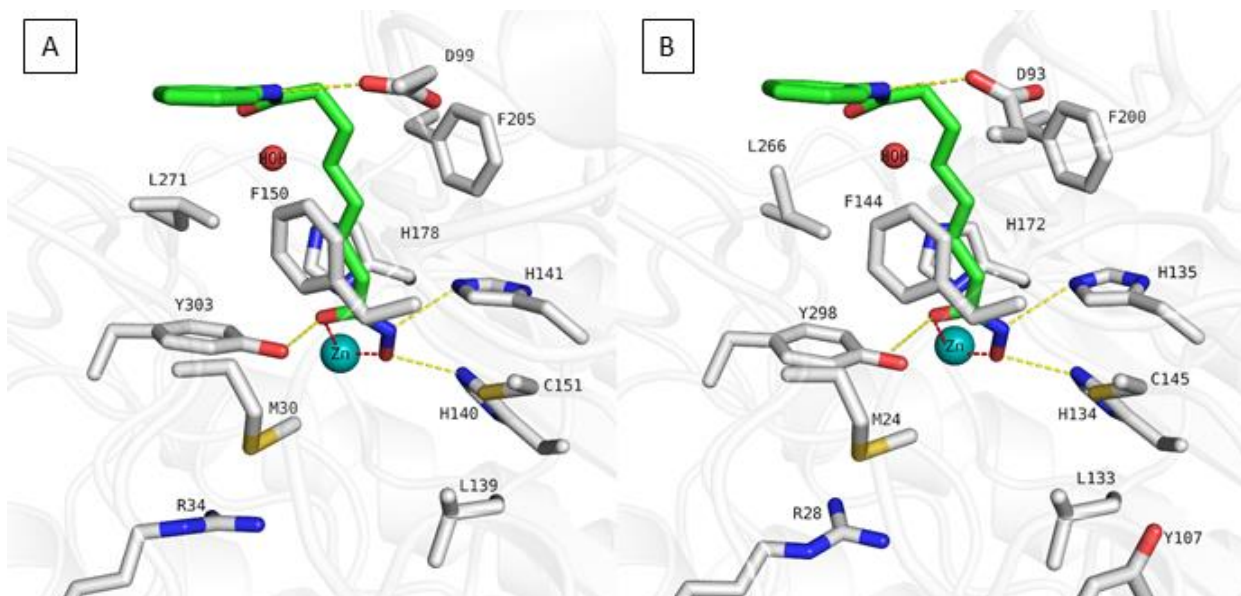
Figure 42. Protein-ligand complexes for HDAC1 and HDAC3. A) in HDAC1 (PDB ID: 4BKX), B) in HDAC3 (PDB ID: 4A69). Ligands were shown with green carbon sticks. Hydrogen bonds (yellow dashed lines) and metal coordination (red dashed lines) between inhibitors and proteins are shown. Relevant residues are shown in stick representation as white carbon atoms in HDAC1 and HDAC3. The zinc ion is shown as cyan coloured sphere. The conserved water molecule is shown as red sphere.

4.2.2.2. Design of compounds containing the hydrazide zinc binding group

In the case of the 2-aminobenzamide scaffold, the aniline moiety was located in the foot pocket of HDAC1-3. Similarly, alkyl side chains of the hydrazides are supposed to be

76

accommodated in the foot pocket of HDAC1-3 and 8. The potency and selectivity profiles of alkylhydrazide-based HDAC inhibitors can be altered by the different chain lengths of the alkyl side chains attached to the hydrazides [101].

Previously, in 2015, the benzoylhydrazide zinc binding group was discovered [115]. Among the synthesized compounds, SR-3558 was identified as a potent and selective class I HDAC1/3 inhibitor (HDAC1 IC_{50} = 0.09 μM, HDAC2 IC_{50} = 0.80 μM, HDAC3 IC_{50} = 0.06 μM, HDAC8 IC_{50} = 2.43 μM) [175]. First, we docked SR-3558 into HDAC1-3, 8, and HDAC6 (Figure 43). The docking analysis revealed that the alkylhydrazide is not able to chelate the zinc ion in HDAC6 due to the steric hindrance of P608 (replaced by L138/144/133 in HDAC1-3, W141 in HDAC8, respectively). Thus, alkylhydrazide based HDAC inhibitors do not show HDAC6 activity. In class I HDACs, the hydrazide warhead binds to the zinc ion in a bidentate fashion. Additionally, it shows hydrogen bond interactions with the conserved residues (H140/145/134/142, H141/146/135/143, and Y303/308/298/306 in HDAC1-3 and 8, respectively). The analysis of the binding mode of alkylhydrazides was studied (done by Matthes Zessin) by doing detailed enzyme kinetic studies using HDAC8, a fluorigenic peptide substrate and the alkylhydrazides compound 80 and 98. For both compounds a reversible binding (checked by jump dilution test) and a substrate-competitive inhibition was detected [176].

In the hydrophobic tunnel, the biphenyl linker group interacts with phenylalanines (F150/155/144/152 and F205/210/200/208 in HDAC1-3 and 8, respectively). The butyl side chain attached to the hydrazide is placed into the foot pocket. These docking results of SR-3558 directed us to test different lengths of *N-alkyl* side chains, which target the foot pocket. Additionally, the acetamidomethylene group was attached to the biphenyl linker to gain hydrogen bond interactions with the conserved aspartate (D99/104/03/101 in HDAC1-3, 8, respectively). Moreover, the aminopyrimidine moiety was tested to see its effect on subtype selectivity. The general structures of synthesized compounds are shown in Table 14.
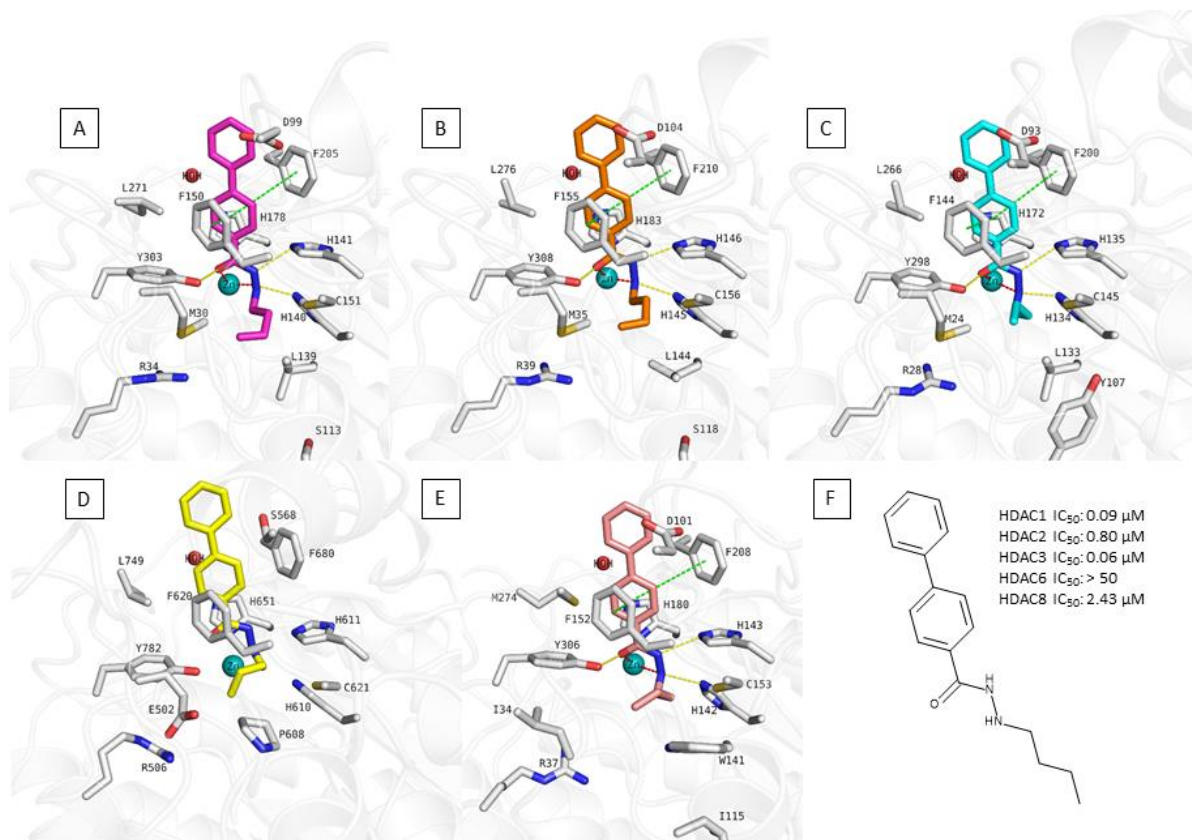
Figure 43.Docking poses of SR-3558 (A, magenta coloured sticks) in HDAC1 (PDB ID: 4BKX), SR-3558 (B, orange coloured sticks) in HDAC2 (PDB ID: 4LY1), SR-3558 (C, cyan coloured sticks) in HDAC3 (PDB ID: 4A69), SR-3558 (D, yellow coloured sticks) in HDAC6 (PDB ID:5EDU), SR-3558 (E, salmon coloured sticks) in HDAC8 (PDB ID: 1T69). Hydrogen bonds (yellow dashed lines), metal coordination (red dashed lines), ionic interactions (blue dashed lines) and aromatic interactions (green dashed lines) between inhibitors and proteins are shown. Relevant residues are shown in stick representation as white carbon atoms in HDAC1, HDAC2, HDAC3, HDAC6 and HDAC8. The zinc ion is shown as cyan coloured sphere. The conserved water molecule is shown as red sphere.

Table 14 General structure of the synthesized compounds against HDAC1-3, HDAC6 and HDAC8 .
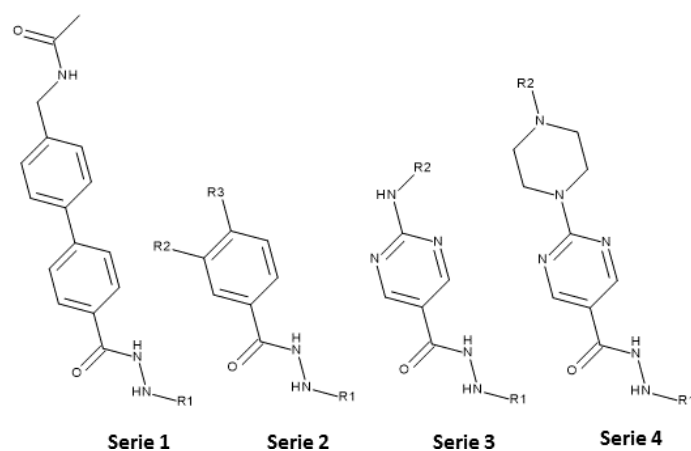
4.2.2.3. Docking of synthesized compounds

The synthesized compounds were docked to the available crystal structures of HDAC1 (PDB ID: 4BKX [25]), HDAC2 (PDB ID: 4LXZ [55]), HDAC3 (PDB ID: 4A69 [24]), HDAC6 (PDB ID: 5EDU [99]), HDAC8 (PDB ID: 1T69 [103]) to understand the structure-activity relationship and find a structural explanation for the subtype selectivity.

Table 15. Inhibitory activity of first series of the synthesized compounds against HDAC1-3, HDAC6 and HDAC8 [176].
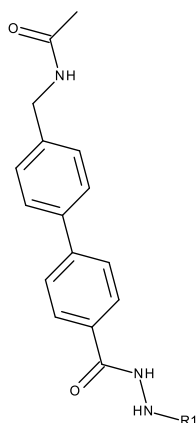
Serie	Name	R1	R2	R3	Inhibitory activity (IC$_{50,}$ µM or % inhibition at a given concentration)				
					HDAC1	HDAC2	HDAC3	HDAC6	HDAC8
1	77	n-propyl	-	-	1.6 ± 0.1	0.63 ± 0.03	0.091 ± 0.003	> 20	0.7 ± 0.07
1	78	n-butyl	-	-	0.62 ± 0.05	1.1 ± 0.1	0.35 ± 0.02	not tested	0.36 ± 0.02
1	79	n-pentyl	-	-	0.66 ± 0.05	2.0 ± 0.2	1.5 ± 0.1	not tested	0.35 ± 0.01
1	80	n-hexyl	-	-	1.8 ± 0.3	12 ± 1	> 20	> 20	0.036 ± 0.002

In the first series of compounds (77-80, Table 15), similar binding poses were observed for 77-79 in HDAC1-3 and 8 (Figure 44), as exemplified by the docking poses of 77 and 80. The acetomidomethylene cap group exhibits hydrogen bond interactions with the conserved aspartate (D93/101 in HDAC3/8, respectively). Similar to the lead compound SR-3558, the biphenyl linker groups of compounds 77 and 80 are sandwiched between two phenylalanine residues (F144/152 and F200/208 in HDAC3/8, respectively). The bidentate chelation was observed between zinc ion and the hydrazide warhead of 77 and 80. It is engaged in a hydrogen

79

bond relationship with H134/142, H135/143, and Y298/306 at the catalytic region in HDAC3/8, respectively (Figure 44). The significant difference, which might explain the selectivity for HDAC3 of compound 7a, was observed in the foot pocket. The n-propyl side chain of compound 77 is well-accommodated in the foot pocket region of HDAC3 compared to other class I HDACs. In HDAC3, L133 makes the foot pocket of HDAC3 narrower by being pushed by Y107 (replaced by S113/S118/W141 in HDAC1/2 and 8, respectively). Hence, the n-propyl fills the foot pocket of HDAC3, resulting in the improved potency of HDAC3. In contrast to 77, other compounds 78-80, having a longer side chain than n-propyl, could not be well-placed into the foot pocket of HDAC3, resulting in a decrease in the HDAC3 inhibitory activity. Docking results of 78, 79, and 80 showed that they clashed with the side chains of M24, R28, and L133 in HDAC3 (Figure 44C). Meanwhile, in HDAC8, whose foot pocket is different in size and shape, compound 80, possessing an n-hexyl chain, perfectly fits into the foot pocket by interacting with I34 and W141. This result might be the explanation for the improved HDAC8 inhibitory potency of compound 80.
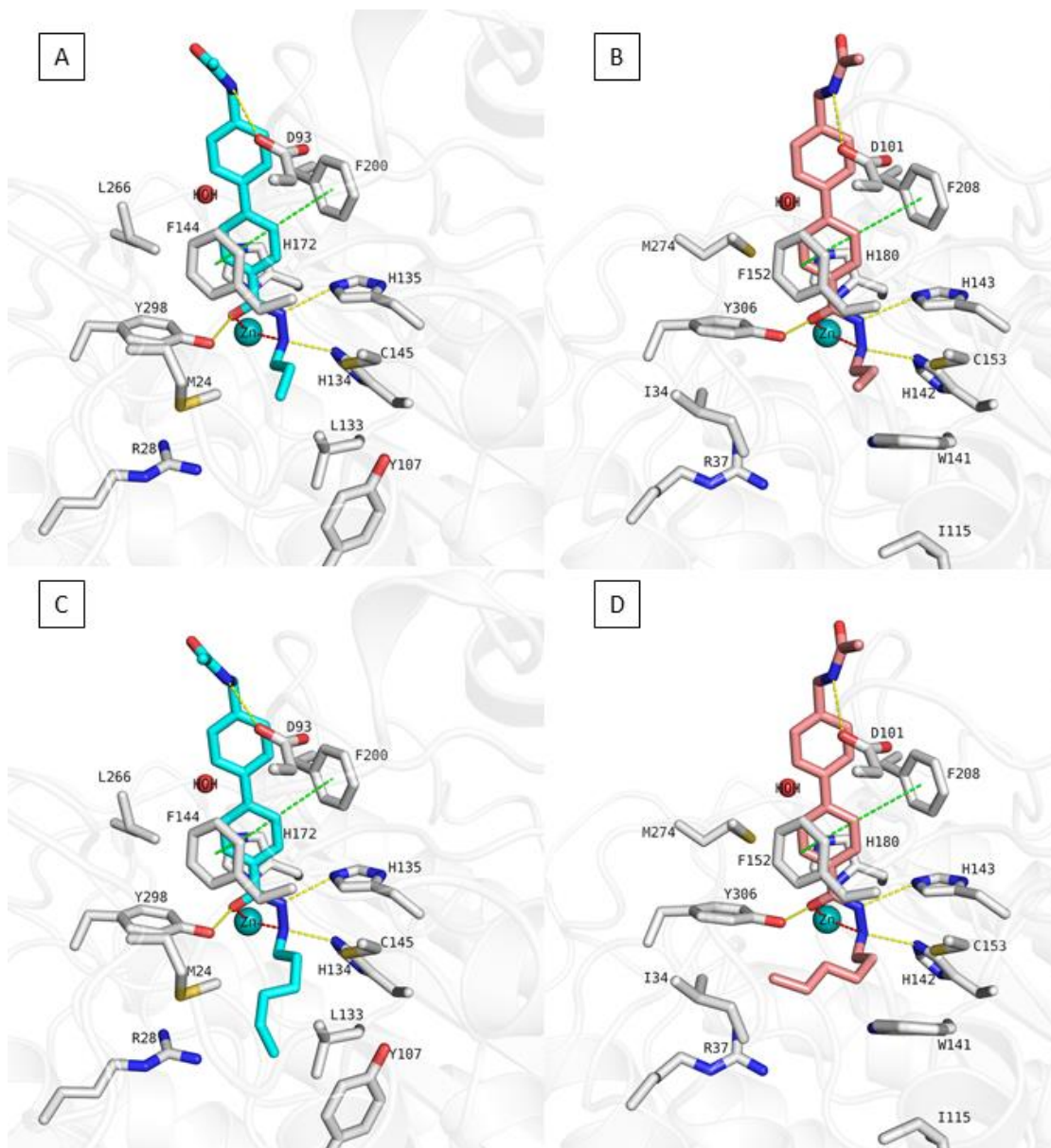
Figure 44. Docking poses of 77 and 80. A) 77 (cyan coloured sticks) in HDAC3 (PDB ID: 4A69), B) 77 (salmon coloured sticks), in HDAC8 (PDB ID: 1T69), C) 80 (cyan coloured sticks), in HDAC3 (PDB ID: 4A69), D) 80 (salmon coloured sticks), in HDAC8 (PDB ID: 1T69). Hydrogen bonds (yellow dashed lines), metal coordination (red dashed lines), and aromatic interactions (green dashed lines) between inhibitors and proteins are shown. Relevant residues are shown in stick representation

81

Table 16. Inhibitory activity of second series of the synthesized compounds against HDAC1-3, HDAC6 and HDAC8 [176].
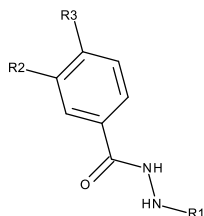
Serie	Name	R1	R2	R3	Inhibitory activity (IC$_{50}$, µM or % inhibition at a given concentration)				
					HDAC1	HDAC2	HDAC3	HDAC6	HDAC8
2	81	n-propyl	H		1.6 ± 0.2	5.5 ± 0.4	1.6 ±0.1	not tested	n.d
2	82	n-hexyl	H		4.8 ± 0.4	12 ± 1	> 20	not tested	0.023 ± 0.001
2	83	n-hexyl	benzylamino	H	> 20	> 20	> 20	> 20	0.046 ± 0.003
2	84	n-hexyl	benzylamino	CH$_3$	35% @10 µM	26% @10 µM	42% @10 µM	not tested	100% @10 µM

In the case of the second series of compounds (Table 16) bearing substituted phenylhydrazide moieties, compound 83 was found as a selective HDAC8 inhibitor (Figure 45). The meta-substituent on the phenyl linker of 83 targets the side pocket of HDAC8 consisting of M274 (replaced by L270/276/266 in HDAC1/2/3, respectively), F152, and Y306. In this side pocket of HDAC8, compound 83 undergoes aromatic interactions with F152 and Y306. The zinc binding and linker groups show the same interaction pattern as observed for the previous series. The hexyl side chain undergoes hydrophobic interactions with I34 and W141 in the foot pocket of HDAC8. Meanwhile, compound 83 is not able to chelate the zinc binding group in HDAC1-3, resulting in a significant loss of HDAC1-3 activity due to the structural difference in the active pocket.
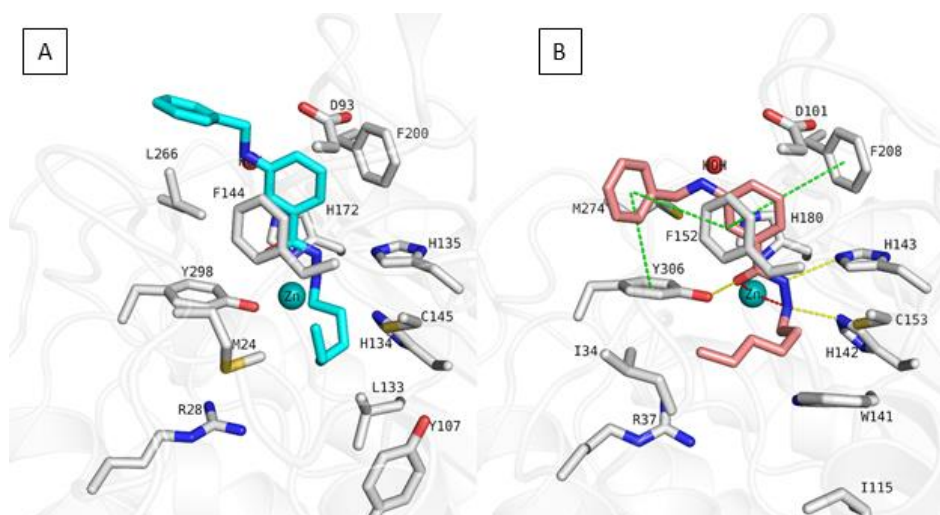
Figure 45. Docking poses of 83 (A, cyan coloured sticks) in HDAC3 (PDB ID: 4A69), 83 (B, salmon coloured sticks), in HDAC8 (PDB ID: 1T69). Hydrogen bonds (yellow dashed lines), metal coordination (red dashed lines), and aromatic interactions (green dashed lines) between inhibitors and proteins are shown. Relevant residues are shown in stick representation as white carbon atoms in HDAC3 and HDAC8. The zinc ion is shown as cyan coloured sphere. The conserved water molecule is shown as red sphere.

Table 17. Inhibitory activity of third series of the synthesized compounds against HDAC1-3, HDAC6 and HDAC8 [176].
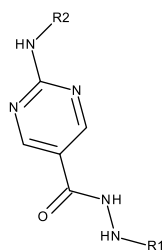
Serie	Name	R1	R2	R3	Inhibitory activity (IC$_{50}$, µM or % inhibition at a given concentration)				
					HDAC1	HDAC2	HDAC3	HDAC6	HDAC8
3	85	n-propyl		-	0.25 ± 0.02	0.7 ± 0.03	0.043 ±0.005	> 20	1.0 ± 0.11
3	86	n-butyl		-	85% @10 µM	93% @10 µM	0.20 ± 0.01	not tested	94% @10 µM
3	87	n-propyl		-	85% @10 µM	90% @10 µM	99% @10 µM	not tested	89% @10 µM
3	88	n-propyl		-	91% @10 µM	93% @10 µM	0.081 ± 0.002	not tested	83% @10 µM

83
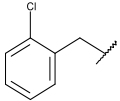
3	89	n-propyl		-	89% @10 μM	92% @10 μM	0.060 ± 0.001	not tested	87% @10 μM
3	90	n-propyl		-	92% @10 μM	96% @10 μM	0.037 ± 0.001	not tested	88% @10 μM
3	91	n-propyl		-	88% @10 μM	n.d	0.058 ± 0.002	not tested	83% @10 μM
3	92	n-propyl		-	0.29 ± 0.02	0.92 ± 0.04	0.11 ± 0.01	not tested	n.d
3	93	n-hexyl		-	8.3 ± 1.2	> 20	> 20	not tested	0.063 ± 0.004
3	94	n-hexyl		-	2.2 ± 0.1	12 ± 1	7.2 ± 0.2	not tested	0.28 ± 0.002
3	95	n-hexyl		-	0.56 ± 0.03	3.2 ± 0.2	3.0 ± 0.2	not tested	0.016 ± 0.001
3	96	n-hexyl		-	0.96 ± 0.06	4.5 ± 0.3	8.5 ± 0.4	not tested	0.019 ± 0.001
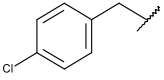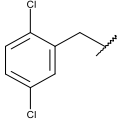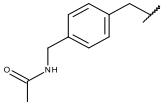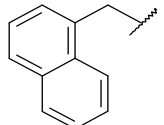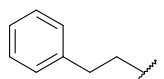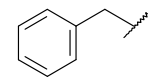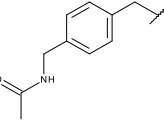
Similar binding modes were observed in the third series of compounds (85-96, Table 17) bearing different aromatic cap groups and different lengths of foot pocket targeting alkyl chains. The docking poses were exemplified by the obtained docking poses of 85 and 95 (Figure 46). The n-propyl chain of compound 85 is placed into the foot pocket of HDAC3, resulting in improved potency for HDAC3. The zinc binding group shows bidentate chelation with zinc ion and hydrogen bond interactions with H134, H135 and Y298 in HDAC3. The aminopyrimidine linker group is accommodated in a sandwiched position between F144 and F200 in the hydrophobic tunnel of HDAC3. The benzylamino cap group attached to the p-position of the aminopyrimidine moiety is stacked on F144 in HDAC3. On the other hand, replacing n-propyl with n-hexyl caused an improvement in HDAC8 selectivity. The n-hexyl chain of compound 95 undergoes hydrophobic interactions with I34 and W141 in the foot pocket of HDAC8 (Figure 46D). In HDAC3, it is clashing with the surrounding residues (M24, R28, and L133).
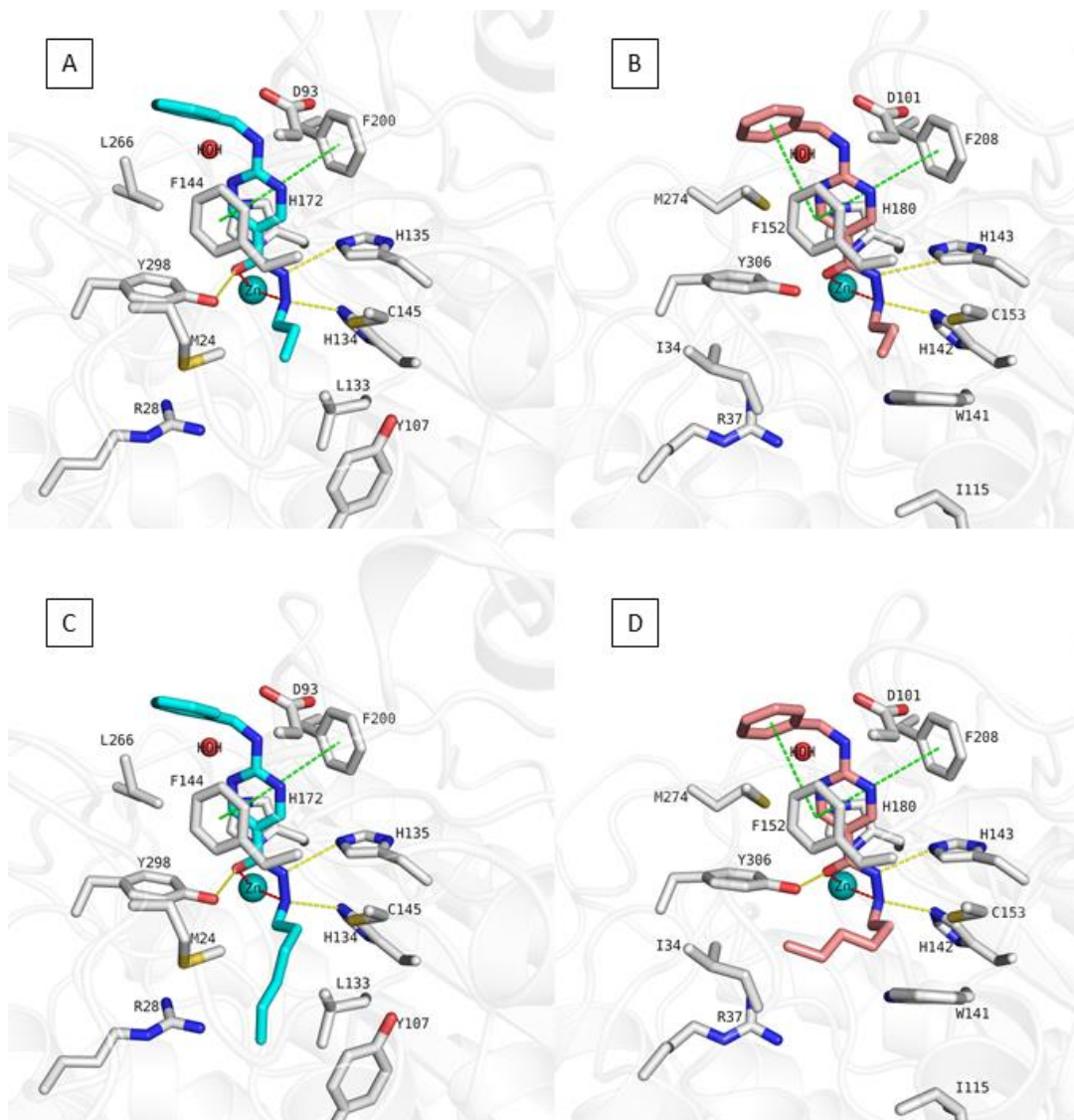
Figure 46. Docking poses of 85 and 95. A) 85 (cyan coloured sticks) in HDAC3 (PDB ID: 4A69), B) 85 (salmon coloured sticks), in HDAC8 (PDB ID: 1T69), C) 95 (cyan coloured sticks), in HDAC3 (PDB ID: 4A69), D) 95 (salmon coloured sticks), in HDAC8 (PDB ID: 1T69). Hydrogen bonds (yellow dashed lines), metal coordination (red dashed lines), and aromatic interactions (green dashed lines) between inhibitors and proteins are shown. Relevant residues are shown in stickrepresentation

Table 18. Inhibitory activity of forth series of the synthesized compounds against HDAC1-3, HDAC6 and HDAC8 [176].
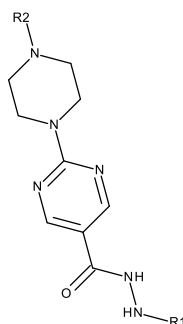
Serie	Name	R1	R2	R3	Inhibitory activity (IC$_{50}$, µM or % inhibition at a given concentration)				
					HDAC1	HDAC2	HDAC3	HDAC6	HDAC8
4	97	n-propyl	H	-	0.59 ± 0.03	2.4 ± 0.1	0.12 ± 0.01	not tested	0.25 ± 0.01
4	98	n-hexyl		-	0.073 ± 0.007	1.1 ± 0.1	0.030 ± 0.001	not tested	0.0082 ± 0.0006
4	99	n-hexyl		-	0.17 ± 0.01	0.31 ± 0.01	0.10 ± 0.04	> 20	0.0059 ± 0.0006
4	100	n-hexyl		-	0.17 ± 0.01	0.33 ± 0.02	0.30 ±0.02	not tested	0.014 ± 0.001
4	101	n-hexyl		-	0.86 ± 0.07	1.40 ± 0.10	1.00 ± 0.10	not tested	0.013 ± 0.001
4	102	n-hexyl		-	0.46 ± 0.03	1.20 ± 0.10	1.40 ± 0.10	not tested	0.023 ± 0.002

The last series of compounds (97-102, Table 18) bearing pyrimidine/piperazine as linker group and indole cap group is exemplified by the docking pose of 98 and 99 (Figure 47). In contrast to other derivatives containing a hexylhydrazide moiety, this series of compounds showed high inhibitory activity on all class I HDACs. The docking poses of compounds 98 and

99 revealed that the indole capping group displays aromatic interactions with F200/208 in HDAC3/8, respectively. The piperazine establishes ionic interactions with the conserved aspartate (D93/101 in HDAC3/8, respectively). Most likely, the π-π interactions with F200/208 and the ionic interactions with D93/101 in HDAC3/8, respectively, improved the activity of this series of compounds. Moreover, in all cases, the pyrimidine linker group is sandwiched between F144/152 and F200/208 in HDAC3/8, respectively. The hexyl chain of compound 99 shows hydrophobic interactions with I34 and W141, resulting in selectivity for HDAC8, while it clashes with M24, R28, and L133 in HDAC3, resulting in a significant decrease in HDAC3 inhibitory activity.
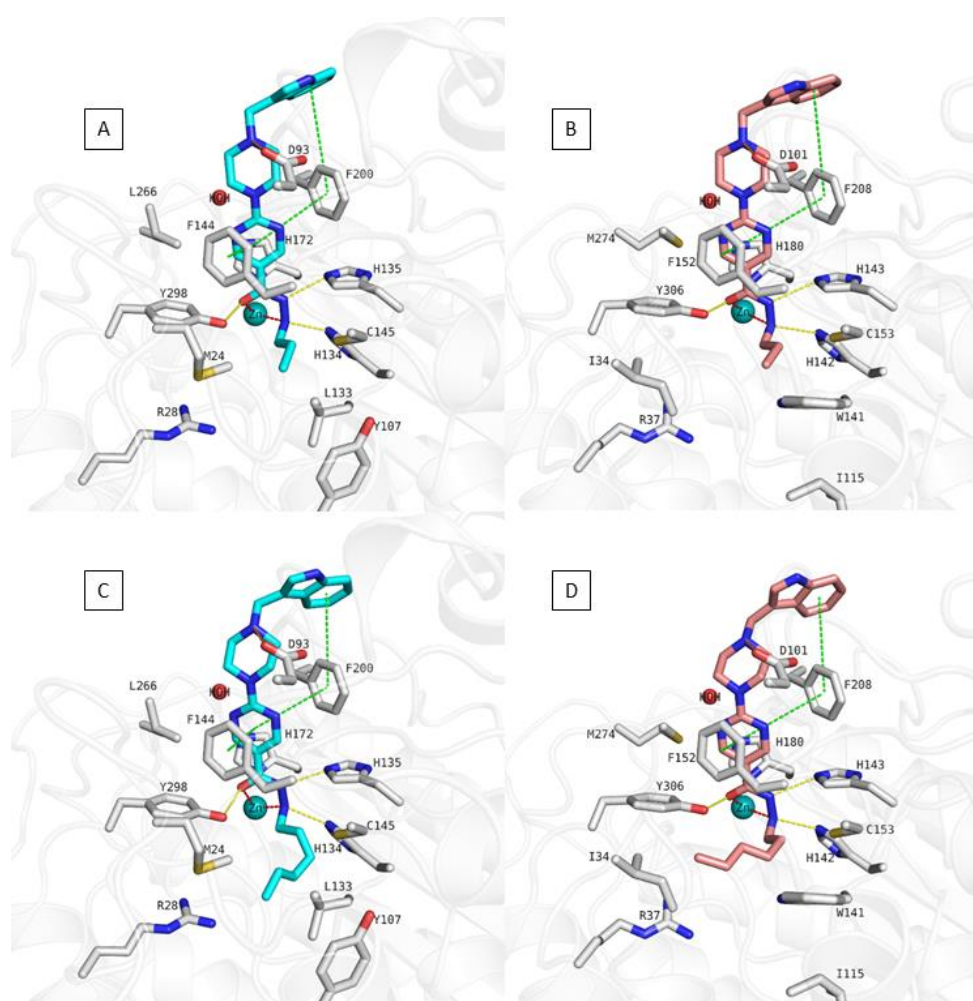
Figure 47. Docking poses of 98 and 99. A) 98 (cyan coloured sticks) in HDAC3 (PDB ID: 4A69), B) 98 (salmon coloured sticks), in HDAC8 (PDB ID: 1T69), C) 99 (cyan coloured sticks), in HDAC3 (PDB ID: 4A69), D) 99 (salmon coloured sticks), in HDAC8 (PDB ID: 1T69). Hydrogen bonds (yellow dashed lines), metal coordination (red dashed lines), and aromatic interactions (green dashed lines) between inhibitors and proteins are shown. Relevant residues are shown in stick representation

To summarize the docking results, four series of 26 compounds have been designed, synthesized, and their binding modes have been analyzed. The first series of compounds having an acetamidomethyl capping group showed hydrogen bond interactions with D93 and D101 in HDAC3/8, respectively. The compounds possess different lengths of alklyhydrazide. The n-propyl derivative showed HDAC3 selectivity, while the n–hexyl derivative showed HDAC8 selectivity over other HDACs. In the second series of compounds, the attachment of benzylamino to the 3rd position of the phenyl linker group with the proper alkyl length resulted in HDAC8 selectivity due to fitting into the selectivity pocket of HDAC8. In the third series of compounds having an aminopyrimidine linker group and different N-arylpiperazine moieties as a capping group, the majority of the compounds having an n-propyl group attached to hydrazide showed nanomolar inhibitory activity and selectivity for HDAC3 enzyme. The last series having N-methylindole as a capping group showed improved HDAC8 activity over other HDACs. As a result, we have noticed that the length of the alkyl group attached to the hydrazide moiety has a crucial impact on selectivity. The n-propyl group is favorable for the HDAC3 selectivity, and the n-hexyl group seems proper for HDAC8 selectivity over other HDACs. The addressing of the selectivity pocket of HDAC8 also improves the selectivity profile of compounds.

4.2.2.4. Molecular dynamics simulation of the isoform-selective compounds 77 and 80

The 50 ns molecular dynamics (MD) simulations were performed for the most promising compounds 77 and 80 in HDAC1, 2, 3, and 8, to check the protein-ligand interaction stability of the protein-ligand complexes. MD simulations were analyzed by means of RMSD and distance analysis of essential interactions.

In the case of compound 77 in HDAC1, 2, 3 and 8 (Figure 48), the RMSD analysis revealed that the protein and zinc ion are stable throughout the MD. The ligand showed fluctuations due to the solvent-exposed acetamidomethylene capping group. The detailed analysis of MD showed that the zinc binding group of compound 77 conserves its bidentate chelation with the

zinc ion during the 50 ns MD in HDAC2, HDAC3 and HDAC8. At the same time, the hydrazide warhead does not keep its bidentate chelation in HDAC1. The nitrogen atom, which interacts with the zinc ion, changed its position. Additionally, the zinc ion moved away a bit from that nitrogen atom in HDAC1. In the hydrogen bond analysis, catalytic tyrosines (Y303/308/298/306) are observed as flexible. Interactions with histidines (H140/145/134/142 and H141/146/135/143 in HDAC1-3 and 8, respectively) were preserved in all cases. Furthermore, in all cases, the biphenyl linker group maintains its $\pi - \pi$ stacking interactions with the phenylalanine residues (F150/155/144/152 and F205/210/200/208 in HDAC1-3 and 8, respectively).

In the case of compound 80 (Figure 49), the flexibility of the solvent-exposed acetamidomethylene group was observed in all cases. The observed zinc coordination distance was maintained in HDAC1, HDAC3 and HDAC8. The catalytic Y303 was observed as flexible in HDAC1. The $\pi - \pi$ interactions with F150 and F200 were retained in HDAC1. In the case of HDAC2, interestingly, the zinc chelation was broken and consequently lost its activity in HDAC2. In addition, the sandwiched position of compound 80 between F155 and F210 in HDAC2 was lost due to the deviation of F155 and F210. In the case of HDAC3, the bidentate zinc coordination, hydrogen bonds within the zinc binding region and aromatic interactions with F144 and F200 were kept. Most likely, the n-hexyl alkyl chain clashed with the surrounding residues in the foot pocket and caused a loss of HDAC3 activity. In HDAC8, the ligand kept its initial interactions. The n-hexyl side chain took a favourable position in the foot pocket, and compound 80 gained selectivity for HDAC8 over other class I HDACs.
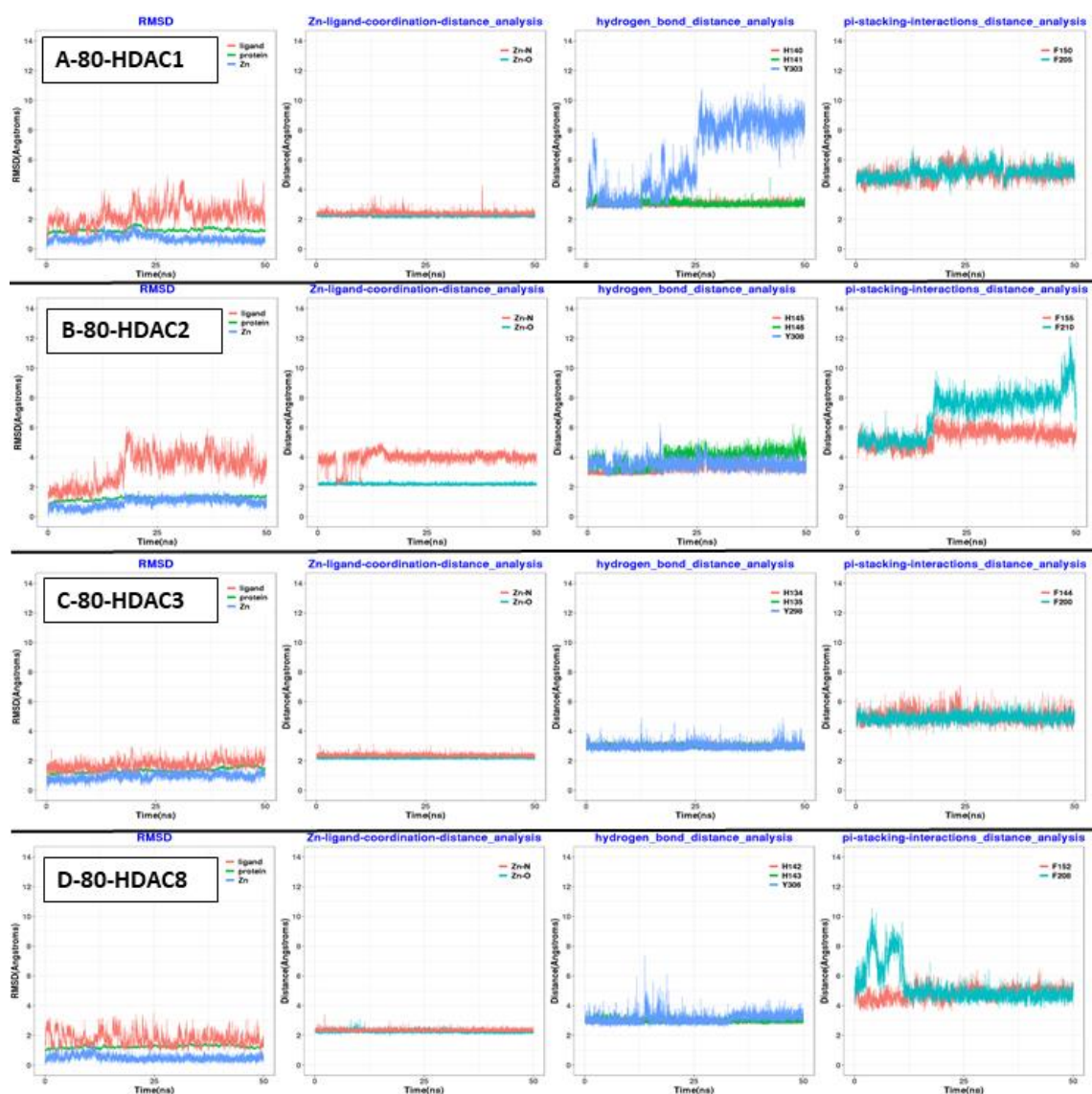
Figure 49. Analysis of 50 ns MD simulation for 80 in HDAC1-3 and 8. A) in HDAC1 (PDB ID: 4BKX), B) in HDAC2 (PDB ID: 4LXZ) C) in HDAC3 (PDBID: 4A69), D) in HDAC8 (PDB ID: 1T69). RMSD, Zn-ligand coordination distance analysis, hydrogen bond distance analysis and pi-stacking interaction distance analysis were shown.

MD simulations of compounds 77 and 80 revealed that *N*-alkylhydrazide derivatives bind to the catalytic pocket of HDAC1-3 and 8. In addition, the *N*-alklyhydrazide group functions as a zinc binder and the alkyl chain interacts with the surrounding residues in the foot pocket of HDAC1-3 and 8. The size and shape differences in foot pocket among class I HDACs might be utilized to design selective HDAC3 or HDAC8 inhibitors based on the length of the alkyl chain.

4.3. Design of inhibitors of LpxCs

4.3.1. Hydroxamic Acid Derivatives

A hydroxamic acid warhead has been identified as a potent UDP-3-O-(R-3-hydroxymyristoyl)-N-acetylglucosamine deacetylase (LpxC) inhibitor [71]. The analysis of the crystal structure of *Escherichia coli* LpxC in a complex with LPC-053 (PDB ID: 3PS3 [72]) revealed that the diphenyldiacetylene group penetrates through the hydrophobic substrate binding tunnel and the threonyl-hydroxamate group is located at the active site and directed toward the hydrophobic patch of the LpxC enzyme (Figure 50). The hydroxamate warhead chelates the zinc ion in a bidentate manner through its carbonyl oxygen and hydroxyl oxygen. Additionally, the hydroxamate group forms hydrogen bond interactions with T191 and E78 in the active site. The threonyl moiety of LPC-053 forms van der Waals interactions with the side chain of F192 and water-mediated interactions with the backbone of F192 and C63 in the hydrophobic patch of enzyme. Additionally, the amide moiety of LPC-053 establishes hydrogen bond interactions with the side chain of T191 and the backbone of C63. The diphenyldiacetylene group of LPC-053 is accommodated in the hydrophobic substrate binding tunnel consisting of L18, M195, I198, C207, F212, A215, V217 and forms favourable hydrophobic interactions inside the tunnel.
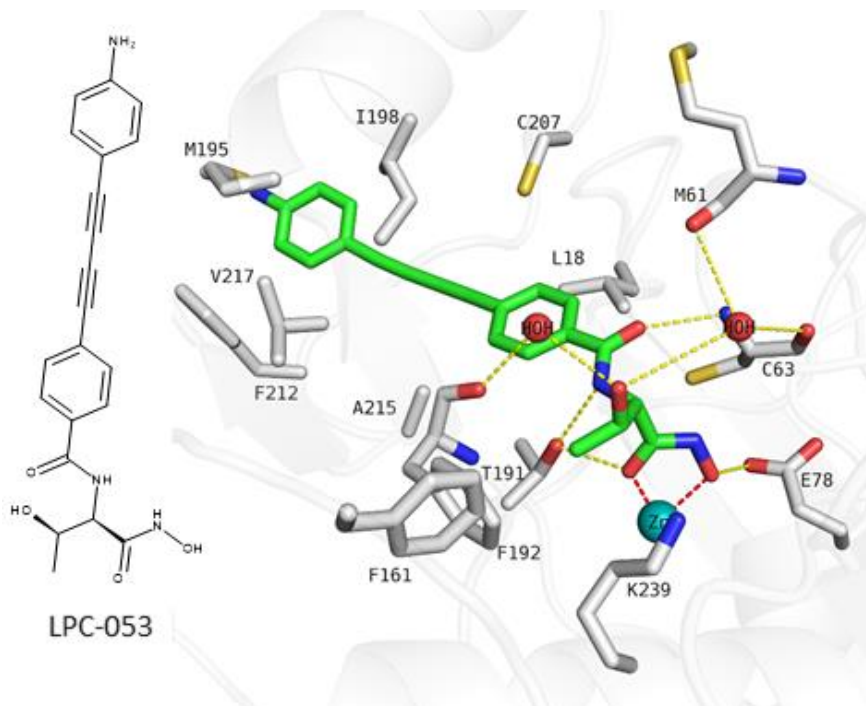
Figure 50. Binding mode of LPC-053 in E.coli LpxC (PDB ID: 3PS3).Ligand is shown as green carbon sticks. Protein backbone is shown as white carbon colour. Ribbons are shown in white colour. The zinc ion is shown as cyan coloured sphere. The water molecule is shown as red sphere.

Redocking studies were performed to find an appropriate docking protocol that could reproduce the co-crystallized ligand. The re-docked pose of the ligand was found to be in good agreement with the co-crystallized ligand with an RMSD of 0.29 Å (Figure 51).
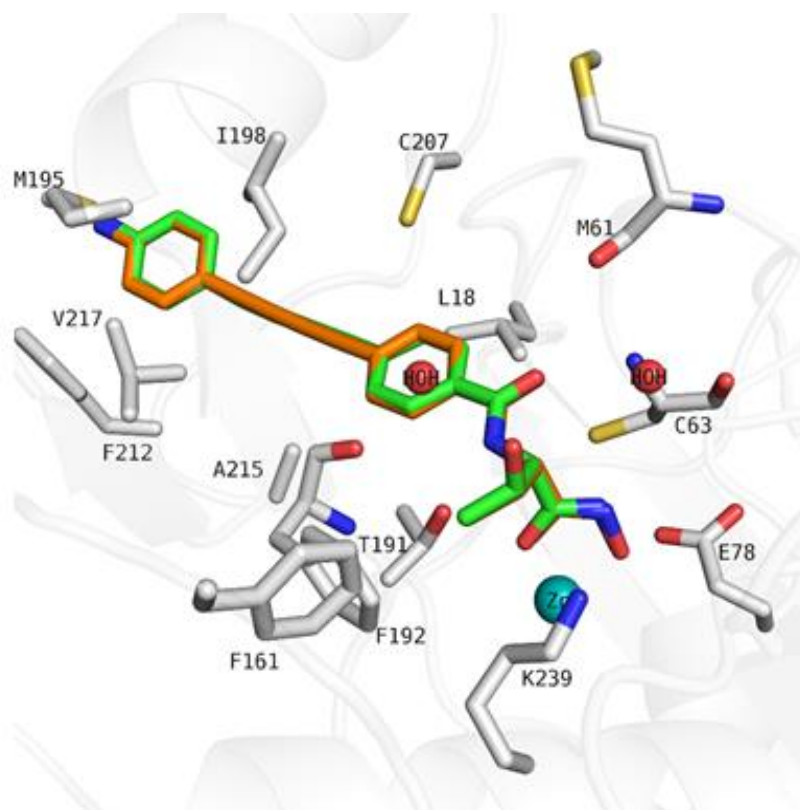
Figure 51. Re-docking results of E. coli LpxC in a complex with LPC-053 (PDB ID: 3PS3). The re-docked pose was shown as sticks with orange carbon atoms, and co-crystallized ligands as sticks with green carbon atoms. Protein backbone was shown with white carbon colour. Ribbons were shown with white colour. The zinc ion is shown as cyan coloured sphere. The water molecule is shown as red sphere.

4.3.1.1. Design of synthesized compounds

Five series of compounds were synthesized and tested against *Escherichia coli* gram-negative bacteria (Figure 52 and Table 19). The same numbering system for the compounds was used, as shown in the published articles [165-167]. The compounds were designed by modifying CHIR-090, which is an N-aroyl-L-threonine hydroxamic acid derivative. The N-aroyl-L-threonine part of the CHIR-090 interacts favorably with the residues in the hydrophobic patch of LpxC enzyme. Modifying this part of CHIR-090 enables us to reach the basic patch and/or to interact with more residues in hydrophobic patch. For this purpose, the ether moiety was used instead of the amide moiety of CHIR-090 in all cases. In the first series [167], the threonyl side chain of CHIR-090 was incorporated into the dihydoxytetrahydrofuran ring to restrict the conformation. Compounds containing C-furanosides (compound 1-8, scaffold A) have been modified by changing the stereoisomer of hydroxyl groups on the tetrahydrofuran

ring at third and fourth positions. In the second series [165], the compounds bearing a monohydroxytetrahydrofuran ring (compound 9-14, scaffold B and C) were tested against *E.coli* LpxC enzyme. These novel compounds were designed by modifying the compounds 2, 4, 5, and 7 synthesized in the first series. The hydroxyl group, either in position 3 or 4 of the tetrahydrofuran ring, was removed to investigate the impact of the removal of one of the two hydroxyl groups. In the third series of compounds, the open-chained benzyloxyacetohydroxamic acids (compound 15-18, scaffold D) were tried to test the impact of the conformational restriction on the LpxC inhibitory activity. In the fourth series of compounds (compound 19-29, scaffold E, F, and G) [166], the previously synthesized compound 19 [177], having benzyloxyacetohydroxamic acid, was chosen as a lead compound. The hydroxyl group of the lead compound was replaced by a triazole ring. Additionally, the polar or non-polar groups are substituted in the triazole ring to test their effect on LpxC inhibitory activity. In the last series of compounds (compound 30-39, scaffold H, I and J) [178], the previously synthesized compound 132 (T901) and compound 133 (G12) [179] were selected as lead compounds. A substituent was introduced at the β-carbon atom of the hydroxamic acid of lead compounds to gain favourable interactions with the LpxC enzyme.
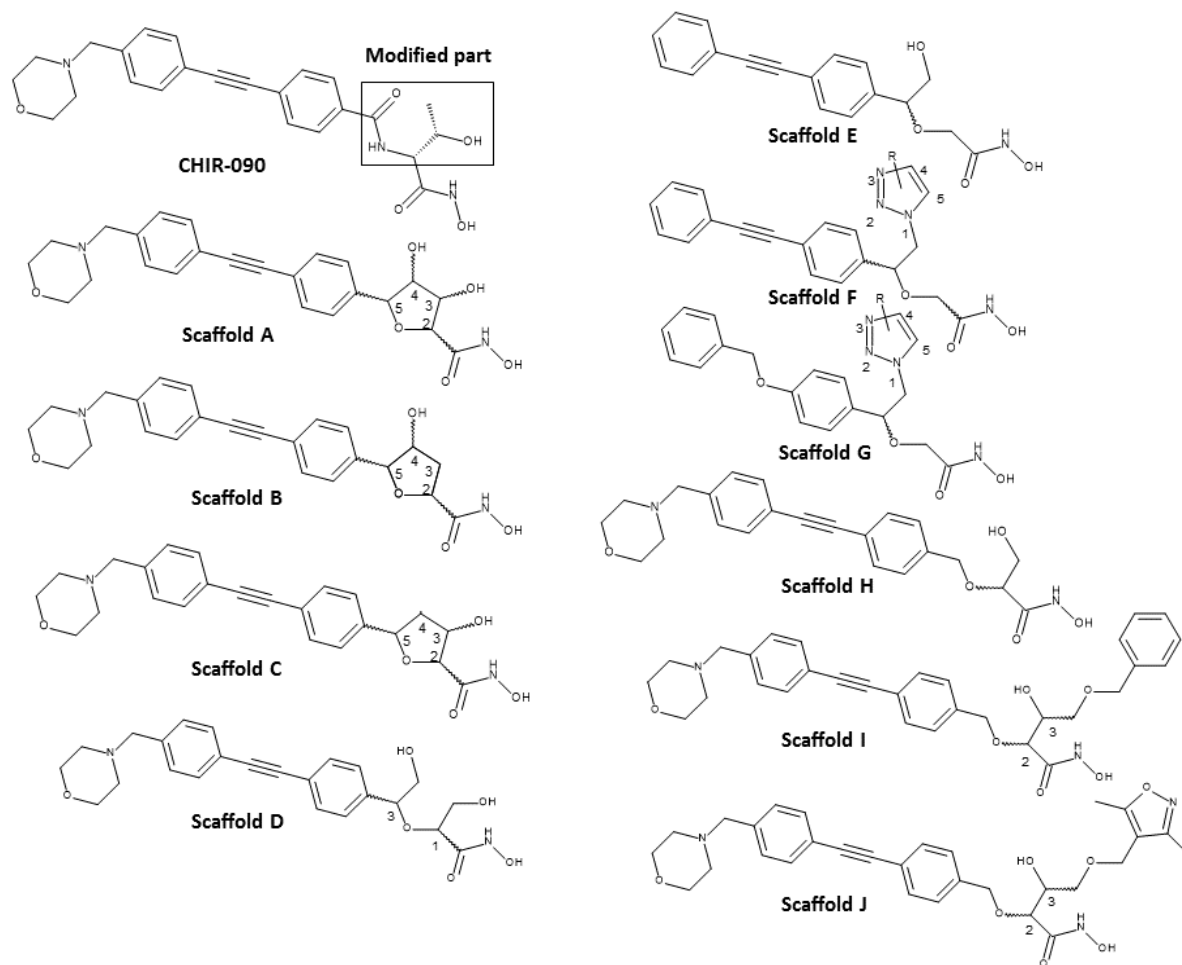
Figure 52. 2D representation of reference inhibitor and synthesized compounds.

Table 19. İnhibitory activity of synthesized compounds against LpxC.

Name	Serie	Scaffold	Code in the article	enantiomer	LpxC IC$_{50}$ μM	Reference
103	1	A	1	2R, 3R, 4S, 5R	28.2 ± 9	[167]
104	1	A	2	2R, 3R, 4S, 5S	10 ± 1	[167]
105	1	A	3	2S, 3R. 4S. 5R	34 ± 10	[167]
106	1	A	4	2S, 3R, 4S, 5S	>200	[167]
107	1	A	12	2R, 3S, 4R, 5R	>200	[167]
108	1	A	13	2R, 3S, 4R, 5S	90 ± 35.6	[167]
109	1	A	14	2S, 3S, 4R, 5R	127.4 ± 15.6	[167]
110	1	A	15	2S, 3S, 4R, 5S	3.2 ± 1.0	[167]
111	2	B	9	2R, 4R, 5R	>200	[165]
112	2	B	ent-9	2S, 4S, 5S	193.9 ± 70.5	[165]
113	2	B	10	2R, 4S, 5S	>200	[165]
114	2	B	ent-10	2S, 4R, 5R	>200	[165]
115	2	C	8	2R, 3S, 5S	56.3 ± 16.5	[165]

116	2	C	ent-8	2S, 3R, 5R	23.7 ± 17.6	[165]
117	3	D	5	1R, 3R	180 ± 4	[167]
118	3	D	6	1R, 3S	8.0 ± 0.6	[167]
119	3	D	7	1S, 3R	21 ± 3	[167]
129	3	D	8	1S, 3S	2.6 ± 0.3	[167]
121	4	E	lead	S	86.2 ± 1.9	[166]
122	4	E	ent-lead	R	>200	[166]
123	4	F	32	S	36 ± 1.7	[166]
124	4	F	ent-32	R	>200	[166]
125	4	G	29	S	>200	[166]
126	4	F	27	S	10.4 ± 9.7	[166]
127	4	F	ent-27	S	>200	[166]
128	4	G	23	S	>200	[166]
129	4	F	37	S	>20	[166]
130	4	F	35	S	8.5 ± 1.3	[166]
131	4	F	40	S	23.4 ± 5.8	[166]
132	5	H	T901	2S	2.8 ± 0.5	[178]
133	5	H	G12	2R	1.6 ± 0.31	[178]
134	5	I	BM13	2S, 3S	1.7 ± 1.3	[178]
135	5	I	RL08	2S, 3R	39.58 ± 37.36	[178]
136	5	I	LD08	2R, 3S	5.87 ± 2.03	[178]
137	5	I	LD12	2R, 3R	9.17 ± 0.88	[178]
138	5	J	BM19	2S, 3S	2.23 ± 0.80	[178]
139	5	J	MG25	2S, 3R	92.7 ± 31.5	[178]
140	5	J	SW30	2R, 3S	27.0 ± 10.1	[178]
141	5	J	SW32	2R, 3R	43.5 ±10.4	[178]
Ref	Ref.		CHIR-090	-	0.076 ± 0.003	[166]

4.3.1.2. Docking of synthesized compounds

Synthesized compounds were docked to the *E. coli* LpxC crystal structure (PDB ID: LPC-053) to explore the structure-activity relationship of novel hydroxamic acid derivatives.

Analysis of docking poses of the first series of compounds (103 – 110, scaffold A, Table 19) demonstrated that they bind similarly to the LpxC as known inhibitors (CHIR-090 and LPC compounds). The common parts of the first series are the diphenylacetlylene part and hydroxamic acid zinc binder. The diphenylacetylene moiety is located in the hydrophobic tunnel composed of L18, F192, M195, I198, A215, F212, and V217. In all cases, the hydroxamic acid moiety chelates the catalytic zinc ion in a bidentate fashion through both oxygen atoms, except in inactive compounds 106 and 107. The hydroxyl and carbonyl groups

of the hydroxamate moiety form hydrogen bonds with the side chains of E78 and T191. The differences in the binding mode were observed in the orientation of the tetrahydrofuran ring (compounds 103-110).

Most of the active compounds (103, 104, 105, and 110) exhibit water-bridge interactions with the neighboring residues M61, C63, T191, and F192. Their hydroxyl groups on the tetrahydrofuran ring were solvent-exposed at the entrance of the pocket (Figure 53). In particular, the water-bridge interactions might be the reason for the high inhibitory activity of these compounds.

Figure 53. Docking poses of compound 103, 104, 105 and 110. A) Compound 103, B) compound 104, C) compound 105 and D) Compound 110 in LpxC (PDB ID: 3PS3). Ligands are shown as green coloured sticks. Ribbons are shown as white colour. Relevant residues are shown in stick representation as white carbon atoms. The zinc ion is shown as cyan coloured sphere. The conserved

Less active compounds 108 and 109 show several hydrogen bond interactions. However, the 3-hydroxyl group of compound 108 lost its water-bridge interaction with F192. In the case of compound 109, the 4-hydroxyl group lost its hydrogen bond with M61 and the water-bridge interaction with F192 and was directed toward L18 inside the pocket. The loss of water-bridge interaction might be the reason behind the reduced inhibitory activity of compounds 108 and 109 (Figure 54A/B). The inactive compounds 106 and 107 do not fit into the pocket due to the unfavourable linker orientation. They lost their bidentate chelation with a zinc ion. The removal of the bidentate chelation resulted in a total loss of the LpxC inhibitory activity of compounds 106 and 107 (Figure 54C/D).

Figure 54. Docking poses of compound 108, 109, 106 and 107. A) Compound 108, B) compound 109, C) compound 106 and D) Compound 107 in LpxC (PDB ID: 3PS3). Ligands are shown as green

99

In the second series of compounds (111-114, scaffolds B and C, Table 19), the impact of the hydroxyl groups on the tetrahydrofuran ring was investigated. Removing the 3-hydroxyl groups of the inactive compounds all-cis-configured 106 and 107 yields compounds 111 and 112 (Figure 55). The loss of the 3-hydroxyl group did not result in a significant improvement in the activities of compounds 111 and 112. In the case of compound 111, the hydroxyl group on the tetrahydrofuran ring is clashing with the water molecule. The unfavourable orientation of the ring causes a loss of the bidentate chelation with the zinc ion. This might be the reason behind the loss of LpxC inhibitory activity of compound 111. Compound 112, an enantiomer of compound 111, demonstrated bidentate chelation with zinc ion as well as a hydrogen bond with E78 and T191. The hydroxyl group has an unfavourable orientation pointing toward the hydrophobic residue L18 in the pocket.
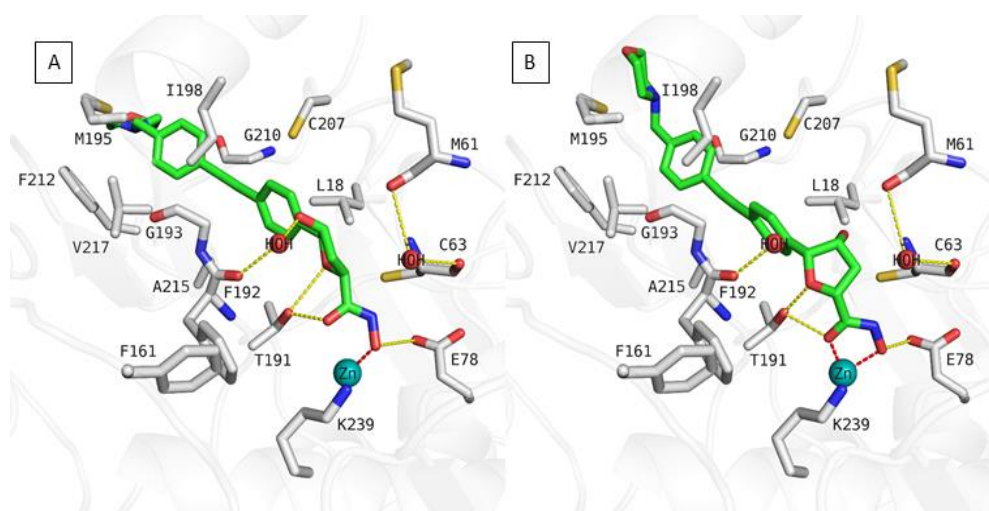
Figure 55. Docking poses of compound 111 and 112. A) Compound 111 and B) compound 112 in LpxC (PDB ID: 3PS3). Ligands are shown as green coloured sticks. Ribbons are shown as white colour. Relevant residues are shown in stick representation as white carbon atoms. The zinc ion is shown as cyan coloured sphere. The conserved water molecule is shown as red. Hydrogen bonds (yellow dashed lines), metal coordination (red dashed lines) between inhibitors and protein are shown.

Removal of the 3-hydroxyl group of the most active compound 104 leads to compound 113 (Figure 56). The absence of the 3-hydroxyl group caused the total loss of the LpxC inhibitory activity. A comparison of the docking poses of compounds 104 and 113 revealed that compound 113 forms a water-bridge interaction with F192 and hydrogen bond interactions with M61 but does not build up a water-bridge interaction with C63, in contrast to compound 104 (Figure 56A/B). The absence of the water-bridge interaction with C63 probably causes the loss of the activity in the case of compound 113. Its enantiomer compound 114 shows no bidentate chelation with the zinc ion (Figure 56C). Its hydroxyl group is directed toward L18 in the pocket, as observed in compound 112 (Figure 55B). It seems that the hydrophobic interaction with L18 is not favourable. This might be the reason for the total loss of the LpxC inhibitory activity for compound 114.
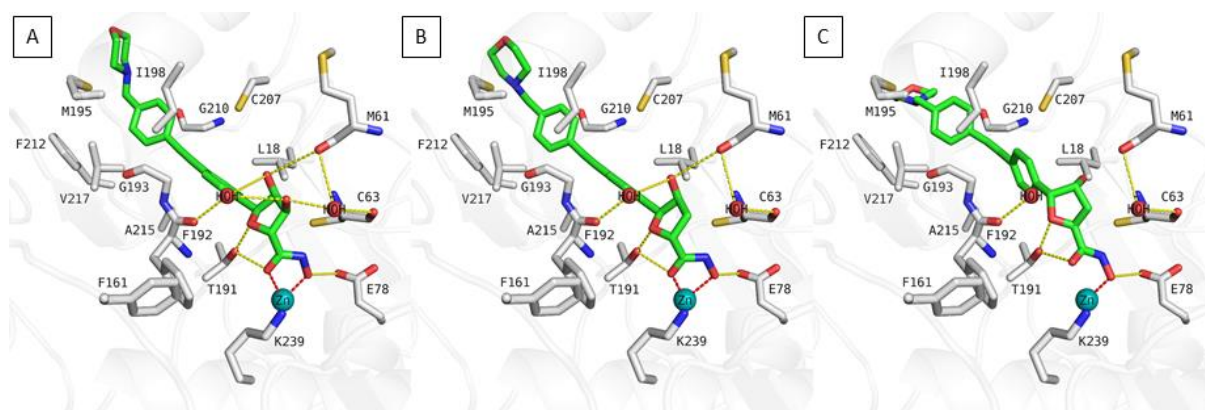
Figure 56. Docking poses of compound 104, 113 and 114.A) Compound 104, B) compound 113, and C) compound 114 in LpxC (PDB ID: 3PS3). Ligands are shown as green coloured sticks. Ribbons are shown as white colour. Relevant residues are shown in stick representation as white carbon atoms. The zinc ion is shown as cyan coloured sphere. The conserved water molecule is shown as red. Hydrogen bonds (yellow dashed lines), metal coordination (red dashed lines) between inhibitors and protein are shown.

The shift of the hydroxyl from 4th to 3rd position on compound 111 leads to compound 115 (Figure 57). Surprisingly, compound 115 and its enantiomer compound 116 showed improved LpxC inhibitory activity. Compound 115 showed hydrogen bond interactions with C63 and one of the solvent molecules (close to C63), while compound 116 formed hydrogen bonds with T191, F192, and one of the solvent molecules (close to F192) (Figure 57A/B). The hydroxyl at the 3rd position of the tetrahydrofuran ring seems more favourable than at the position 4.
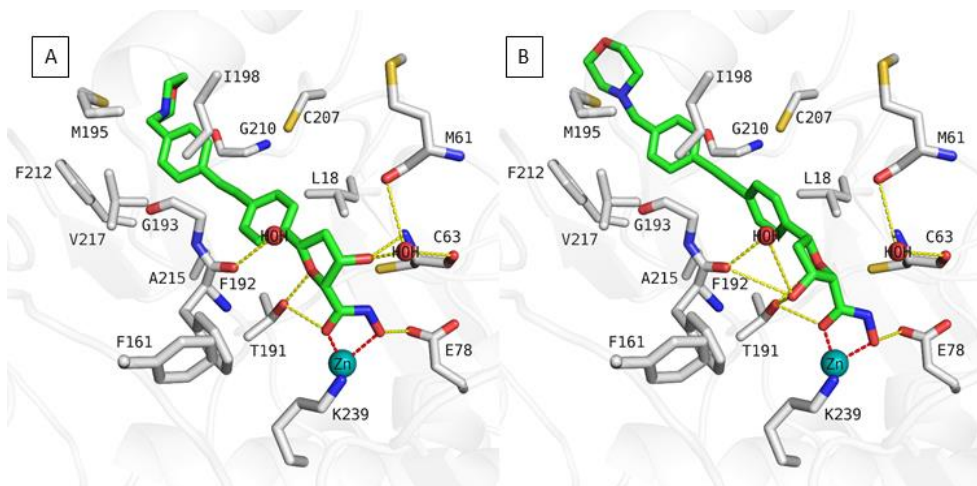
Figure 57. Docking poses of compound 115 and 116. A) Compound 115 and B) compound 116 in LpxC (PDB ID: 3PS3). Ligands are shown as green coloured sticks. Ribbons are shown as white colour. Relevant residues are shown in stick representation as white carbon atoms. The zinc ion is shown as cyan coloured sphere. The conserved water molecule is shown as red. Hydrogen bonds (yellow dashed lines), metal coordination (red dashed lines) between inhibitors and protein are shown.

In the third series of compounds (compound 117-120, scaffold D, Table 19), the open-chain analogues can adopt possible favourable interactions due to the flexibility of the diol linker group. This flexibility of the linker group caused the increase in the inhibitory activity in contrast to the rigid linker group. Compound 120, which is the most active compound in this series, shows direct interaction with C63, T191, and F192 through its hydroxyl groups and water-bridge interactions. These favourable interactions of compound 120 are probably the reason behind the increased LpxC inhibitory activity (Figure 58B). On the other hand, the less active compound 117 showed a similar interaction pattern as observed for compounds 112 and 114. One of the hydroxyl groups is directed toward L18, resulting in the reduced LpxC inhibitory activity (Figure 58A).

102
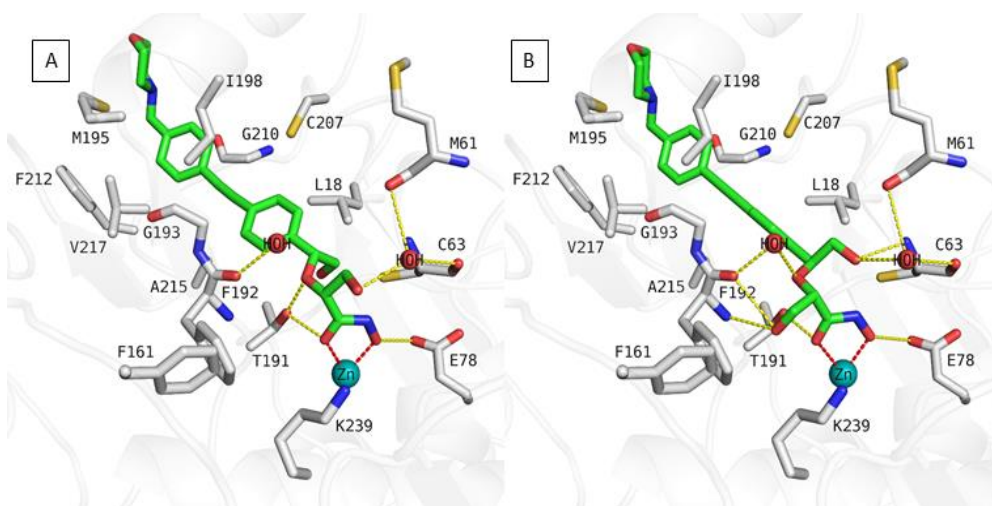
Figure 58. Docking poses of compound 117, and 120. A) Compound 117, and B) compound 120 in LpxC (PDB ID: 3PS3. Ligands are shown as green coloured sticks. Ribbons are shown as white colour. Relevant residues are shown in stick representation as white carbon atoms. The zinc ion is shown as cyan coloured sphere. The conserved water molecule is shown as red. Hydrogen bonds (yellow dashed lines), metal coordination (red dashed lines) between inhibitors and protein are shown.

In the fourth series of compounds (compound 121-131, scaffolds E, F and G, Table 19), the docking poses revealed that compounds bind to the binding pocket except for two inactive compounds 125 and 128, which possess a 4-(benzyloxy)phenyl group instead of a diphenylacetylene moiety. The benzyloxy cap group of compounds 125 and 128 could not fit into the hydrophobic tunnel, resulting in a loss of activity. The diphenylacetylene moieties of the compounds 121-131 (except compounds 125 and 128) pass through the hydrophobic tunnel consisting of L18, F192, M195, I198, A215, F212, and V217. The compounds bind the zinc ion in a bidentate fashion. In all cases, the side chains of E78 and T191 are engaged in hydrogen bond interactions with the hydroxyl and carbonyl groups of the hydroxamate moiety, respectively.

The (*S*)-configured compound 123 possessing a mono-substituted triazole ring, and its enantiomer compound 124 show similar binding modes (Figure 59A/B). The triazole ring is located in a small pocket consisting of F192 and K239. In the case of compound 123, the triazole ring is able to form an edge-to-face aromatic interaction with the side chain of F192. This interaction was not observed for compound 124 due to the less favourable orientation of the triazole ring. The other difference observed between 123 and 124 is the orientation of the C-O-

C linker. In the active compound 123, the oxygen atom is turned toward T191. In the inactive compound 124, the oxygen atom is directed toward the C63 residue. Additionally, the attachment of the phenyl ring to the 4th position of triazole in 123 and 124 leads to 126 and 127 (Figure 59C/D), respectively. Compound 126 showed a similar binding mode as observed for compound 123. Compound 126 exhibits additional cation-π interaction with K239. The interaction with K239 might explain the improvement in the activity of 126 compared to 123. The triazole ring of the inactive compound 127 is flipped, and aromatic interaction with F192 is lost, resulting in the loss of the inhibitory activity. The interaction with F192 seems crucial for the LpxC inhibitory activity. This interaction might also explain why compounds 123 and 126 have better activity than compound 121, which is the lead compound for this series.
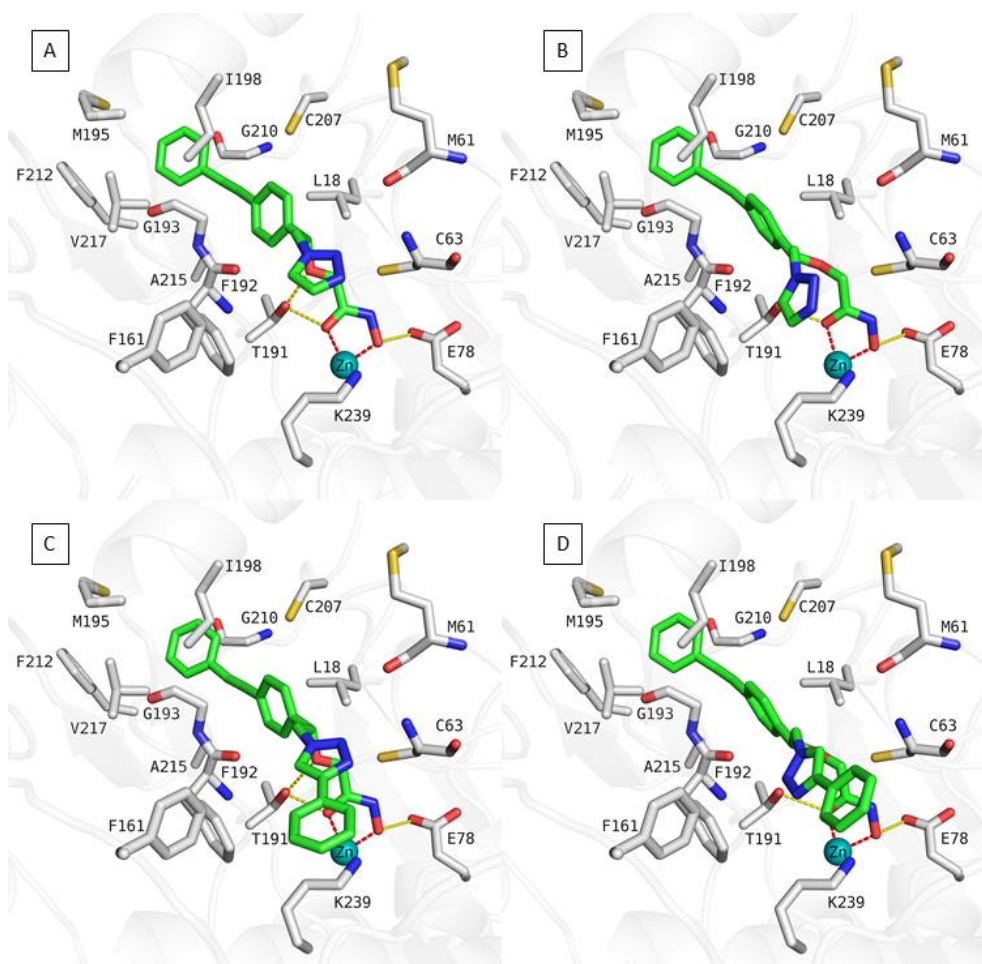
Figure 59. Docking poses of compound 123, 124, 126 and 127. A) Compound 123, B) compound 124, C) compound 126 and D) Compound 127 in LpxC (PDB ID: 3PS3). Ligands are shown as green coloured sticks. Ribbons are shown as white colour. Relevant residues are shown in stick

In the case of compound 129, the attachment of the phenyl ring to the 5th position of the triazole decreased the activity due to the loss of the F192 interaction. The triazole ring is directed toward C63 (Figure 60A). Compound 130 (Figure 60B), which is the most active compound in this series, showed a similar binding mode to the other active derivatives 123 and 125, which contain triazole rings. The methylhydroxy group attached to the 4th position of triazole in compound 130 is involved in a hydrogen bond interaction with K239. The shifted position of the methylhydroxy group from position 4 to 5 on the triazole ring prevents compound 131 from interaction with K239 (Figure 60C). However, the hydroxyl group builds hydrogen bond interactions with the backbone of M61 and the backbone of C63. These additional hydrogen bonds might compensate for the loss of interaction with K239.
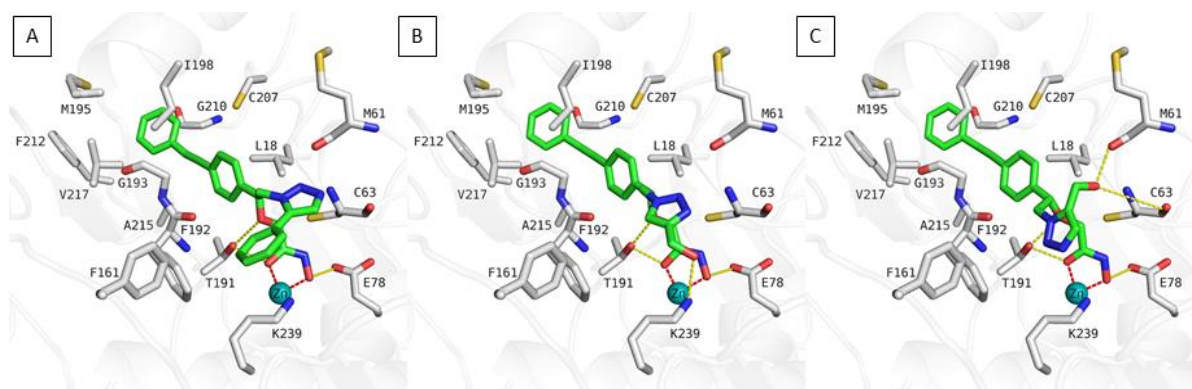
Figure 60. Docking poses of compound 129, 130 and 131. A) Compound 129, B) compound 130 and C) Compound 131 in LpxC (PDB ID: 3PS3). Ligands are shown as green coloured sticks. Ribbons are shown as white colour. Relevant residues are shown in stick representation as white carbon atoms. The zinc ion is shown as cyan coloured sphere. The conserved water molecule is shown as red. Hydrogen bonds (yellow dashed lines), metal coordination (red dashed lines) between inhibitors and protein are shown.

In the case of last series of compounds (132-141, scaffold H, I and J, Table 19), the compounds were inspired by previously reported compounds 132 and 133, which showed promising LpxC inhibitory activity. To gain further favorable interactions, the inhibitors were extended toward the UDP binding pocket (basic patch) by attaching benzyl ethers (scaffold I)

or (3,5-dimethylisoxazol-4-yl-methyl ethers (scaffold J). All the designed compounds in this series exhibited similar binding modes. The hydroxamic acid part showed bidentate chelation with zinc ion and hydrogen bond interaction with E78 and T191. The lipophilic distal part of the compounds is placed into the hydrophobic tunnel formed by L18, F192, M195, I198, A215, F212, and V217. The substituents attached to the β-carbon of the hydroxamic acid moiety directed towards the small pocket consisted of F161, F192, and K239.

Most active compounds of this series, (2S,3S)-configured compounds 134 and 138, showed similar docking poses (Figure 61A/B). The hydroxyl at position 3 is involved in a hydrogen bond with the F192. The benzyl and isoxazolylmethyl ether groups at position 3 are engaged in π-π interaction with the F161 and F192. The oxygen of the ether moiety shows hydrogen bond interactions with K239. The inversion of the configuration at position 3 of 134 and 138 leads to (2S, 3R)-configured derivatives 135 and 139 (Figure 61C/D). The hydroxyl groups at position 3 are directed out of the pocket and the solvent exposed. In addition, the benzyl ether and isoxazolylmethyl ether shifted away from K239 and lost their interaction with K239. The loss of the K239 interaction resulted in a significant decrease in the LpxC inhibitory activity.
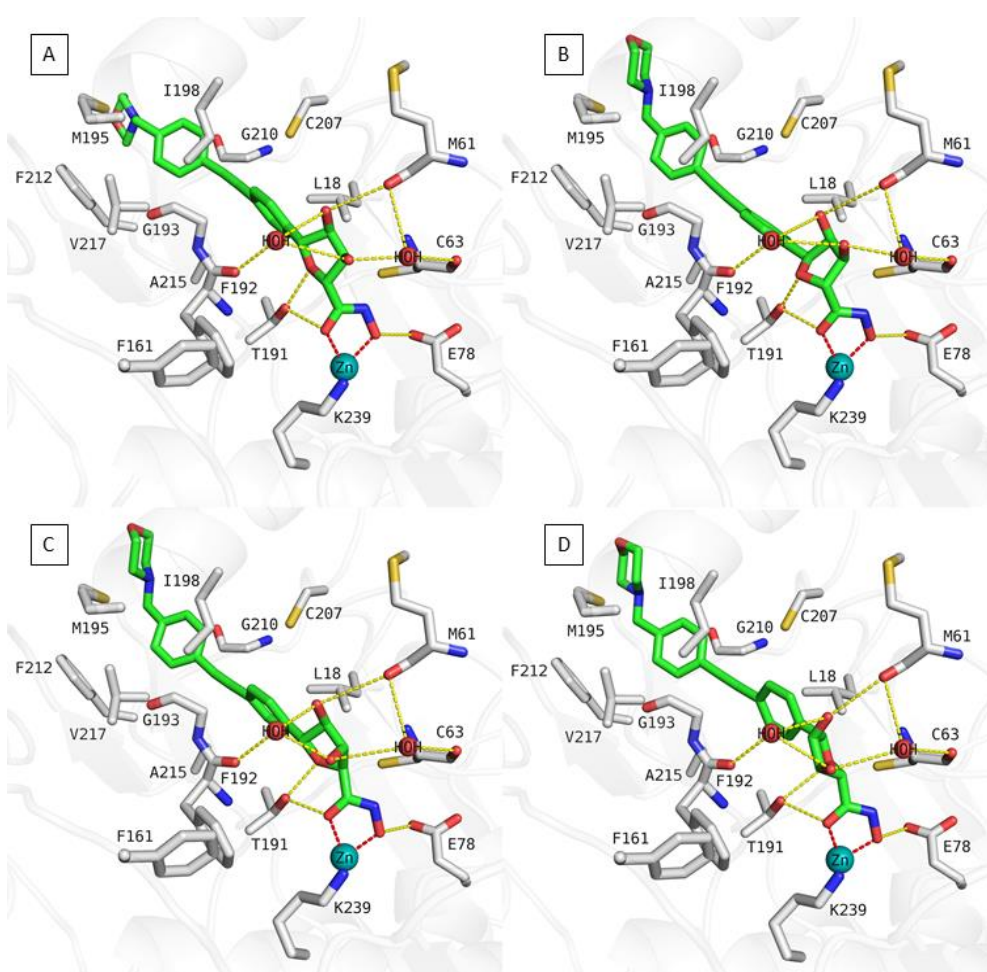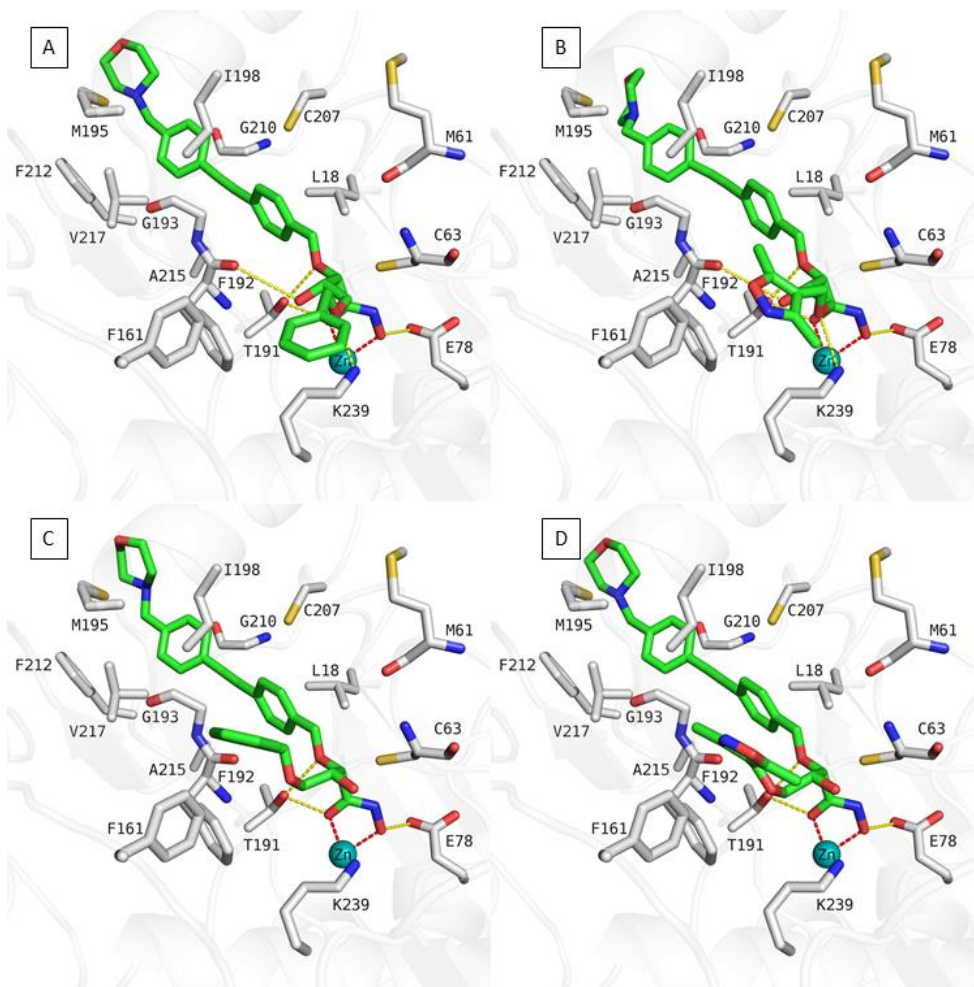
Figure 61. Docking poses of compound 134, 138, 135 and 139. A) Compound 134, B) compound 138, C) compound 135 and D) Compound 139 in LpxC (PDB ID: 3PS3). Ligands are shown as green coloured sticks. Ribbons are shown as white colour. Relevant residues are shown in stick representation as white carbon atoms. The zinc ion is shown as cyan coloured sphere. The conserved water molecule is shown as red. Hydrogen bonds (yellow dashed lines), metal coordination (red dashed lines) between inhibitors and protein are shown.

Analysis of the docking poses of (2R,3S)-configured compounds 136 and 140 (Figure 62A/B), which are enantiomers of compounds 135 and 139, revealed that the hydroxyl groups approach the F192 and exhibit hydrogen bond interaction with it, as observed for the active compounds 134 and 138. The benzylether moiety of compound 136 is engaged in a π-π interaction with the F161 and F192 and a hydrogen bond with K239. However, these interactions were not observed in the case of compound 140. This might explain the reduced activity of 140 compared to 136. In the case of the (2R,3R)-configured derivatives 137 and 141 (Figure 62C/D), the inversion of the hydroxyl group of compounds 136 and 140 resulted in the

107

interaction with C63. The interactions with F161, F192, and K239 were maintained in the case of compound 137 while compound 141 lost them. This is probably the reason for a significant decrease in the LpxC inhibitory activity.
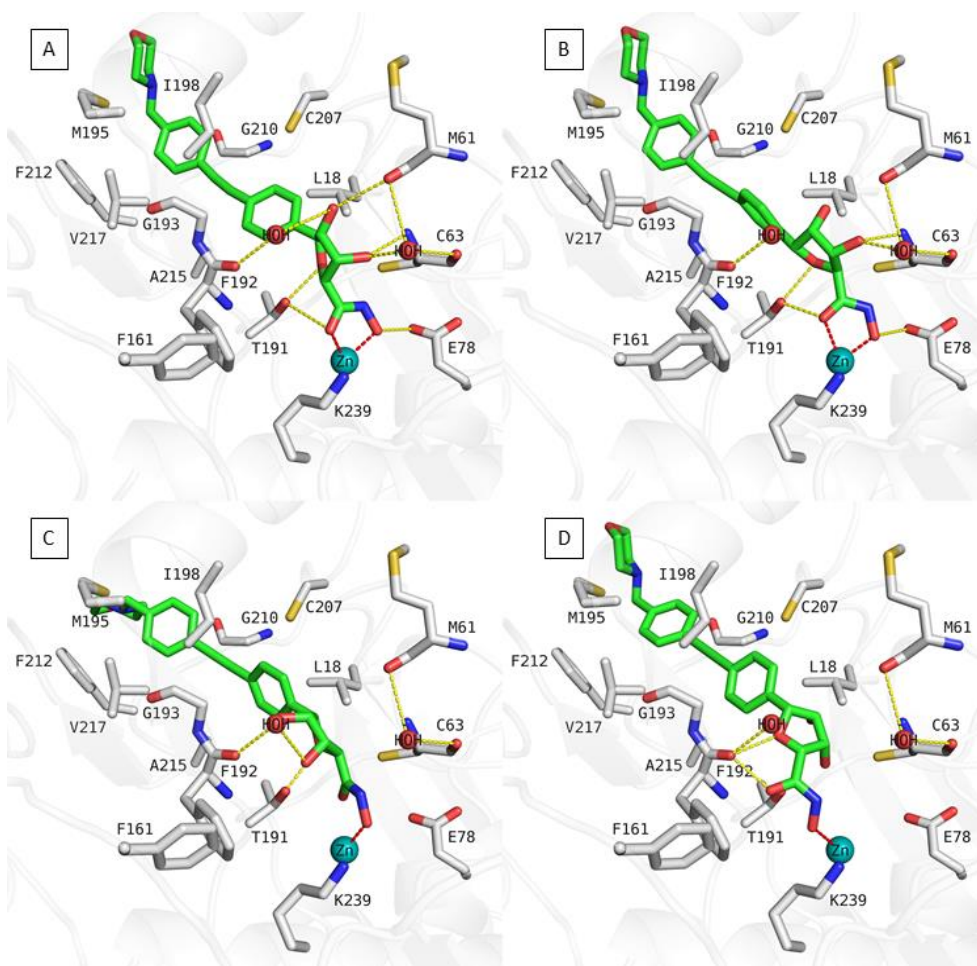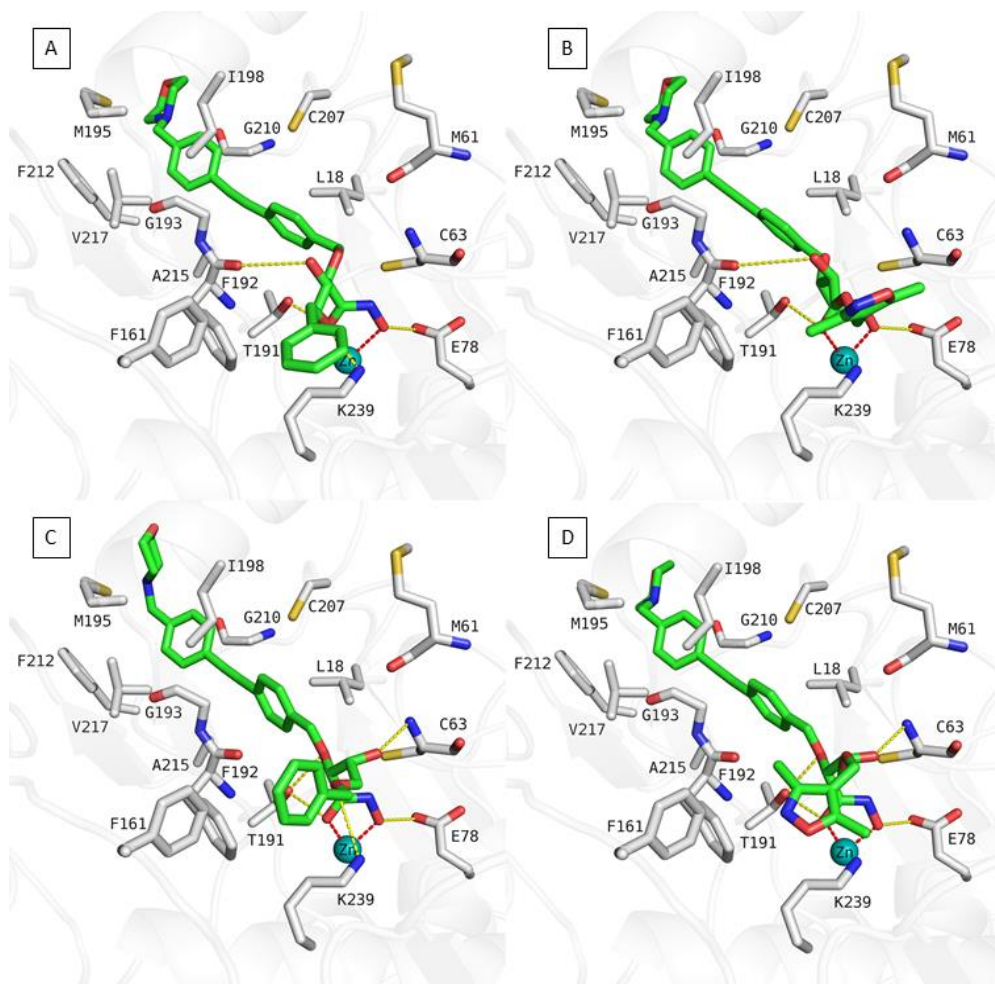

Figure 62. Docking poses of compound 136, 140, 137 and 141. A) Compound 136, B) compound 140, C) compound 137 and D) Compound 141 in LpxC (PDB ID: 3PS3). Ligands are shown as green coloured sticks. Ribbons are shown as white colour. Relevant residues are shown in stick representation as white carbon atoms. The zinc ion is shown as cyan coloured sphere. The conserved water molecule is shown as red. Hydrogen bonds (yellow dashed lines), metal coordination (red dashed lines) between inhibitors and protein are shown.

To summarize the docking results, four series of compounds (39 compounds) have been designed, synthesized, and their binding modes have been analyzed by computational methods. In the first series of compounds, it is observed that the position of the hydroxyl group on the C-glycoside moiety seems important for the activity. The hydroxyl groups of the active

compounds form water mediated hydrogen bond interactions with the amino acids. In contrast, when the hydroxyl groups were directed towards the inside of the pocket, the activity decreased. In the second series, the position of the hydroxyl on the tetrahydrofuran moiety was tested. The 3-hydroxyl group seems more favorable than the 4-hydroxyl group for the LpxC inhibitory activity due to the favorable hydrogen bond interactions with surrounding residues. In the third series, the flexible benzyloxyacetohydroxamic acid moiety instead of the rigid tetrahydrofuran ring was used to test the effect of conformational restriction on LpxC inhibitory activity. The flexible moiety led to an increase in the LpxC inhibitory activity. In the fourth series, compounds were extended by substitution of the tetrazole ring in order to make interactions with the UDP binding site where the fatty acyl chain of the natural substrate binds. At the UDP binding site, the compounds showing interactions with K239 exhibited high LpxC inhibitor activity. In the fifth series, the different aromatic substituents were tried to reach the UDP binding site and make aromatic interactions with the hydrophobic patch of active site. All of the compounds demonstrated high LpxC inhibitory activity. As a result, the interactions with the hydrophobic patch and the basic patch of the LpxC enzyme have a crucial role in LpxC inhibitory activity. Occupying these sites of the enzyme increases the LpxC inhibitory activity.

5. CONCLUSION

Drug discovery is a time-consuming, expensive, and challenging process. A drug discovery project aims to find potent and selective drug candidates with desired pharmacological and therapeutic effects. Bringing one single drug candidate to the market costs many years and billions of dollars. Computer-aided drug design (CADD) methods have emerged to reduce the time and cost of drug discovery projects. These methods can limit the use of unnecessary chemical products and eliminate the most likely inactive ones. The structure-based drug design (SBDD) technique is one of the CADD methods. It relies on known 3D structural information. Thus, the SBDD methods could provide critical knowledge to determine the crucial features of the target and ligand.

SBDD methods include molecular docking studies, molecular dynamics (MD) simulations, binding free energy (BFE) calculations, and virtual screening of large databases. Molecular docking studies predict the binding mode of the ligands. It helps to find out the crucial protein-ligand interactions. Then this information is used to design novel compounds. MD simulations give detailed information on the flexibility of the protein-ligand complexes. The atomic behavior and movement can be analyzed by MD simulations. Additionally, the stability of the predicted binding pose of the ligand can be investigated by using MD simulations. The BFE calculations are performed to rescore the predicted docking pose to find how well the ligand binds to the active pocket. Correct rescoring of the ligand poses plays a pivotal role in the establishment of predictive models. The generated models can predict the binding activities of the potential drug candidates. Based on this information, only the promising compounds can be synthesized.

In the present study, we mainly utilize SBDD methods to design and develop novel, potent and selective inhibitors against parasitic HDACs, human HDACs, and bacterial LpxC enzymes. We designed novel inhibitors and analyzed the obtained biological data using computer-based methods. This work discussed 39 compounds having hydroxamic acid warhead against parasitic *Trypanosoma cruzi* DAC2, 36 compounds possessing 2-aminobenzamide warhead against human class I HDACs, 26 compounds containing alkyl-hydrazide warhead against human class I HDACs and 39 hydroxamic acid derivatives against bacterial LpxC enzyme.

110

In the first part of the study, four series of compounds containing 39 hydroxamic acid derivatives were designed and analyzed. They were tested against the parasitic tcDAC2 protein, a possible target for the treatment of Chagas disease. The parasitic tcDAC2 enzyme shows a resemblance to the human class I HDACs. This part of the project aims to obtain potent and selective compounds for the tcDAC2 enzyme. The molecular docking studies were performed to understand the structure-activity relationship between the compounds and the target/off-target proteins. Based on the obtained structural information, the novel compounds aimed at the different parts of the active pocket were designed to achieve high activity as well as selectivity for tcDAC2 against human class I isoforms. The docking results showed that the π-π interaction with F267 in tcDAC2 increases the tcDAC2 inhibitory activity of the compounds as well as class I HDAC inhibitory activity. The compounds aiming to address the unique selectivity pocket of tcDAC2 resulted in reduced HDAC1 inhibitory activity but improved HDAC8 inhibitory activity. The compounds also lost activity on tcDAC2 due to solvent effects Therefore, the project should focus on aiming only at the tcDAC2 selectivity pocket with more suitable substituents, but not the unique HDAC8 selectivity pocket, in the future. The rigid groups attached to the linker group can be helpful in directing the ligand towards only the tcDAC2 selectivity pocket, not the HDAC8 selectivity pocket.

In the second part of the study, 36 novel 2-aminobenzamide derivatives were tested against human Class I HDACs, specifically HDAC1-3. Addressing the foot pocket region of the class I HDACs (HDAC1-3) resulted in selective HDAC1-3 inhibitors over other HDACs. However, the selectivity among the class I members remains challenging. To overcome that problem, we have optimized the linker and cap groups to investigate the impact of the different groups on selectivity. The fluoro group attached to the 4th position of 2-aminobenzamide showed favourable effects for HDAC3 selectivity over HDAC1-2. In addition, the attachment of the bulky groups (thiophene and phenyl) to the 5th position of 2-aminobenzamide resulted in selective HDAC1/2 inhibitory activity over HDAC3. The synthesized compounds were rescored using the BFE calculations. The predictive models based on BFE calculation were generated for each isoform. The predictive accuracy of the generated model was externally tested. The novel compounds were designed, synthesized, and tested by optimizing the several compounds in a previous step. The activity results of the external test set proved that the

predictive models based on BFE calculation could be used to design novel compounds. This method reduces the time and cost.

In the third part of the project, the 26 alkyl-hydrazide based compounds tested on class I HDACs were discussed. The alkylhydrazide warhead resulted in highly selective HDAC3 or selective HDAC8 inhibitory activity. The n-propyl side chain perfectly fills the foot pocket region of the HDAC3. The foot pockets of HDAC1 and HDAC2 are larger than in HDAC3. This shape difference between HDAC1/2 and HDAC3 resulted in selective HDAC3 inhibitory activity. The increase in the the side chain length caused an improvement in HDAC8 inhibitory activity over other HDACs. The structural analysis of HDAC3 and HDAC8 showed some crucial structural differences in their foot pocket region. We have utilized these structural differences to achieve selectivity among class I HDACs.

The last part of the project deals with 39 hydroxamic acid derivatives tested against the bacterial LpxC enzyme. In this part, the aim was to obtain the highly potent LpxC inhibitors. The stereoisomeric compounds were developed by optimizing the CHIR-090 reference compounds. Our studies showed that open-chain analogues show better LpxC inhibitory activity than the rigid tetrahydrofuran ring in the linker region. Additionally, the interactions with F161, F192, and K239 in the hydrophobic patch and basic patch of the LpxC enzyme play a crucial role in LpxC inhibitory activity.

To conclude, we have found that structure-based methods can be successfully used to design novel HDAC and LpxC inhibitors. The established QSAR models were able to predict the activity of the novel designed compounds. Based on the prediction results, the most promising compounds were synthesized. The structural optimization of the broad spectrum HDAC inhibitors resulted in isoform-selective compounds. Additionally, the compounds occupying the isoform-selective subpocket showed the isoform-selectivity among the highly similar enzymes. These validated protocols can be used for future projects related to zinc-dependent enzymes.

6. REFERENCES

1. Waddington, C.H., *The epigenotype. 1942.* Int J Epidemiol, 2012. **41**(1): p. 10-3.
2. Holliday, R., *The inheritance of epigenetic defects.* Science, 1987. **238**(4824): p. 163-70.
3. Felice, C., et al., *Review article: selective histone deacetylase isoforms as potential therapeutic targets in inflammatory bowel diseases.* Aliment Pharmacol Ther, 2015. **41**(1): p. 26-38.
4. Kouzarides, T., *Chromatin modifications and their function.* Cell, 2007. **128**(4): p. 693-705.
5. Cutter, A.R. and J.J. Hayes, *A brief review of nucleosome structure.* Febs Letters, 2015. **589**(20): p. 2914-2922.
6. Dymock, B.W., *The rise of epigenetic drug discovery.* Future Medicinal Chemistry, 2016. **8**(13): p. 1523-1524.
7. Claveria-Cabello, A., et al., *Epigenetics in Liver Fibrosis: Could HDACs be a Therapeutic Target?* Cells, 2020. **9**(10).
8. Mathias, R.A., A.J. Guise, and I.M. Cristea, *Post-translational modifications regulate class IIa histone deacetylase (HDAC) function in health and disease.* Mol Cell Proteomics, 2015. **14**(3): p. 456-70.
9. Keating, S.T., J. Plutzky, and A. El-Osta, *Epigenetic Changes in Diabetes and Cardiovascular Risk.* Circ Res, 2016. **118**(11): p. 1706-22.
10. Davey, C.A., et al., *Solvent Mediated Interactions in the Structure of the Nucleosome Core Particle at 1.9Å Resolution††We dedicate this paper to the memory of Max Perutz who was particularly inspirational and supportive to T.J.R. in the early stages of this study.* Journal of Molecular Biology, 2002. **319**(5): p. 1097-1113.
11. Allfrey, V.G., R. Faulkner, and A.E. Mirsky, *Acetylation and Methylation of Histones and Their Possible Role in the Regulation of Rna Synthesis.* Proc Natl Acad Sci U S A, 1964. **51**: p. 786-94.
12. Chen, P.J., et al., *Epigenetic modifications by histone deacetylases: Biological implications and therapeutic potential in liver fibrosis.* Biochimie, 2015. **116**: p. 61-9.
13. Eberharter, A. and P.B. Becker, *Histone acetylation: a switch between repressive and permissive chromatin. Second in review series on chromatin dynamics.* EMBO Rep, 2002. **3**(3): p. 224-9.
14. Park, S.Y. and J.S. Kim, *A short guide to histone deacetylases including recent progress on class II enzymes.* Exp Mol Med, 2020. **52**(2): p. 204-212.
15. Yang, X.J. and E. Seto, *The Rpd3/Hda1 family of lysine deacetylases: from bacteria and yeast to mice and men.* Nat Rev Mol Cell Biol, 2008. **9**(3): p. 206-18.
16. Shukla, S. and B.L. Tekwani, *Histone Deacetylases Inhibitors in Neurodegenerative Diseases, Neuroprotection and Neuronal Differentiation.* Front Pharmacol, 2020. **11**: p. 537.
17. Lehrman, G., et al., *Depletion of latent HIV-1 infection in vivo: a proof-of-concept study.* Lancet, 2005. **366**(9485): p. 549-55.
18. Kong, Y., et al., *Suppression of class I and II histone deacetylases blunts pressure-overload cardiac hypertrophy.* Circulation, 2006. **113**(22): p. 2579-88.

19. Reddy, P., et al., *Histone deacetylase inhibition modulates indoleamine 2,3-dioxygenase-dependent DC functions and regulates experimental graft-versus-host disease in mice.* J Clin Invest, 2008. **118**(7): p. 2562-73.

20. Haberland, M., et al., *Genetic dissection of histone deacetylase requirement in tumor cells.* Proc Natl Acad Sci U S A, 2009. **106**(19): p. 7751-5.

21. Haberland, M., R.L. Montgomery, and E.N. Olson, *The many roles of histone deacetylases in development and physiology: implications for disease and therapy.* Nat Rev Genet, 2009. **10**(1): p. 32-42.

22. Tang, J., H. Yan, and S. Zhuang, *Histone deacetylases as targets for treatment of multiple diseases.* Clin Sci (Lond), 2013. **124**(11): p. 651-62.

23. Melesina, J., et al., *Strategies To Design Selective Histone Deacetylase Inhibitors.* ChemMedChem, 2021. **16**(9): p. 1336-1359.

24. Watson, P.J., et al., *Structure of HDAC3 bound to co-repressor and inositol tetraphosphate.* Nature, 2012. **481**(7381): p. 335-40.

25. Millard, C.J., et al., *Class I HDACs share a common mechanism of regulation by inositol phosphates.* Mol Cell, 2013. **51**(1): p. 57-67.

26. Xue, Y., et al., *NURD, a novel complex with both ATP-dependent chromatin-remodeling and histone deacetylase activities.* Mol Cell, 1998. **2**(6): p. 851-61.

27. Laherty, C.D., et al., *Histone deacetylases associated with the mSin3 corepressor mediate mad transcriptional repression.* Cell, 1997. **89**(3): p. 349-56.

28. Humphrey, G.W., et al., *Stable histone deacetylase complexes distinguished by the presence of SANT domain proteins CoREST/kiaa0071 and Mta-L1.* J Biol Chem, 2001. **276**(9): p. 6817-24.

29. Turnbull, R.E., et al., *The MiDAC histone deacetylase complex is essential for embryonic development and has a unique multivalent structure.* Nat Commun, 2020. **11**(1): p. 3252.

30. Guenther, M.G., et al., *A core SMRT corepressor complex containing HDAC3 and TBL1, a WD40-repeat protein linked to deafness.* Genes Dev, 2000. **14**(9): p. 1048-57.

31. Wen, Y.D., et al., *The histone deacetylase-3 complex contains nuclear receptor corepressors.* Proc Natl Acad Sci U S A, 2000. **97**(13): p. 7202-7.

32. Hu, E., et al., *Cloning and characterization of a novel human class I histone deacetylase that functions as a transcription repressor.* J Biol Chem, 2000. **275**(20): p. 15254-64.

33. Lee, H., N. Rezai-Zadeh, and E. Seto, *Negative regulation of histone deacetylase 8 activity by cyclic AMP-dependent protein kinase A.* Mol Cell Biol, 2004. **24**(2): p. 765-73.

34. Clocchiatti, A., C. Florean, and C. Brancolini, *Class IIa HDACs: from important roles in differentiation to possible implications in tumourigenesis.* J Cell Mol Med, 2011. **15**(9): p. 1833-46.

35. Hudson, G.M., et al., *Insights into the Recruitment of Class IIa Histone Deacetylases (HDACs) to the SMRT/NCoR Transcriptional Repression Complex.* J Biol Chem, 2015. **290**(29): p. 18237-18244.

36. Kutil, Z., et al., *The unraveling of substrate specificity of histone deacetylase 6 domains using acetylome peptide microarrays and peptide libraries.* FASEB J, 2019. **33**(3): p. 4035-4045.

37. Hai, Y., et al., *Histone deacetylase 10 structure and molecular function as a polyamine deacetylase.* Nat Commun, 2017. **8**: p. 15368.

38.	de Ruijter, A.J., et al., *Histone deacetylases (HDACs): characterization of the classical HDAC family.* Biochem J, 2003. **370**(Pt 3): p. 737-49.

39.	Gao, L., et al., *Cloning and functional characterization of HDAC11, a novel member of the human histone deacetylase family.* J Biol Chem, 2002. **277**(28): p. 25748-55.

40.	Yoshida, M., et al., *Chemical and structural biology of protein lysine deacetylases.* Proc Jpn Acad Ser B Phys Biol Sci, 2017. **93**(5): p. 297-321.

41.	Lagger, G., et al., *Essential function of histone deacetylase 1 in proliferation control and CDK inhibitor repression.* EMBO J, 2002. **21**(11): p. 2672-81.

42.	Montgomery, R.L., et al., *Maintenance of cardiac energy metabolism by histone deacetylase 3 in mice.* J Clin Invest, 2008. **118**(11): p. 3588-97.

43.	Montgomery, R.L., et al., *Histone deacetylases 1 and 2 redundantly regulate cardiac morphogenesis, growth, and contractility.* Genes Dev, 2007. **21**(14): p. 1790-802.

44.	Haberland, M., et al., *Epigenetic control of skull morphogenesis by histone deacetylase 8.* Genes Dev, 2009. **23**(14): p. 1625-30.

45.	Chang, S., et al., *Histone deacetylases 5 and 9 govern responsiveness of the heart to a subset of stress signals and play redundant roles in heart development.* Mol Cell Biol, 2004. **24**(19): p. 8467-76.

46.	Chang, S., et al., *Histone deacetylase 7 maintains vascular integrity by repressing matrix metalloproteinase 10.* Cell, 2006. **126**(2): p. 321-34.

47.	Vega, R.B., et al., *Histone deacetylase 4 controls chondrocyte hypertrophy during skeletogenesis.* Cell, 2004. **119**(4): p. 555-66.

48.	Zhang, Y., et al., *Mice lacking histone deacetylase 6 have hyperacetylated tubulin but are viable and develop normally.* Mol Cell Biol, 2008. **28**(5): p. 1688-701.

49.	Finnin, M.S., et al., *Structures of a histone deacetylase homologue bound to the TSA and SAHA inhibitors.* Nature, 1999. **401**(6749): p. 188-93.

50.	Vanommeslaeghe, K., et al., *Theoretical study revealing the functioning of a novel combination of catalytic motifs in histone deacetylase.* Bioorg Med Chem, 2005. **13**(12): p. 3987-92.

51.	Corminboeuf, C., et al., *Unexpected deacetylation mechanism suggested by a density functional theory QM/MM study of histone-deacetylase-like protein.* J Am Chem Soc, 2006. **128**(14): p. 4530-1.

52.	Gantt, S.M., et al., *General Base-General Acid Catalysis in Human Histone Deacetylase 8.* Biochemistry, 2016. **55**(5): p. 820-32.

53.	Berman, H.M., et al., *The Protein Data Bank.* Nucleic Acids Res, 2000. **28**(1): p. 235-42.

54.	Ho, T.C.S., A.H.Y. Chan, and A. Ganesan, *Thirty Years of HDAC Inhibitors: 2020 Insight and Hindsight.* J Med Chem, 2020. **63**(21): p. 12460-12484.

55.	Lauffer, B.E., et al., *Histone deacetylase (HDAC) inhibitor kinetic rate constants correlate with cellular histone acetylation but not transcription and cell viability.* J Biol Chem, 2013. **288**(37): p. 26926-43.

56.	Wang, D.F., et al., *On the function of the 14 A long internal cavity of histone deacetylase-like protein: implications for the design of histone deacetylase inhibitors.* J Med Chem, 2004. **47**(13): p. 3409-17.

57.	Hotez, P.J., et al., *The global burden of disease study 2010: interpretation and implications for the neglected tropical diseases.* PLoS Negl Trop Dis, 2014. **8**(7): p. e2865.

58.   Organization, W.H. *Chagas disease (also known as American trypanosomiasis.* 2022 [cited 2022 12 April].

59.   Schmunis, G.A. and Z.E. Yadon, *Chagas disease: A Latin American health problem becoming a world health problem.* Acta Tropica, 2010. **115**(1-2): p. 14-21.

60.   Schofield, C.J., J. Jannin, and R. Salvatella, *The future of Chagas disease control.* Trends in Parasitology, 2006. **22**(12): p. 583-588.

61.   Perez-Molina, J.A. and I. Molina, *Chagas disease.* Lancet, 2018. **391**(10115): p. 82-94.

62.   Hailu, G.S., et al., *Lysine Deacetylase Inhibitors in Parasites: Past, Present, and Future Perspectives.* Journal of Medicinal Chemistry, 2017. **60**(12): p. 4780-4804.

63.   Scholte, L.L.S., et al., *Evolutionary relationships among protein lysine deacetylases of parasites causing neglected diseases.* Infection Genetics and Evolution, 2017. **53**: p. 175-188.

64.   Marek, M., et al., *Species-selective targeting of pathogens revealed by the atypical structure and active site of Trypanosoma cruzi histone deacetylase DAC2.* Cell Reports, 2021. **37**(12).

65.   Falagas, M.E., et al., *Outcome of infections due to pandrug-resistant (PDR) Gram-negative bacteria.* BMC Infect Dis, 2005. **5**: p. 24.

66.   Wright, G.D., *Molecular mechanisms of antibiotic resistance.* Chem Commun (Camb), 2011. **47**(14): p. 4055-61.

67.   Onishi, H.R., et al., *Antibacterial agents that inhibit lipid A biosynthesis.* Science, 1996. **274**(5289): p. 980-2.

68.   Raetz, C.R. and C. Whitfield, *Lipopolysaccharide endotoxins.* Annu Rev Biochem, 2002. **71**: p. 635-700.

69.   Barb, A.W. and P. Zhou, *Mechanism and inhibition of LpxC: an essential zinc-dependent deacetylase of bacterial lipid A synthesis.* Curr Pharm Biotechnol, 2008. **9**(1): p. 9-15.

70.   Sorensen, P.G., et al., *Regulation of UDP-3-O-[R-3-hydroxymyristoyl]-N-acetylglucosamine deacetylase in Escherichia coli. The second enzymatic step of lipid a biosynthesis.* J Biol Chem, 1996. **271**(42): p. 25898-905.

71.   Lee, C.J., et al., *Species-specific and inhibitor-dependent conformations of LpxC: implications for antibiotic design.* Chem Biol, 2011. **18**(1): p. 38-47.

72.   Liang, X., et al., *Syntheses, structures and antibiotic activities of LpxC inhibitors based on the diacetylene scaffold.* Bioorg Med Chem, 2011. **19**(2): p. 852-60.

73.   Liang, X., et al., *Synthesis, structure, and antibiotic activity of aryl-substituted LpxC inhibitors.* J Med Chem, 2013. **56**(17): p. 6954-6966.

74.   Cole, K.E., et al., *Structure of the metal-dependent deacetylase LpxC from Yersinia enterocolitica complexed with the potent inhibitor CHIR-090.* Biochemistry, 2011. **50**(2): p. 258-65.

75.   Hernick, M., et al., *Activation of Escherichia coli UDP-3-O-[(R)-3-hydroxymyristoyl]-N-acetylglucosamine deacetylase by Fe2+ yields a more efficient enzyme with altered ligand affinity.* Biochemistry, 2010. **49**(10): p. 2246-55.

76.   Hernick, M., et al., *UDP-3-O-((R)-3-hydroxymyristoyl)-N-acetylglucosamine deacetylase functions through a general acid-base catalyst pair mechanism.* J Biol Chem, 2005. **280**(17): p. 16969-78.

77.   Duvic, M., et al., *Phase 2 trial of oral vorinostat (suberoylanilide hydroxamic acid, SAHA) for refractory cutaneous T-cell lymphoma (CTCL).* Blood, 2007. **109**(1): p. 31-9.

78. Li, Y., et al., *A New Strategy to Target Acute Myeloid Leukemia Stem and Progenitor Cells Using Chidamide, a Histone Deacetylase Inhibitor.* Current Cancer Drug Targets, 2015. **15**(6): p. 493-503.

79. Libby, E.N., et al., *Panobinostat: a review of trial results and future prospects in multiple myeloma.* Expert Review of Hematology, 2015. **8**(1): p. 9-18.

80. Molife, L.R. and J.S. de Bono, *Belinostat: clinical applications in solid tumors and lymphoma.* Expert Opinion on Investigational Drugs, 2011. **20**(12): p. 1723-1732.

81. Piekarz, R.L., et al., *Phase II multi-institutional trial of the histone deacetylase inhibitor romidepsin as monotherapy for patients with cutaneous T-cell lymphoma.* J Clin Oncol, 2009. **27**(32): p. 5410-7.

82. Atadja, P., *Development of the pan-DAC inhibitor panobinostat (LBH589): successes and challenges.* Cancer Lett, 2009. **280**(2): p. 233-41.

83. Ning, Z.Q., et al., *Chidamide (CS055/HBI-8000): a new histone deacetylase inhibitor of the benzamide class with antitumor activity and the ability to enhance immune cell-mediated tumor cell cytotoxicity.* Cancer Chemother Pharmacol, 2012. **69**(4): p. 901-9.

84. Ito, T., et al., *Significant growth suppression of synovial sarcomas by the histone deacetylase inhibitor FK228 in vitro and in vivo.* Cancer Lett, 2005. **224**(2): p. 311-9.

85. Mann, B.S., et al., *FDA approval summary: vorinostat for treatment of advanced primary cutaneous T-cell lymphoma.* Oncologist, 2007. **12**(10): p. 1247-52.

86. Marks, P.A. and W.S. Xu, *Histone deacetylase inhibitors: Potential in cancer therapy.* J Cell Biochem, 2009. **107**(4): p. 600-8.

87. Poole, R.M., *Belinostat: first global approval.* Drugs, 2014. **74**(13): p. 1543-54.

88. Cashen, A., et al., *Phase II study of the histone deacetylase inhibitor belinostat (PXD101) for the treatment of myelodysplastic syndrome (MDS).* Ann Hematol, 2012. **91**(1): p. 33-8.

89. Oki, Y., et al., *Phase I study of panobinostat plus everolimus in patients with relapsed or refractory lymphoma.* Clin Cancer Res, 2013. **19**(24): p. 6882-90.

90. Lu, X., et al., *Development of chidamide for peripheral T-cell lymphoma, the first orphan drug approved in China.* Intractable Rare Dis Res, 2016. **5**(3): p. 185-91.

91. Whittaker, S.J., et al., *Final results from a multicenter, international, pivotal study of romidepsin in refractory cutaneous T-cell lymphoma.* J Clin Oncol, 2010. **28**(29): p. 4485-91.

92. Micelli, C. and G. Rastelli, *Histone deacetylases: structural determinants of inhibitor selectivity.* Drug Discov Today, 2015. **20**(6): p. 718-35.

93. Melesina, J., et al., *Homology modeling of parasite histone deacetylases to guide the structure-based design of selective inhibitors.* J Mol Graph Model, 2015. **62**: p. 342-361.

94. Jung, M., et al., *Amide analogues of trichostatin A as inhibitors of histone deacetylase and inducers of terminal cell differentiation.* Journal of Medicinal Chemistry, 1999. **42**(22): p. 4669-4679.

95. Jung, M., et al., *Analogues of trichostatin A and trapoxin B as histone deacetylase inhibitors.* Bioorganic & Medicinal Chemistry Letters, 1997. **7**(13): p. 1655-1658.

96. Balasubramanian, S., E. Verner, and J.J. Buggy, *Isoform-specific histone deacetylase inhibitors: the next step?* Cancer Lett, 2009. **280**(2): p. 211-21.

97. Cole, K.E., et al., *Structural basis of the antiproliferative activity of largazole, a depsipeptide inhibitor of the histone deacetylases.* J Am Chem Soc, 2011. **133**(32): p. 12474-7.

98.   Fournier, J.F., et al., *Squaramides as novel class I and IIB histone deacetylase inhibitors for topical treatment of cutaneous t-cell lymphoma.* Bioorg Med Chem Lett, 2018. **28**(17): p. 2985-2992.

99.   Hai, Y. and D.W. Christianson, *Histone deacetylase 6 structure and molecular basis of catalysis and inhibition.* Nat Chem Biol, 2016. **12**(9): p. 741-7.

100.   Liu, J., et al., *Selective Class I HDAC Inhibitors Based on Aryl Ketone Zinc Binding Induce HIV-1 Protein for Clearance.* ACS Med Chem Lett, 2020. **11**(7): p. 1476-1483.

101.   Liu, J., et al., *Discovery of Highly Selective and Potent HDAC3 Inhibitors Based on a 2-Substituted Benzamide Zinc Binding Group.* ACS Med Chem Lett, 2020. **11**(12): p. 2476-2483.

102.   Simoben, C.V., et al., *A Novel Class of Schistosoma mansoni Histone Deacetylase 8 (HDAC8) Inhibitors Identified by Structure-Based Virtual Screening and In Vitro Testing.* Molecules, 2018. **23**(3).

103.   Somoza, J.R., et al., *Structural snapshots of human HDAC8 provide insights into the class I histone deacetylases.* Structure, 2004. **12**(7): p. 1325-34.

104.   Vannini, A., et al., *Substrate binding to histone deacetylases as shown by the crystal structure of the HDAC8-substrate complex.* EMBO Rep, 2007. **8**(9): p. 879-84.

105.   Whitehead, L., et al., *Human HDAC isoform selectivity achieved via exploitation of the acetate release channel with structurally unique small molecule inhibitors.* Bioorg Med Chem, 2011. **19**(15): p. 4626-34.

106.   Yu, W., et al., *Discovery of ethyl ketone-based HDACs 1, 2, and 3 selective inhibitors for HIV latency reactivation.* Bioorg Med Chem Lett, 2020. **30**(13): p. 127197.

107.   Yadav, R., P. Mishra, and D. Yadav, *Histone Deacetylase Inhibitors: A Prospect in Drug Discovery.* Turk J Pharm Sci, 2019. **16**(1): p. 101-114.

108.   Perrin, J., et al., *Identifying drug targets in tissues and whole blood with thermal-shift profiling.* Nat Biotechnol, 2020. **38**(3): p. 303-308.

109.   Becher, I., et al., *Thermal profiling reveals phenylalanine hydroxylase as an off-target of panobinostat.* Nat Chem Biol, 2016. **12**(11): p. 908-910.

110.   McClure, J.J., et al., *Development of Allosteric Hydrazide-Containing Class I Histone Deacetylase Inhibitors for Use in Acute Myeloid Leukemia.* Journal of Medicinal Chemistry, 2016. **59**(21): p. 9942-9959.

111.   Li, X., et al., *Class I HDAC Inhibitors Display Different Antitumor Mechanism in Leukemia and Prostatic Cancer Cells Depending on Their p53 Status.* J Med Chem, 2018. **61**(6): p. 2589-2603.

112.   Kozlov, M.V., et al., *Synthesis of N'-propylhydrazide analogs of hydroxamic inhibitors of histone deacetylases (HDACs) and evaluation of their impact on activities of HDACs and replication of hepatitis C virus (HCV).* Bioorg Med Chem Lett, 2019. **29**(16): p. 2369-2374.

113.   Li, X., et al., *Design of Hydrazide-Bearing HDACIs Based on Panobinostat and Their p53 and FLT3-ITD Dependency in Antileukemia Activity.* J Med Chem, 2020. **63**(10): p. 5501-5525.

114.   Ibrahim, H.S., et al., *Synthesis, Molecular Docking and Biological Characterization of Pyrazine Linked 2-Aminobenzamides as New Class I Selective Histone Deacetylase (HDAC) Inhibitors with Anti-Leukemic Activity.* Int J Mol Sci, 2021. **23**(1).

115.   Wang, Y.F., et al., *Identification of Histone Deacetylase Inhibitors with Benzoylhydrazide Scaffold that Selectively Inhibit Class I Histone Deacetylases.* Chemistry & Biology, 2015. **22**(2): p. 273-284.

116.	Heimburg, T., et al., *Structure-Based Design and Synthesis of Novel Inhibitors Targeting HDAC8 from Schistosoma mansoni for the Treatment of Schistosomiasis.* J Med Chem, 2016. **59**(6): p. 2423-35.

117.	Heimburg, T., et al., *Structure-Based Design and Biological Characterization of Selective Histone Deacetylase 8 (HDAC8) Inhibitors with Anti-Neuroblastoma Activity.* J Med Chem, 2017. **60**(24): p. 10188-10204.

118.	Marek, M., et al., *Characterization of Histone Deacetylase 8 (HDAC8) Selective Inhibition Reveals Specific Active Site Structural and Functional Determinants.* Journal of Medicinal Chemistry, 2018. **61**(22): p. 10000-10016.

119.	Burli, R.W., et al., *Design, synthesis, and biological evaluation of potent and selective class IIa histone deacetylase (HDAC) inhibitors as a potential therapy for Huntington's disease.* J Med Chem, 2013. **56**(24): p. 9934-54.

120.	Jackman, J.E., et al., *Antibacterial agents that target lipid A biosynthesis in gram-negative bacteria. Inhibition of diverse UDP-3-O-(r-3-hydroxymyristoyl)-n-acetylglucosamine deacetylases by substrate analogs containing zinc binding motifs.* J Biol Chem, 2000. **275**(15): p. 11002-9.

121.	McClerren, A.L., et al., *A slow, tight-binding inhibitor of the zinc-dependent deacetylase LpxC of lipid A biosynthesis with antibiotic activity comparable to ciprofloxacin.* Biochemistry, 2005. **44**(50): p. 16574-83.

122.	Sabe, V.T., et al., *Current trends in computer aided drug design and a highlight of drugs discovered via computational techniques: A review.* Eur J Med Chem, 2021. **224**: p. 113705.

123.	Meng, X.Y., et al., *Molecular docking: a powerful approach for structure-based drug discovery.* Curr Comput Aided Drug Des, 2011. **7**(2): p. 146-57.

124.	Saikia, S. and M. Bordoloi, *Molecular Docking: Challenges, Advances and its Use in Drug Discovery Perspective.* Current Drug Targets, 2019. **20**(5): p. 501-521.

125.	Kitchen, D.B., et al., *Docking and scoring in virtual screening for drug discovery: methods and applications.* Nat Rev Drug Discov, 2004. **3**(11): p. 935-49.

126.	Pagadala, N.S., K. Syed, and J. Tuszynski, *Software for molecular docking: a review.* Biophys Rev, 2017. **9**(2): p. 91-102.

127.	Harder, E., et al., *OPLS3: A Force Field Providing Broad Coverage of Drug-like Small Molecules and Proteins.* J Chem Theory Comput, 2016. **12**(1): p. 281-96.

128.	*Schrödinger Release 2019-1: Maestro, Protein Preparation Wizard, prime, Epik, Ligprep, Confgen, Glide.* 2019, Schrödinger LLC: New York, NY (USA).

129.	*Molecular operating Environment (MOE), 2019.01.* 2019, Chemical Computing Group (CCG): 1010 Sherbooke St. West, Suite 910, Montreal, QC, Canada, H3A 2R7.

130.	Hollingsworth, S.A. and R.O. Dror, *Molecular Dynamics Simulation for All.* Neuron, 2018. **99**(6): p. 1129-1143.

131.	D.A. Case, R.M.B., D.S. Cerutti, T.E. Cheatham, III, T.A. Darden, R.E. Duke, T.J. Giese, H. Gohlke, A.W. Goetz, N. Homeyer, S. Izadi, P. Janowski, J. Kaus, A. Kovalenko, T.S. Lee, S. LeGrand, P. Li, C. Lin, T. Luchko, R. Luo, B. Madej, D. Mermelstein, K.M. Merz, G. Monard, H. Nguyen, H.T. Nguyen, I. Omelyan, A. Onufriev, D.R. Roe, A. Roitberg, C. Sagui, C.L. Simmerling, W.M. Botello-Smith, J. Swails, R.C. Walker, J. Wang, R.M. Wolf, X. Wu, L. Xiao and P.A. Kollman, *AMBER2016, University of Claiforni, San Francisco.* 2016.

132.	Jakalian, A., et al., *Fast, efficient generation of high-quality atomic charges. AM1-BCC model: I. Method.* J Comput Chem, 2000. **21**: p. 132-146.

133. Jakalian, A., D.B. Jack, and C.I. Bayly, *Fast, efficient generation of high-quality atomic charges. AM1-BCC model: II. Parameterization and validation.* J Comput Chem, 2002. **23**(16): p. 1623-41.

134. Duan, Y., et al., *A point-charge force field for molecular mechanics simulations of proteins based on condensed-phase quantum mechanical calculations.* J Comput Chem, 2003. **24**(16): p. 1999-2012.

135. Lee, M.C. and Y. Duan, *Distinguish protein decoys by using a scoring function based on a new AMBER force field, short molecular dynamics simulations, and the generalized born solvent model.* Proteins, 2004. **55**(3): p. 620-34.

136. Li, P., L.F. Song, and K.M. Merz, Jr., *Parameterization of highly charged metal ions using the 12-6-4 LJ-type nonbonded model in explicit water.* J Phys Chem B, 2015. **119**(3): p. 883-95.

137. Wang, J., et al., *Development and testing of a general amber force field.* J Comput Chem, 2004. **25**(9): p. 1157-74.

138. Jean-Paul Ryckaert, G.C., Herman J. C. Berendsen, *Numerical integration of the cartesan equations of motion of a system with constraints: molecular dynamics of n-alkanes.* Journal of Computational Physics, 1977. **23**(3): p. 327-341.

139. Pastor, R.W., B.R. Brooks, and A. Szabo, *An analysis of the accuracy of Langevin and molecular dynamics algorithms.* Molecular Physics, 1988. **65**(6): p. 1409-1419.

140. Heinzelmann, G. and M.K. Gilson, *Automation of absolute protein-ligand binding free energy calculations for docking refinement and compound evaluation.* Sci Rep, 2021. **11**(1): p. 1116.

141. Zwanzig, R.W., *High-Temperature Equation of State by a Perturbation Method .1. Nonpolar Gases.* Journal of Chemical Physics, 1954. **22**(8): p. 1420-1426.

142. Straatsma, T.P. and H.J.C. Berendsen, *Free-Energy of Ionic Hydration - Analysis of a Thermodynamic Integration Technique to Evaluate Free-Energy Differences by Molecular-Dynamics Simulations.* Journal of Chemical Physics, 1988. **89**(9): p. 5876-5886.

143. Straatsma, T.P., H.J.C. Berendsen, and J.P.M. Postma, *Free-Energy of Hydrophobic Hydration - a Molecular-Dynamics Study of Noble-Gases in Water.* Journal of Chemical Physics, 1986. **85**(11): p. 6720-6727.

144. Bhati, A.P., et al., *Rapid, Accurate, Precise, and Reliable Relative Free Energy Prediction Using Ensemble Based Thermodynamic Integration.* J Chem Theory Comput, 2017. **13**(1): p. 210-222.

145. Fratev, F. and S. Sirimulla, *An Improved Free Energy Perturbation FEP+ Sampling Protocol for Flexible Ligand-Binding Domains.* Sci Rep, 2019. **9**(1): p. 16829.

146. Srinivasan, J., et al., *Continuum solvent studies of the stability of RNA hairpin loops and helices.* Journal of Biomolecular Structure & Dynamics, 1998. **16**(3): p. 671-+.

147. Kollman, P.A., et al., *Calculating structures and free energies of complex molecules: Combining molecular mechanics and continuum models.* Accounts of Chemical Research, 2000. **33**(12): p. 889-897.

148. Hansson, T., J. Marelius, and J. Aqvist, *Ligand binding affinity prediction by linear interaction energy methods.* J Comput Aided Mol Des, 1998. **12**(1): p. 27-35.

149. Aqvist, J., C. Medina, and J.E. Samuelsson, *A new method for predicting binding affinity in computer-aided drug design.* Protein Eng, 1994. **7**(3): p. 385-91.

150. Wichapong, K., et al., *Application of Docking and QM/MM-GBSA Rescoring to Screen for Novel Myt1 Kinase Inhibitors.* Journal of Chemical Information and Modeling, 2014. **54**(3): p. 881-893.

151. Slynko, I., et al., *Identification of Highly Potent Protein Kinase C-Related Kinase 1 Inhibitors by Virtual Screening, Binding Free Energy Rescoring, and in vitro Testing.* ChemMedChem, 2016. **11**(18): p. 2084-94.

152. Simoben, C.V., et al., *Binding Free Energy (BFE) Calculations and Quantitative Structure-Activity Relationship (QSAR) Analysis of Schistosoma mansoni Histone Deacetylase 8 (smHDAC8) Inhibitors.* Molecules, 2021. **26**(9).

153. Karaman, B. and W. Sippl, *Docking and binding free energy calculations of sirtuin inhibitors.* Eur J Med Chem, 2015. **93**: p. 584-98.

154. Bulbul, E.F., et al., *Docking, Binding Free Energy Calculations and In Vitro Characterization of Pyrazine Linked 2-Aminobenzamides as Novel Class I Histone Deacetylase (HDAC) Inhibitors.* Molecules, 2022. **27**(8).

155. Feig, M., et al., *Performance comparison of generalized born and Poisson methods in the calculation of electrostatic solvation energies for protein structures.* J Comput Chem, 2004. **25**(2): p. 265-84.

156. Hawkins, G.D., C.J. Cramer, and D.G. Truhlar, *Pairwise solute descreening of solute charges from a dielectric medium.* Chemical Physics Letters, 1995. **246**(1): p. 122-129.

157. Hawkins, G.D., C.J. Cramer, and D.G. Truhlar, *Parametrized Models of Aqueous Free Energies of Solvation Based on Pairwise Descreening of Solute Atomic Charges from a Dielectric Medium.* The Journal of Physical Chemistry, 1996. **100**(51): p. 19824-19839.

158. Mongan, J., et al., *Generalized Born model with a simple, robust molecular volume correction.* J Chem Theory Comput, 2007. **3**(1): p. 156-169.

159. Onufriev, A., D. Bashford, and D.A. Case, *Exploring protein native states and large-scale conformational changes with a modified generalized born model.* Proteins, 2004. **55**(2): p. 383-94.

160. Genheden, S. and U. Ryde, *The MM/PBSA and MM/GBSA methods to estimate ligand-binding affinities.* Expert Opin Drug Discov, 2015. **10**(5): p. 449-61.

161. Kollman, P.A., et al., *Calculating structures and free energies of complex molecules: combining molecular mechanics and continuum models.* Acc Chem Res, 2000. **33**(12): p. 889-97.

162. Hou, T.J., et al., *Assessing the Performance of the Molecular Mechanics/Poisson Boltzmann Surface Area and Molecular Mechanics/Generalized Born Surface Area Methods. II. The Accuracy of Ranking Poses Generated From Docking.* Journal of Computational Chemistry, 2011. **32**(5): p. 866-877.

163. Heltweg, B., et al., *Subtype selective substrates for histone deacetylases.* J Med Chem, 2004. **47**(21): p. 5235-43.

164. Heltweg, B., J. Trapp, and M. Jung, *In vitro assays for the determination of histone deacetylase activity.* Methods, 2005. **36**(4): p. 332-7.

165. Dreger, A., et al., *Synthesis, biological evaluation, and molecular docking studies of deoxygenated C-glycosides as LpxC inhibitors.* Bioorg Chem, 2021. **117**: p. 105403.

166. Hoff, K., et al., *Synthesis and biological evaluation of triazolyl-substituted benzyloxyacetohydroxamic acids as LpxC inhibitors.* Bioorg Med Chem, 2020. **28**(13): p. 115529.

167. Dreger, A., et al., *Chiral Pool Synthesis, Biological Evaluation and Molecular Docking Studies of C-Furanosidic LpxC Inhibitors.* ChemMedChem, 2019. **14**(8): p. 871-886.

168. Watson, P.J., et al., *Insights into the activation mechanism of class I HDAC complexes by inositol phosphates.* Nature Communications, 2016. **7**.

169. Vannini, A., et al., *Substrate binding to histone deacetylases as shown by the crystal structure of the HDAC8-substrate complex.* Embo Reports, 2007. **8**(9): p. 879-884.

170. Shen, S. and A.P. Kozikowski, *Why Hydroxamates May Not Be the Best Histone Deacetylase Inhibitors--What Some May Have Forgotten or Would Rather Forget?* ChemMedChem, 2016. **11**(1): p. 15-21.

171. Bressi, J.C., et al., *Exploration of the HDAC2 foot pocket: Synthesis and SAR of substituted N-(2-aminophenyl)benzamides.* Bioorg Med Chem Lett, 2010. **20**(10): p. 3142-5.

172. Wagner, F.F., et al., *Kinetic and structural insights into the binding of histone deacetylase 1 and 2 (HDAC1, 2) inhibitors.* Bioorg Med Chem, 2016. **24**(18): p. 4008-4015.

173. Minami, J., et al., *Histone deacetylase 3 as a novel therapeutic target in multiple myeloma.* Leukemia, 2014. **28**(3): p. 680-9.

174. Jiang, Y.Q., et al., *Potent Hydrazide-Based HDAC Inhibitors with a Superior Pharmacokinetic Profile for Efficient Treatment of Acute Myeloid Leukemia In Vivo.* Journal of Medicinal Chemistry, 2021.

175. Xiao, Y., et al., *Discovery of histone deacetylase 3 (HDAC3)-specific PROTACs.* Chem Commun (Camb), 2020. **56**(68): p. 9866-9869.

176. Sun, P., et al., *Development of Alkylated Hydrazides as Highly Potent and Selective Class I Histone Deacetylase Inhibitors with T cell Modulatory Properties.* J Med Chem, 2022. **65**(24): p. 16313-16337.

177. Szermerski, M., et al., *Synthesis, biological evaluation and molecular docking studies of benzyloxyacetohydroxamic acids as LpxC inhibitors.* Bioorg Med Chem, 2014. **22**(3): p. 1016-28.

178. Wimmer, S., et al., *Synthesis, biological evaluation, and molecular docking studies of aldotetronic acid-based LpxC inhibitors.* Bioorg Chem, 2023. **131**: p. 106331.

179. Tangherlini, G., et al., *Synthesis and biological evaluation of enantiomerically pure glyceric acid derivatives as LpxC inhibitors.* Bioorg Med Chem, 2016. **24**(5): p. 1032-44.

7. APPENDIX

Table S 1. R2 values of all models generated for HDAC1, HDAC2 and HDAC3

Model Number	Method	Frame	R^2- HDAC1 n: 22	R^2- HDAC2 n: 23	R^2- HDAC3 n: 22
1	GB1	Emin1	0.06	0.15	0.68
2	GB1	Emin2	0.02	0.03	0.47
3	GB1	MD1-50	0.59	0.12	0.47
4	GB1	MD51-100	0.26	0.10	0.46
5	GB1	MD101-500	0.13	0.17	0.45
6	GB1	Emin3	0.11	0.22	0.46
7	GB2	Emin1	0.13	0.19	0.71
8	GB2	Emin2	0.05	0.06	0.50
9	GB2	MD1-50	0.14	0.33	0.48
10	GB2	MD51-100	0.26	0.22	0.49
11	GB2	MD101-500	0.24	0.14	0.49
12	GB2	Emin3	0.04	0.10	0.50
13	GB5	Emin1	0.18	0.19	0.66
14	GB5	Emin2	0.07	0.07	0.48
15	GB5	MD1-50	0.18	0.37	0.46
16	GB5	MD51-100	0.30	0.27	0.47
17	GB5	MD101-500	0.26	0.16	0.47
18	GB5	Emin3	0.05	0.13	0.48
19	GB8	Emin1	0.13	0.24	0.56
20	GB8	Emin2	0.11	0.06	0.46
21	GB8	MD1-50	0.23	0.66	0.40
22	GB8	MD51-100	0.10	0.43	0.44
23	GB8	MD101-500	0.21	0.32	0.45
24	GB8	Emin3	0.13	0.19	0.46
25	PB-bondi	Emin1	0.11	0.12	0.56
26	PB-bondi	Emin2	0.07	0.04	0.46
27	PB-bondi	MD1-50	0.03	0.47	0.52
28	PB-bondi	MD51-100	0.08	0.48	0.54
29	PB-bondi	MD101-500	0.28	0.52	0.63
30	PB-bondi	Emin3	0.22	0.41	0.56
31	PB-parse	Emin1	0.14	0.15	0.56
32	PB-parse	Emin2	0.11	0.05	0.46
33	PB-parse	MD1-50	0.19	0.18	0.57
34	PB-parse	MD51-100	0.29	0.23	0.61
35	PB-parse	MD101-500	0.08	0.19	0.54
36	PB-parse	Emin3	0.01	0.07	0.55

Table S 2. The docking scores, binding free energy results of the best model and in vitro data for HDAC1, MODEL3. The compounds were coloured based on the cut off values (1 μM IC$_{50}$). Green colour < 1 μM, red colour > 1 μM. Outlier is coloured in cyan.

HDAC1				
code	HDAC1 IC$_{50}$ (μM) or %inhibition	HDAC1-pIC$_{50}$	Docking_score	GB1_MD-1-50
67	0.07 ± 0.01	7.15	-13.05	-81.10
66	0.11 ± 0.01	6.96	-12.06	-81.83

code	IC50 or %inhibition	pIC50	Docking_score	GB8_MD-1-50
45	0.13 ± 0.01	6.89	-9.46	-71.75
48	0.14 ± 0.02	6.85	-9.45	-76.95
68	0.16 ± 0.03	6.80	-12.33	-86.33
69	0.18 ± 0.01	6.74	-12.17	-77.19
44	0.21 ± 0.07	6.68	-9.54	-70.59
49	0.26 ± 0.01	6.59	-12.72	-78.81
56	0.27 ± 0.03	6.57	-9.83	-76.66
54	0.29 ± 0.03	6.54	-8.90	-68.68
46	0.31 ± 0.03	6.51	-10.78	-77.26
57	0.33 ± 0.02	6.48	-10.13	-78.76
55	0.40 ± 0.06	6.40	-9.11	-68.49
47	0.45 ± 0.06	6.35	-8.85	-72.62
40	0.51 ± 0.05	6.29	-10.01	-72.55
43	0.52 ± 0.07	6.28	-9.67	-70.15
50	0.70 ± 0.08	6.15	-11.68	-79.44
51	0.76 ± 0.07	6.12	-11.18	-78.21
52	0.81 ± 0.07	6.09	-10.00	-72.69
53	3.0 ± 0.2	5.52	-10.06	-65.48
60	3.30 ± 0.18	5.48	-10.09	-62.14
62	4.3 ± 0.3	5.37	-9.45	-56.64
65	20.0 ± 1.0	4.7	-11.17	-6.25
41	25.8% @ 2 μM		-10.25	-66.93
42	33.9% @ 2 μM		-9.62	-68.88
58	5% @ 1 μM		-9.80	-64.84
59	27% @ 1 μM		-9.96	-65.31
61	0% @ 1 μM		-10.67	-62.49
63	0% @ 1 μM		-10.44	-65.72
64	0% @ 1 μM		-11.33	-56.90

Table S 3. The docking scores, binding free energy results of the best model and in vitro data for HDAC2, MODEL21. The compounds were coloured based on the cut off values (1 μM IC$_{50}$). Green colour < 1 μM, red colour > 1 μM. Outlier is coloured in cyan.

HDAC2				
code	HDAC2 IC$_{50}$ (μM) or %inhibition	HDAC2-pIC$_{50}$	Docking_score	GB8_MD-1-50
66	0.18 ± 0.06	6.74	-14.10	-119,64
67	0.26 ± 0.01	6.59	-14.88	-118,62
69	0.26 ± 0.07	6.59	-14.38	-122,05
45	0.28 ± 0.01	6.55	-11.30	-116,99
68	0.34 ± 0.01	6.47	-14.56	-122,36
56	0.50 ± 0.03	6.30	-11.17	-115,33

48	0.56 ± 0.04	6.25	-11.59	-117,82
54	0.56 ± 0.02	6.25	-10.94	-111,69
44	0.71 ± 0.04	6.15	-11.24	-115,59
52	0.74 ± 0.03	6.13	-11.37	-112,49
51	0.76 ± 0.04	6.12	-14.42	-123,37
50	0.77 ± 0.06	6.11	-13.72	-125,34
40	0.80 ± 0.07	6.10	-11.80	-116,37
47	0.93 ± 0.04	6.03	-11.00	-110,26
46	0.96 ± 0.05	6.02	-11.82	-119,63
57	1.37 ± 0.08	5.86	-11.71	-106,59
43	1.43 ± 0.08	5.84	-11.07	-107,25
55	1.48 ± 0.19	5.83	-10.82	-111,66
60	2.17 ± 0.18	5.66	-11.95	-106,74
49	2.47 ± 0.22	5.61	-14.09	-113,74
53	2.7 ± 0.2	5.57	-11.13	-108,69
62	4.2 ± 0.15	5.38	-12.10	-105,39
65	14.0 ± 2.0	4.85	-12.00	-86,74
41	30.3% @ 2 µM		-12.05	-108,81
42	20.1% @ 2 µM		-10.70	-107,18
58	7% @ 1 µM		-11.67	-105,91
59	15% @ 1 µM		-11.86	-109,68
61	0% @ 1 µM		-12.21	-102,84
63	0% @ 1 µM		-12.46	-109,62
64	0% @ 1 µM		-11.78	-107,88

Table S 4. The docking scores, binding free energy results of the best model and in vitro data for HDAC3, MODEL7. The compounds were coloured based on the cut off values (2 µM IC_{50}). Green colour < 2 µM, red colour > 2 µM. Outlier is coloured in cyan.

HDAC3				
code	HDAC3 IC_{50} (µM) or %inhibition	HDAC3-pIC_{50}	Docking_score	GB2_01_Emin1
45	0.31 ± 0.01	6.51	-10.89	-59.54
55	0.40 ± 0.02	6.40	-10.27	-61.74
60	0.40 ± 0.01	6.40	-11.00	-55.46
46	0.49 ± 0.06	6.31	-10.93	-64.91
56	0.50 ± 0.02	6.30	-9.63	-56.37
52	0.57 ± 0.02	6.24	-9.69	-59.32
48	0.59 ± 0.03	6.23	-10.91	-60.11
57	0.59 ± 0.04	6.23	-10.26	-61.13
54	0.81 ± 0.05	6.09	-9.13	-52.94
44	0.84 ± 0.03	6.08	-10.87	-60.91

43	1.06 ± 0.04	5.97	-10.63	-61.55
40	1.12 ± 0.07	5.95	-11.28	-63.69
62	1.6 ± 0.1	5.80	-10.52	-53.65
47	1.75 ± 0.06	5.76	-10.47	-59.57
53	1.9 ± 0.1	5.72	-10.93	-53.66
66	4.4 ± 0.1	5.36	-5.15	-21.00
67	6.1 ± 0.7	5.21	-5.69	-18.72
68	6.7 ± 0.5	5.17	-6.11	-19.75
61	8.7 ± 0.4	5.06	-11.53	-43.41
69	12.0 ± 1.0	4.92	-5.19	-18.48
65	14.0 ± 1.0	4.85	-9.99	-37.10
51	15 ± 1	4.82	-7.79	-27.02
41	65.2% @ 2 μM		-11.47	-66.39
42	26.8% @ 2 μM		-10.26	-60.36
58	13% @ 1 μM		-10.89	-55.46
59	30% @ 1 μM		-11.40	-55.28
49	0% @ 1 μM		-6.46	-15.32
50	0% @ 1 μM		-7.83	-29.06
63	0% @ 1 μM		-8.51	-44.71
64	0% @ 1 μM		-11.91	-43.26

Table S 5. The docking scores, binding free energy results, and prediction results of the test set for HDAC1.

HDAC1					
code	HDAC1 IC$_{50}$ (μM) or %inhibition	HDAC1-pIC$_{50}$	Predicted HDAC1 pIC$_{50}$	Docking_score	GB1_MD-1-50
70	0.32 ± 0.062	6.49	6.55	-12.11	-76.74
71	0.04 ± 0.006	7.39	6.31	-12.36	-73.71
72	0.019 ± 0.001	7.72	6.50	-12.53	-75.83
73	1.9 ± 0.1	5.72	5.70	-9.30	-60.78
74	4% @1 μM		5.58	-10.85	-58.50
75	0% @1 μM		5.77	-10.99	-62.06
76	6% @1 μM		5.68	-10.96	-60.33

Table S 6. The docking scores, binding free energy results, and prediction results of the test set for HDAC2.

HDAC2					
code	HDAC2	HDAC2-pIC$_{50}$	Predicted HDAC2 pIC$_{50}$	Docking_score	GB8_MD-1-50

126

	IC$_{50}$ (μM) or %inhibition				
70	0.61 ± 0.02	6.21	6.00	-14.01	-112.67
71	0.79 ± 0.02	6.10	6.24	-14.15	-118.28
72	1.1 ± 0.1	5.96	5.95	-13.95	-111.56
73	24 ± 2	4.62	5.89	-12.01	-110.06
74	10% @1 μM		5.52	-11.81	-101.63
75	13% @1 μM		5.29	-11.80	-96.34
76	14% @1 μM		5.52	-11.78	-101,56

Table S 7. The docking scores, binding free energy results, and prediction results of the test set for HDAC3.

HDAC3					
code	HDAC3 IC$_{50}$ (μM) or %inhibition	HDAC3-pIC$_{50}$	Predicted HDAC3 pIC$_{50}$	Docking_score	GB2_01_Emin1
70	8% @1 μM		5.06	-5.51	-23.42
71	6% @1 μM		5.01	-5.23	-21.48
72	4% @1 μM		4.98	-7.71	-20.77
73	15% @1 μM		5.98	-10.97	-54.11
74	21% @1 μM		5.81	-9.76	-48.42
75	19% @1 μM		5.80	-11.12	-48.17
76	25% @1 μM		5.79	-11.13	-47.74

CURRICULUM VITAE (CV)

Name:	Emre Fatih Bülbül
Birth place:	Kütahya/Turkey
Birth date:	07.08.1991
Linkedin:	https://www.linkedin.com/in/emre-fatih-bulbul-5b3498179/
ORCID ID:	0000-0002-9901-2022
Scopus ID:	57194777234
Language:	Turkish (native speaker)
	English (fluent)
	German (intermediate) (B2 level)

EDUCATION

- ✓ **PhD (2018-2022)** Department of Medicinal Chemistry, Martin Luther University Halle-Wittenberg Germany
  Research Thema: Structure - based design of inhibitors of the zinc-dependent enzymes histone deacetylase (HDAC) and UDP-3-O-(R-3-hydroxymyristoylyl)-N-acetylglucosamine deacetylase (LpxC)
- ✓ **Master (2015-2018)** Department of Pharmaceutical Chemistry, Eskisehir Anadolu University Turkey
  Research Thema: Synthesis of some thiazolyl sulfonamide derivatives and Investigation of their Anticancer effects.
- ✓ **Undergraduate (2009-2014)** Faculty of Pharmacy, Eskisehir Anadolu University Turkey
  Research Thema: (practical study in Department of Pharmaceutical Chemistry): Synthesis of some *N*-[4-(2-arylthiazol4-yl)phenyl]acetamide derivatives and investigation of their biological effects

JOB EXPERIENCES

1. **2022-2024** Postdoctoral Researcher, Department of Biochemistry, Maastricht University, Netherland
2. **2018-2022** Researcher - Institute of Pharmacy, Martin Luther University Halle-Wittenberg, Germany
3. **2015-2018** Research Assistant, Department of Pharmaceutical Chemistry, Istanbul Medipol University, Turkey
4. **2014-2014** (6 month) Internship, Public Pharmacy, Eskisehir, Turkey

PUBLICATIONS

2022

- S. Wimmer, K. Hoff, B. Martin, M. Grewer, L. Denni, R.L. Massanet, M.V. Raimondi, **E.F. Bülbül,** J. Melesina, S. Hotop, J. Haupenthal, H. Rohde, P. Heisig, A. Hirsch, M. Brönstup, W. Sippl, R. Holl, Synthesis, Biological evaluation, and molecular docking studies of aldotetronic acid-based-LpxC inhibitors. Bioorganic Chemistry, 2022, 106331. **doi: 10.1016/j.bioorg.2022.106331**

- P. Sun, J. Wang, K.S. Khan, W.L. Ng, N. Ilmenov, M. Zessin, **E.F. Bülbül**, D. Robaa, F. Erdmann, M. Schmidt, C. Romier, M. Schutkowski, A. Cheng, W. Sippl, Development of alkylated hydrazides as highly potent and selecive class I HDAC inhibitors with T cell modulatory properties, J. Med. Chem, 2022, 16313-16337, **doi: 10.1021/acs.jmedchem.2c01132**

- D. Kalbas, M. Meleshin, S. Liebscher, M. Zessin, J. Melesina, C. Schiene-Fischer, **E. F. Bülbül** F. Bordusa, W. Sippl, M. Schutkowski, Small changes make the difference for SIRT2: Two different binding modes for 3-arylmercaptoacylated lysine derivatives, Biochemistry, 2022, **doi: 10.1021/acs.biochem.2c00211**

- **E.F.Bülbül**, J. Melesina, H.S. Ibrahim, M. Abdelsalam, A. Vecchio, D. Robaa, M. Zessin, M. Schutkowski, W. Sippl, Docking, Binding free energy calculatons and In Vitro Characterization of Pyrazine Linked 2-Aminobenzamides as Novel Class I Histone Deacetylase (HDAC) inhibitors, Molecules, 2022, 27 (8), 2526, **doi: 10.3390/molecules27082526**

- H. Ibrahim, M. Abdelsalam, Y. Zeyn, M. Zessin, , A. M. Mustafa, M. A. Fischer, P. Zeyen, , P. Sun, **E F. Bülbül,** A. Vecchio, F. Erdmann, M. Schmidt, D. Robaa, C. Barinka, C. Romier, M. Schutkowski, O. H. Krämer, and W. Sippl, Synthesis, molecular docking and biological characterization of pyrazine linked 2-aminobenzamides as new class I selective histone deacetylase (HDAC) inhibitors with anti-leukemic activity, Int. J. Mol. Sciences, 2022, 23, 369, **doi:10.3390/ijms23010369.**

2021

- A. Dreger, K. Hoff, O. Agogliatta**, E. F. Bülbül**, J. Melesina, W. SIppl, R. Holl, Synthesis, biological evaluation and molecular docking studies of deoxygenated C-glycosides as LpxC inhibitors, Bioorg. Chem. 2021, **https://doi.org/10.1016/j.bioorg.2021.105403**.

- L. Yurttas, H. E. Temel, M. O. Aksoy, **E. F. Bülbül**, G. A. Ciftci; New chromanone derivatives containing thiazoles: Synthesis and antitumor activity evaluation on A549 lung cancer cell line, 2021 Sep 17, **https://doi.org/10.1002/ddr.21879**

- J. Melesina, C. V. Simoben, L. Praetorius, **E. F. Bülbül**, D. Robaa, W. Sippl. *Strategies to Design Selective HDAC Inhibitors*. ChemMedChem. 2021 Jan 11. **doi:10.1002/cmdc.202000934** .

2020

✓ Z. Sahin, S.Biltekin, **E. F. Bülbül** , L. Yurttas, B. Berk, S. Demirayak, Design and synthesis of new donepezil analogs derived from arylpiperazine scaffold as acetylcholinesterase inhibitors, Phosphorus, Sulfur, and Silicon and the Related Elements, 2020 Sep 27. **doi: 10.1080/10426507.2020.1830773**

✓ K. Hoff, S. Mielniczuk, O. Agoglitta, M. T. Iorio, M. Caldara, **E. F. Bülbül**, J. Melesina, W. Sippl, R. Holl. *Synthesis and biological evaluation of triazolyl-substituted benzyloxyacetohydroxamic acids as LpxC inhibitors*. Bioorg Med Chem. 2020 Apr 25:115529. **doi:10.1016/j.bmc.2020.115529** .

2019

✓ Dreger, O. K. O. Agoglitta, **E. F. Bülbül**, J. Melesina, W. Sippl,and R. Holl. Chiral pool synthesis, biological evaluation and molecular docking studies of C-furanosidic LpxC inhibitors. ChemMedChem. 14, 871-886, 2019. **doi:10.1002/cmdc.201900068** .

✓ S. Demirayak, Z. Sahin, M. Ertas, **E. F. Bülbül**, C. Bender, S. N. Biltekin, B. Berk, B. N. Saglik, S. Levent, L. Yurttas, Novel Thiazole-piperazine derivatives as potential cholinesterase inhibitors, Journal of Heterocyclic Chemistry, 2019, 56, 12, 3370-3386**. doi:10.1002/jhet.3734**

✓ M. Ertas, Z. Sahin, **E. F. Bülbül**. C. Bender, S. N. Biltekin, B. Berk, L. Yurttas, A. M. Nalbur, H. Celik, S. Demirayak, Arch. Pharm, 2019, 352, (11), e1900033 **doi: 10.1002/ardp.201900033**

2018

✓ Z. Sahin, M. Ertas, C. Bender, **E. F. Bülbül**, B. Berk, S. N. Biltekin, L. Yurttas, S. Demirayak, Thiazole-substituted benzoylpiperazine derivatives as acetylcholinesterase inhibitors, Drug Dev Res, 2018, 79 (8), 406-425**, doi: 10.1002/ddr.21481.**

2017

✓ L. Yurttas, **E. F. Bülbül**, S. Tekinkoca, S. Demirayak, Antimicrobial Activity Evaluation of New 1,3,4-oxadiazole Derivatives, Acta Pharmaceutica Sciencia, 2017, 55, 2**, doi: 10.23893/1307-2080.APS.05511**

✓ Berk, Y. A. Tahirovic, **E. F. Bülbül**, S. N. Biltekin, The synthesis, antimicrobial activity studies, and molecular property predictions of novel benzothiazole-2-thione derivatives, Acta Pharm. Sci, 2017, 55 (3), **doi: 10.23893/1307-2080.APS.05516**

DECLARATION OF AUTHORSHIP

With this document I state that the content of the dissertation is my sole work, that i wrote and formulated the thesis on my own without external help, and that all textual references used to write the thesis and which originate from other sources, have received due credit and citation.

Heerlen/Netherland, 21.06.2023

…………………….
Emre Fatih Bülbül